공학박사 학위논문

Synthesis, Property, and Optoelectronic Device Application of Bis-Lactam-Based Organic Semiconducting Materials

비스락탐을 기반으로 한 유기반도체 물질의 합성, 특성 및 광전자 소자 응용에 대한 연구

2017년 8월

서울대학교 대학원

재료공학부

윤 원 식

Synthesis, Property, and Optoelectronic Device Application of Bis-Lactam-Based Organic Semiconducting Materials

A THESIS SUBMITTED IN PARTIAL FULFILLMENT OF
THE REQUIREMENTS FOR THE DEGREE OF
DOCTOR OF PHILOSOPHY
IN ENGINEERING AT THE GRADUATE SCHOOL OF
SEOUL NATIONAL UNIVERSITY

AUGUST 2017

By
Won Sik Yoon

Supervisor
Prof. Soo Young Park

Abstract

Synthesis, Property, and Optoelectronic Device Application of Bis-Lactam-Based Organic Semiconducting Materials

Won Sik Yoon

Department of Materials Science and Engineering

The Graduate School

Seoul National University

Organic semiconductors have attracted great attention in the last decade because of their promising potential as materials for advanced optoelectronic devices. Among organic semiconductors, those based on bis-lactam materials, such as diketopyrrolopyrrole (DPP), isoindigo (II), isoDPP, and thienoisoindigo (TII), have been extensively studied as desirable electron-withdrawing building blocks, because of their unique features, which include (a) a high electron affinity because of the electron-withdrawing effect of the lactam units; (b) a high degree of π-π stacking, deriving from their quasi-planar backbone structure; and (c) the possibility of controlling their solubility by incorporation of suitable alkyl and aryl side chains at the lactam *N*-atom position. Hence, I studied the bis-lactam-based semiconducting materials as electron-deficient building blocks for high-performance organic field-effect transistors (OFETs)

and organic photovoltaics (OPVs). In this thesis, I have designed and synthesized three different kinds of novel bis-lactam-based semiconducting materials by modifying their structures, and then investigated their structure-property relationships.

First, a new high-performance small molecular n-channel semiconductor based on diketopyrrolopyrrole (DPP), DPP-T-DCV was designed and synthesized. The frontier molecular orbitals have been engineered by introducing a strong electron-accepting dicyanovinyl group. The well-defined lamellar structure of the DPP-T-DCV crystal displayed a uniform terrace step height corresponding to a molecular monolayer in the solid-state. As a result of the high level of crystallinity derived from the conformational planarity, OFETs made of dense-packed solution-processed single-crystals of DPP-T-DCV exhibited an electron mobility up to 0.96 $cm^2\ V^{-1}\ s^{-1}$, one of the highest values yet obtained for DPP derivative-based n-channel OFETs. Polycrystalline OFETs also showed decent electron mobility of 0.64 $cm^2\ V^{-1}\ s^{-1}$ suitable for practical device applications. (Chapter 2)

Second, a novel electron-accepting bis-lactam building block, 3,7-dithiophen-2-yl-1,5-dialkyl-1,5-naphthyridine-2,6-dione (NTDT), and a conjugated polymer P(NTDT-BDT) comprising NTDT as an electron acceptor and benzo[1,2-*b*:4,5-*b*']dithiophene (BDT) as an electron donor have been designed and synthesized for producing efficient OPVs. The thermal, electronic, photophysical, electrochemical, and structural

properties of NTDT and P(NTDT-BDT) have been studied in detail and compared with those of the widely used bis-lactam acceptor dithienyl-substituted-DPP (DPPT) and its polymer P(DPPT-BDT). Compared to DPPT derivatives, NTDT and P(NTDT-BDT) exhibited remarkably higher absorption coefficients, deeper highest occupied molecular orbital energy levels, and more planar structures. A bulk heterojunction solar cell based on P(NTDT-BDT) exhibited a power conversion efficiency of up to 8.16% with a short circuit current (J_{sc}) of 18.51 mA cm^{-2}, one of the highest J_{sc} values ever obtained for BDT-based polymers. It was successfully demonstrated that the novel bis-lactam unit NTDT is a promising building block for use in OPVs. (Chapter 3)

Although the performance of the first successful NTDT-based OPVs, P(NTDT-BDT), was promising, it operated best only for medium-thick active-layer (≈ 140 nm) due to insufficient polymer crystallinity. Therefore, it was considered that the polymer crystallinity should be increased via backbone structure modification in order to produce more efficient (> 9% PCE) thick-active-layer (> 200 nm) OPVs. To this end, new semiconducting polymers, PNTDT-2T, PNTDT-TT, and PNTDT-2F2T, with NTDT as an acceptor, as well as 2,2'-bithiophene (2T), thieno[3,2-*b*]thiophene (TT) and 3,3'-difluoro-2,2'-bithiophene (2F2T) as donors were designed and synthesized. It was found that PNTDT-2F2T exhibited superior polymer crystallinity and a much higher absorption coefficient than those of PNTDT-2T or PNTDT-TT attributed to the appropriate matching between the highly coplanar acceptor (NTDT) and donor (2F2T)

building blocks. A bulk heterojunction solar cell with a thick active layer (>200 nm) of PNTDT-2F2T simply fabricated without using post-fabrication hot processing, demonstrated an outstanding power conversion efficiency of up to 9.63%, with a short circuit current of 18.80 mA cm^{-2} and a fill factor of 0.70. (Chapter 4)

Keyword : organic semiconductor, organic field-effect transistors (OFETs), organic solar cells (OPVs)

Student Number : 2009-20624

Contents

List of Tables

Chapter 2

Chapter 3

Chapter 4

List of Schemes

Chapter 2

Chapter 3

Chapter 4

List of Figures

Chapter 1

Chapter 2

Chapter 3

Chapter 4

Chapter 1. Introduction

1.1. Organic electronics

Organic materials are made up of carbon and hydrogen, but they can also contain heteroatoms such as nitrogen, sulfur, oxygen, and halogens. In nature, countless combinations of these elements are found in living organisms and ecosystems, and over the course of time humans have synthetized a vast number of new organic materials, such as dyes, pharmaceuticals, and plastics for healthcare, and scientific development. In 1977, Shirakawa, MacDiarmid, and Heeger observed metallic conductivity in electrochemical iodine-doped polyacetylene,[1,2] and were awarded later with the 2000 Nobel Prize in Chemistry for "The discovery and development of conductive polymers". Since that breakthrough, much effort has been devoted to the development of organic semiconducting materials. In comparison to inorganic semiconductors, organic materials could lead to the production of cheap, printable and lightweight electronic devices, and these perspectives triggered extensive researches in universities and even more in industry, with special attention to the field of optoelectronic devices.

In recent years, many organic semiconducting materials have been widely used for advanced components such as organic light emitting diodes (OLEDs),[3,4] organic thin

film transistors (OFETs),[5-8] organic photovoltaics (OPVs),[9-11] organic memories,[12] organic sensors,[13] organic batteries,[14] and printed radio-frequency identification (RFID).[15,16] Through the extensive computational and experimental research, it has been proven that the fabrication of organic semiconductors is easier and cheaper than that of silicon-based ones. In addition, there are a huge number of organic materials whose properties can be easily tuned by modifying their chemical structure, making them suitable for specific devices. However, there is still a need for materials with better performance, i.e. higher charge mobility for OFETs and better power conversion efficiency (PCE) for practical OPVs applications. Therefore, it is necessary to develop new semiconducting materials with specifically engineered frontier molecular orbitals (MOs), and to establish design strategies for commercial applications of organic optoelectronic devices.

1.1.1. Charge carrier transport

Most optoelectronic devices, such as OLEDs, OFETs and OPVs require, in order to operate efficiently, a controlled transport of charge carrier and a high charge mobility. Thus, control of charge carrier transport in organic semiconductors is very important for practical applications. Therefore, much effort is being devoted not only to the development of high-performance materials but also to understand the parameters

which control the charge transport.[17-19] In earlier research works, the charge transport in π-conjugated small molecules has received much more attention than polymeric materials, because high-quality single crystals with very few impurities could be grown using various slow crystal growth methods.[20] The benchmark charge carrier mobility of 20~40 cm^2 V^{-1} s^{-1} in OFETs was achieved in rubrene single crystals grown by physical vapor transport.[21-23] However, most of them have limited solubility and poor mechanical properties, and cannot be easily integrated in industrial processes. Therefore, charge transport in π-conjugated polymers has been significantly investigated, and some results show that the charge mobility of semi-crystalline polymers can be as good as that of small molecules.[24,25] For example, Tseng et al. reported highly crystalline polymer, poly[4-(4,4-dihexadecyl-4H-cyclopenta[1,2-b:5,4-b']dithiophen-2-yl)-*alt*-[1,2,5]thiadiazolo[3,4-c]pyridine] (PCDTPT), containing thiadiazolopyridine acceptor and cyclopentadithiophene donor. The PCDTPT OFETs exhibited a high hole mobility of 23.7 cm^2 V^{-1} s^{-1}.[26] In recent years, a large number of theoretical and experimental studies have been devoted to investigating the factors influencing charge transport in small molecules and polymeric materials, such as molecular packing, disorder, presence of impurities and size/molecular weight.[27]

Molecular packing is a most important factor affecting the charge transport properties of small molecules. The interaction between neighboring molecules can vary considerably for different molecular packing, leading to different solid-state electronic structure and charge carrier mobility. A number of previous studies have shown that the

solid state packing is determined by various noncovalent secondary bonding interactions (e.g. electrostatic interaction, hydrogen bonding, π-π stacking, and van der Waals interaction) between adjacent molecules. Thus, by controlling the intermolecular interactions, the stacking structure of single crystals can be effectively tuned. There are four main packing motifs in crystals (herringbone packing without π-π overlap, herringbone packing with π-π overlap, lamellar motif with 1-D π-stacking, lamellar motif with 2-D π-stacking) as shown in **Figure 1-1**.[28,29] According to the theoretical investigations, cofacial lamella packing is the most efficient packing mode for attaining high carrier mobility compared with herringbone packing, since it can maximize the transfer integral between the neighboring molecules. For example, TIPS-pentacene has a 2D π-stacking packing, and thus has a higher value of the transfer integral than that of the herringbone packed pentacene. Nevertheless, in the actual OFET devices the charge carrier mobility of pentacene is much higher than that of TIPS-pentacene.[30] This experimental result was originated from long-range 2D ordered morphology of pentacene, which offeres efficient charge carrier injection and intrinsic defect-free charge transport. Hence, the theoretical value of the transfer integral does not necessarily correspond to the experimental charge carrier mobility of organic semiconducting materials. Apart from the packing mode, a dense molecular packing and an effective π-orbital overlapping are believed to be crucial for high performance organic semiconductors.

In polymeric materials, chain alignment and degree of crystallinity can significantly

influence the charge transport properties as well. In contrast to small molecules, conjugated polymeric materials have many degrees of conformational freedom, therefore resulting in microstructures that vary from completely amorphous to crystalline. In crystalline polymers, the number of hole trapping sites is effectively reduced, thereby improving the charge transport and its stability.[31] In addition, the crystal orientation also plays a crucial role in charge transport. Although most crystalline polymers show anisotropic charge transport properties, the charge transport occurs most efficiently in the direction of π-stacking. Thus, optimal device performances are often achieved when the π-stacking direction in the film is aligned with the direction of the intended charge transport. The charge transport in the active layer of an OFET device is parallel to the substrate surface between the source and drain electrodes, whereas in an OPV device, charge carriers (holes and electrons) traverse the active layer perpendicularly to the substrate towards their respective electrode (anode and cathode).[32,33] Therefore, different material designs should be considered to optimize the charge carrier transport property in OFET and OPV devices.

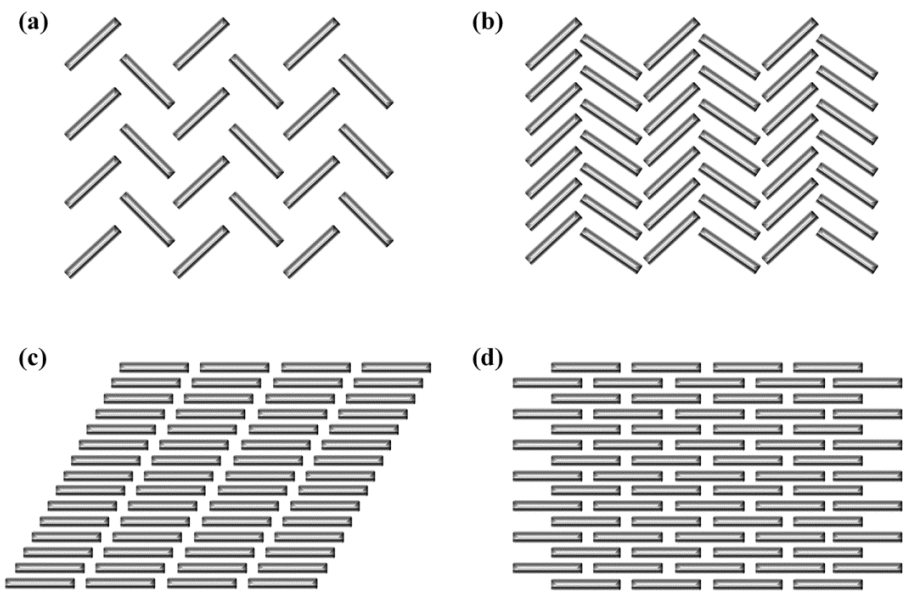

Figure 1-1. Four kinds of molecular packing motifs. (a) Herringbone packing, (b) slipped herringbone packing, (c) lamella motif, 1D π-stacking, and (d) lamella motif, 2D π-stacking.

1.1.2. Bandgap and energy level engineering

The engineering of the bandgap (E_g) and the molecular energy level of organic semiconducting materials is of great importance in improving the device properties. The E_g of organic semiconducting materials is given by the energy difference between the highest occupied molecular orbital (HOMO) and the lowest unoccupied molecular orbital (LUMO), and its size dictates the light absorption, charge separation and charge transport properties of the material. Based on the theory proposed by Roncali,[34,35] the E_g of organic semiconductors is determined by several factors *i.e.* the energy related to bond length alternation, the mean deviation from planarity, the inductive or mesomeric electronic effects of eventual substitutions, and the intermolecular or interchain coupling in the solid state (**Figure 1-2**).

Bond length alternation is defined as the average of the difference in the length between adjacent carbon-carbon bonds in long conjugated molecular chains. Most conjugated organic semiconducting materials have single and double bonds in their molecular structure and, as the single bonds are longer than the double bonds, they exhibit bond length alternation, which contributes to the E_g.[36-38] According to the results of Bredas,[39] the E_g decreases as a function of increasing quinoid character of the conjugated backbone. For example, polyaromatic polymers such as poly(*p*-phenylene), polythiophene, and polypyrrole have two resonance structures (benzenoid

and quinoid, **Figure 1-3**) that are interchangeable through the single and double bonds. According to the calculation, as the quinoid character increases, the HOMO energy level shifts up and LUMO energy level shifts down, resulting in an E_g which is smaller for the quinoid structure than the benzenoid structure.

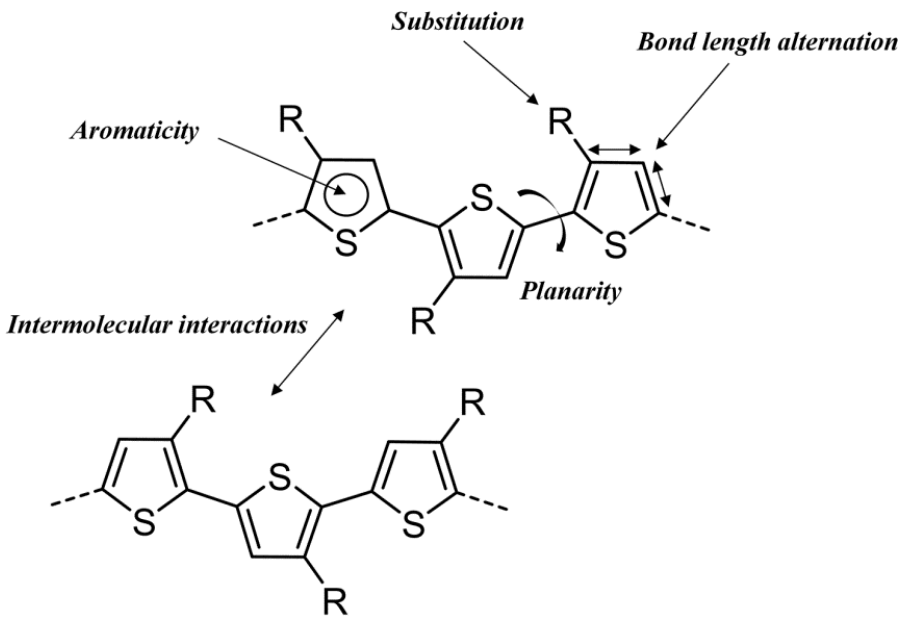

Figure 1-2. The factors determining the bandgap of organic materials.

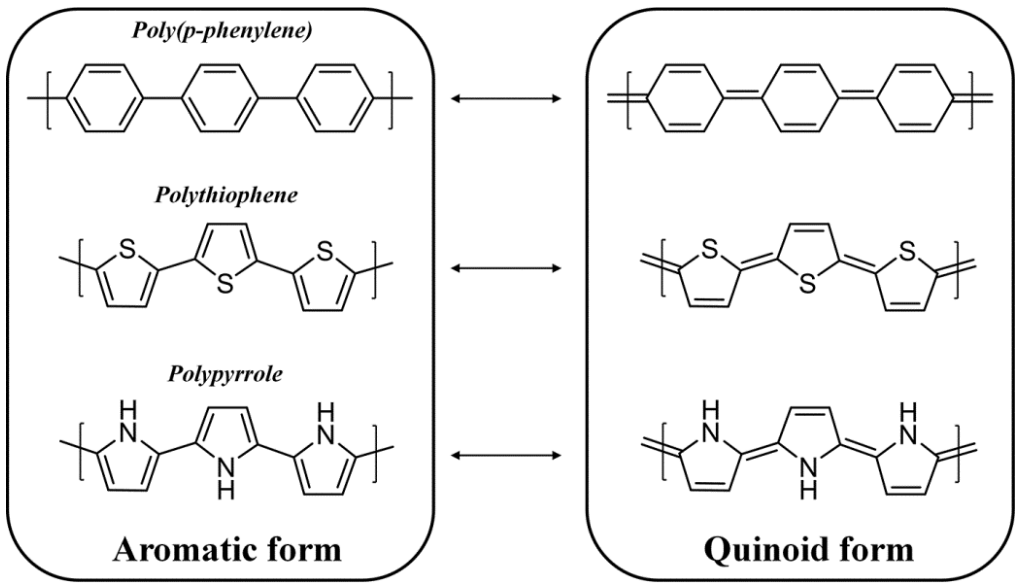

Figure 1-3. Aromatic and quinoid forms of poly(*p*-phenylene), polythiophene, and polypyrrole.

Molecular planarity is another key parameter that affects the charge carrier transport and the E_g of organic semiconductors. If the torsion angle between the molecular planes is too high, it can disrupt the conjugation along a conjugated backbone and result in an increase of E_g due to the reduction of the effective conjugation length.[40] Molecular design strategies aimed at planarization such as improving regioregularity, extended fused system, and intramolecular non-bonding interactions effectively narrow the E_g in semiconducting materials. As a typical example, regioregular poly(3-hexylthiophenes) (P3HT), constructed using the same isomer of the monomer, has a

smaller E_g than head-to-head coupled P3HT.[41] As another example, fluorene with a fused aromatic structure, obtained by bridging two benzene rings, exhibits an E_g smaller than non-planar biphenyl molecules.[42]

In addition, the molecular orbitals are significantly affected by the insertion of electron-withdrawing or electron-donating groups along the conjugated backbones, owing to the mesomeric or inductive effect. Therefore, the HOMO and LUMO energy levels are effectively controlled by introducing appropriate substituents.[43,44] There are many examples in the literature, as will be discussed in detail in the next chapter. The factors listed above (bond length alternation, planarity, and substitution) are only relevant to molecular orbitals of single-chain conjugated molecules. However, the width of E_g is also determined by the overlap of molecular orbitals due to the interactions between individual conjugated molecules. The intermolecular interactions between the molecules can further influence the E_g in the solid state. For example, well-ordered conjugated polymers exhibit a much narrower E_g than disordered or amorphous polymers.[45]

1.1.3. Light absorption of conjugated molecules

The process of light absorption in conjugated molecules is due to electrons that absorb the photon energy and are excited from the HOMO to LUMO level. This light absorption is a critical process affecting the performances of OPVs, as the concept of an OPV is to absorb photons from the sunlight and convert them into an electrical current. Most of the research on OPVs is focused on fitting the absorbance of the conjugated materials to the solar spectrum, by tuning the energy levels and energy band gap of conjugated materials, as described in the previous section.

Another important factor is increasing the magnitude of the optical absorption in conjugated molecules, therefore allowing for higher photocurrent generation in OPVs. However, there is a limited understanding of the magnitude enhancement of the optical absorption, and it is seldom identified as a design target. The absorption coefficient is a measure of how strongly a substance absorbs light: the larger its value, the greater the absorption. In addition, the absorption coefficient is closely related to the probability that an electron is excited. Therefore, the probability of light absorption is related to the oscillator strength (*f*). If we consider the conjugated molecule as a classical oscillating dipole, the oscillator strength (*f*) is defined as:

$$f = 4.319 \times 10^{-9} \int_{band} d\,\nu\varepsilon(\nu)$$

where ε is the extinction coefficient and ν is the wave number. The oscillator strength is

also related to the transition dipole moment by:

$$f = \left(\frac{8\pi m_e \nu}{3e^2 h}\right)\mu^2$$

That is, the transition rate due to light absorption is proportional to the square of the transition dipole moment and can be strongly enhanced by increasing the dipole moment.[46] Transition dipole moments are controlled by several factors. Increasing the size of the molecule, generally results in an increase of its dipole moment and transition probability. For example, when conjugated systems increase in size from benzene to anthracene, the absorption peak shifts toward longer wavelengths and the molar absorption coefficient effectively increases (**Figure 1-4**).[47] A theoretical analysis of the molecular orbital geometries allows the calculation of the light absorptivity, based on the magnitude of orbital overlap between the ground state and the excited state. This orbital overlap often used as a theoretical quantity proportional to the intensity of light absorbance. Vezie et al. reported that rigid molecular structures, compared to curved structures, promote the delocalization of HOMO/LUMO wave functions, and should therefore favor the HOMO/LUMO overlap and lead to a large absorption coefficient for the lowest optical transition (**Figure 1-5**).[48]

(a)

(b)

Substance	Absorption Peak	Molar Absorption Coefficient
Benzene	255 nm	180
Naphthalene	286 nm	360
Anthracene	375 nm	7100

(c)

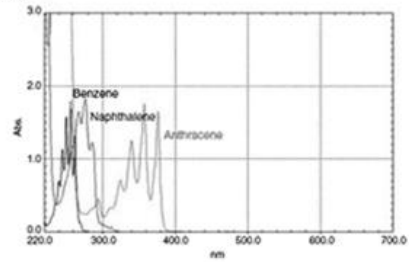

Figure 1-4. (a) Molecular structures, (b) molar absorption coefficients, and (c) absorption spectra of Benzene, Naphthalene, and Anthracene.[47]

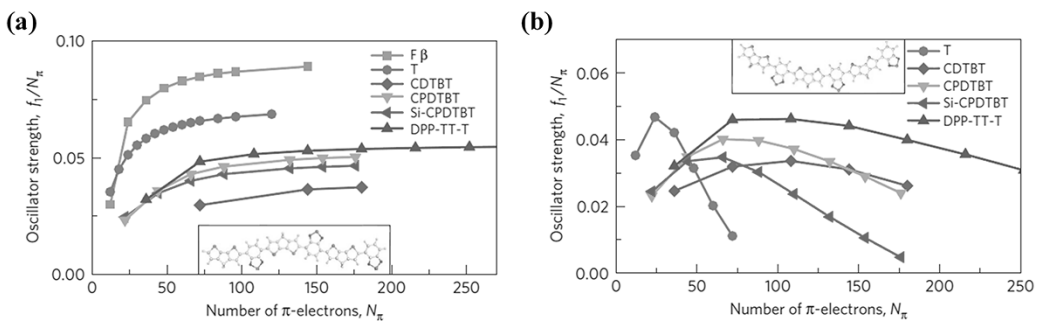

Figure 1-5. Calculated oscillator strength, normalized using the number of π-electrons, and corresponding spectra for oligomers of the corresponding polymers calculated for (a) the alternating (*trans*) configuration and (b) the *cis* configuration.[48]

1.2. Organic field-effect transistors

Field-effect transistors (FETs) are one of the most important inventions in twentieth century, can be found in automation and commutication technologies, and in all kinds of computing systems.[49] Crystalline silicon and other inorganic materials are used for the fabrication of FETs, but these rigid and expensive materials are not suitable for some specific electronic applications. A transition from FETs to OFETs offers a number of benefits such as large-scale solution processing, roll-to-roll printing, and a new generation of flexible electronic devices.[50-52] Organic semiconductors have been the subject of extended research during the last decade, but many major challenges are still confronting the field of organic electronics. For example, the field of n-channel organic semiconductors has made little progress, due to low charge carrier transport efficiencies caused by inherent instabilities and inappropriate frontier molecular orbitals.[53] It is therefore necessary to develop new n-channel semiconducting materials with molecular orbitals rationally engineered toward practical applications (e.g. CMOS, p-n junctions).

1.2.1. Working principle

Most OFETs are built according to four different construction principles: top-contact

bottom-gate (TCBG), bottom-contact bottom-gate (BCBG), top-contact top-gate (TCTG), and bottom-contact top-gate (BCTG) (**Figure 1-6**). OFETs are usually a composed of electrodes, an insulator and a semiconducting layer. The electrodes are contact with the semiconducting layer, while the gate electrode is insulated. In general, BGTC and TGBC devices showed better results than other devices, probably because of the improved interface between the semiconductor layer and the electrodes.[54]

When there is no gate voltage applied ($V_G = 0$), a negligible current flows between source and drain electrodes, and the FET is in the so-called "off" state. If a voltage V_G is applied to the gate, an internal electric field builds up in the gate insulator capacitor, and for a gate voltage exceeding a given threshold (V_T) this results in the accumulation of charge at the insulator-semiconductor interface; if a drain-source voltage V_D is applied to the device, this charge then produces a current between the drain and source, and the device is in the "on" state. When the gate voltage is applied ($V_G \neq 0$), if $V_G < 0$ and holes accumulate in the active layer, it is called a p-type transistor, and if $V_G > 0$ and electrons accumulate at the interface between the organic active layer and the dielectric, it is called an n-type transistor.[55]

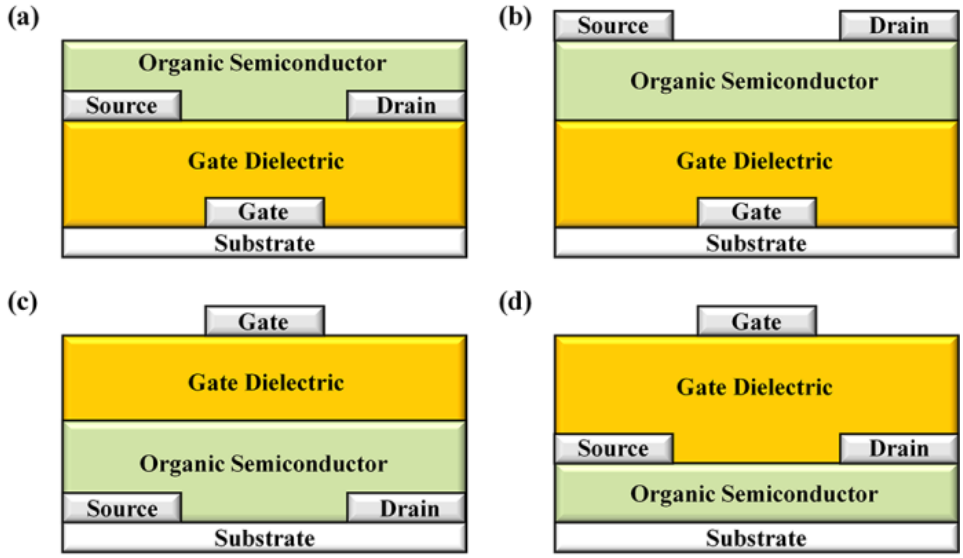

Figure 1-6. Four common geometries of OFETs: (a) bottom-gate bottom-contact (BGBC), (b) bottom-gate top-contact (BGTC), (c) top-gate bottom-contact (TGBC), and (d) top-gate top-contact (TGTC).

1.2.2. Device characterization

In order to characterize the electrical behavior of OFETs, the "output characteristics" and "transfer characteristics" are measured. **Figure 1-7** shows representative curves of output and transfer characteristics of pentacene in OFET devices. In the output characteristics, a current (I_{DS}) is generated in the drain-source circuit, responding to the applied V_{DS} under constant V_G. In the linear regime (source-drain voltage (V_{DS}) << gate voltage (V_G) – threshold voltage (V_T)), I_{DS} increases linearly by increasing V_{DS} and can

be determined using the following equation:

$$I_{DS,lin.} = \frac{W}{L}\mu_{lin.}C_i(V_G - V_T)V_{DS}$$

where C_i is the capacitance per unit area of the insulating layer, W is the channel width, L is the channel length, and μ is the field effect charge mobility.

Instead, in the saturation regime, I_{DS} can be derived as:

$$I_{DS,sat.} = \frac{W}{2L}\mu_{sat.}C_i(V_G - V_T)^2$$

Therefore, we can obtain the linear mobility by plotting $I_{DS,lin}$ against V_G and the saturation mobility by plotting $I_{DS,sat}$ against V_G. Calculated values for the mobility in the linear and saturation regimes can be different. Underestimation of mobility usually occurs in the linear regime model due to contact effects, while overestimation is observed in the saturation regime, attributed to fringe leakage currents outside the channel. In general, the saturation model is widely accepted; therefore, the field effect charge mobility can be derived as:

$$\mu_{sat.}(V_G) = \frac{\partial I_{DS,sat}}{\partial V_G} \cdot \frac{L}{WC_i} \cdot \frac{1}{V_G - V_T}$$

When the current signal (I_{DS}) is generated in the drain-source circuit, responding to the applied V_G under constant V_{DS} in transfer characteristics. From the transfer characteristics, the on/off ratio (I_{on}/I_{off}), threshold voltage and subthreshold swing can be easily obtained.[56]

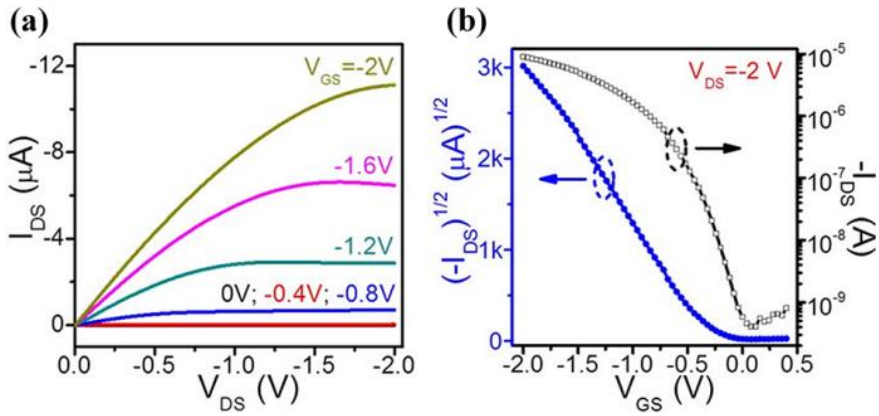

Figure 1-7. (a) Output and (b) transfer curves of pentacene in OFETs.[55]

1.2.3. Energy level of OFET materials

As mentioned above, during OFET operation the charge carriers will accumulate at the gate-insulator interface. These carriers are then extracted from the metal electrodes, and this extraction process is influenced by the injection barriers originating from the bias between the energy levels of frontier molecular orbitals of the organic semiconductors and the Fermi level of metal electrodes. Thus, the Fermi level of the metal and the energy levels of the organic semiconducting materials have to match.

For p-type transistors, electrons are injected into the metal electrodes from the HOMO energy level of semiconductors. An empirical HOMO energy level of stable p-type semiconductors should be lower than -4.9 eV. In addition, an even lower limit of -5.5 eV has been proposed, in order to obtain an Ohmic contact with metal electrodes.

Fortunately, it is possible to tune the HOMO energy level of organic semiconductors by molecular engineering. However, for n-type transistors, the LUMO energy level typically ranges from -4.0 eV to -3.0 eV, thus forming a large injection barrier for transistors. Furthermore, the electron carriers tend to easily degrade by oxidation because of the relatively high LUMO energy. Thus, a high electron affinity (LUMO below –4.0 eV) should be obtained by introducing strongly electron-deficient functionalities that improve the electron injection from the contact electrodes to the π-conjugated backbones.[57]

1.3. Organic photovoltaics

The first silicon-based solar cell was developed in 1954, at Bell Laboratories. Given the increasing global energy demand, silicon-based solar cell technology dominates the commercial market and has reached an efficiency of 26% with single-crystal silicon.[58] However, the drawbacks of silicon-based solar cells, such as high price and weight, limit the widespread application of these high-performing devices. Even though the silicates used for silicon production are abundant and inexpensive, the relevant costs for producing the high-purity final material, and the low optical density of silicon, which requires relatively thick silicon layers, make silicon-based solar cells relatively expensive.[59,60] Therefore, new technologies and innovations that reduce material usage and manufacturing costs must be investigated. One of these technologies currently being researched is organic-based solar cells.[61]

Compared to silicon-based solar cells, organic-based solar cells or OPVs have several advantages: they are lightweight, inexpensive to fabricate, structurally flexible, customizable at the molecular level, easy to dispose of and potentially have a less adverse environmental impact. Another main advantage of OPVs is potential transparency, and thus can be applied in windows, walls, flexible electronics, etc. On the other hand, even the best laboratory OPV devices have a power conversion efficiency (PCE) of 12%, lower than inorganic solar cells, and OPVs also suffer from

stability problems. Thus, efforts have been devoted to the design and synthesis of new organic materials and to the optimization of device fabrication with the aim to improve their efficiency and stability.[62,63]

1.3.1. Device architecture

Conventional OPV device architecture is shown in **Figure 1-8**a.[64] An OPV device is generally constructed using different stacked material layers, each having a specific function. The substrate is usually made of indium tin oxide (ITO) glass, which is a transparent anode material with a high work function, whose purpose is the collection of holes.[65-68] On top of the substrate, a hole conducting layer of poly(3,4-ehtylenedioxythiophene) polystyrene sulfonate (PEDOT:PSS) is deposited by spin coating. PEDOT:PSS forms an Ohmic contact by decreasing the work function of ITO from -4.4~4.8 eV to -5.0 eV, and also smooths the ITO surface.[69,70] The active layer is composed of an electron-donor material and an electron-acceptor material. The electron acceptor material is generally made of a fullerene-based acceptor, e.g., [6.6]-phenyl-C61-butyric acid methyl ester (PCBM), a soluble fullerene derivative with good electron transport properties. Because of some drawbacks of PCBM, such as weak absorption of visible light, non-fullerene electron acceptors are being considered as potential alternatives to PCBM.[71,72] On top of the active layer, an electron transport

layer (interlayer material) such as calcium or lithium fluoride is deposited by means of vacuum-deposition, and is followed by the deposition of a low work function electrode (Al).[73] However, the short-term stability of the low work function cathodes used in conventional architectures is often of significant detriment to the device's operation. With the introduction of inverted device architectures, the stability problems can be greatly reduced by reversing the polarities of the electrodes (**Figure 1-8**b). For conventional geometry, the transparent electrode is the anode, meaning that the current flows away from the front electrode. In the inverted device, this process is reversed, the front transparent electrode acts as the cathode and the current flows towards it. In most cases, devices with inverted architecture exhibited long-term stability and improved overall performances, and are now frequently employed in high-performance OPV devices.[74-76]

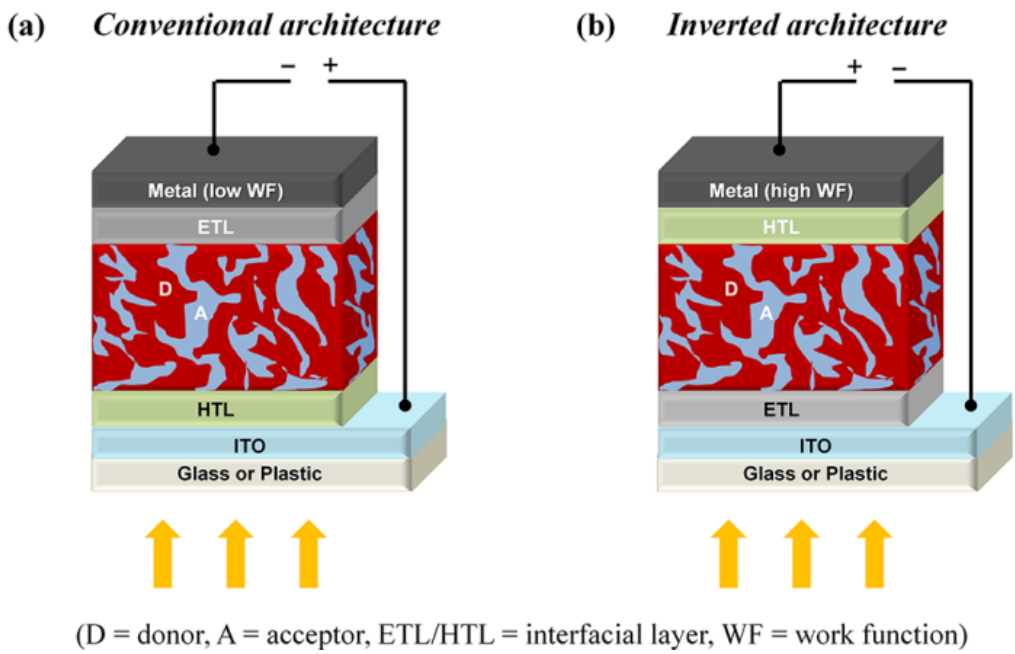

Figure 1-8. Bulk heterojunction schematic diagrams for (a) conventional architecture and (b) inverted architecture.

1.3.2. Working principle

The active layer of a bulk heterojunction (BHJ) OPV consists of a bicontinuous interpenetrating network of electron-donor (often conjugated polymers) and electron-acceptor materials (often fullerene derivatives). The concept of the BHJ was introduced to solve the limited exciton (hole-electron pair) diffusion length problem in previous types of OPVs, such as single-layer or bi-layer junctions. In BHJ structures, the large interfacial areas in the active layer lead to an efficient exciton dissociation. Once the exciton has been formed in the donor materials via the absorption of photons of light, the exciton diffuses through the active layer towards a donor/acceptor interface. If the exciton reaches this interface, the holes and electron separate with the result that holes and electrons travel towards the anode and the cathode through the donor and acceptor network, respectively (**Figure 1-9**).[77] Minor changes to the device or material conditions in the OPV affect each stage of the process and can result in significantly different efficiencies. Hence, to optimize the OPV devices, the key factors such as materials design, morphology, manipulation, and interface engineering must be thoroughly controlled.

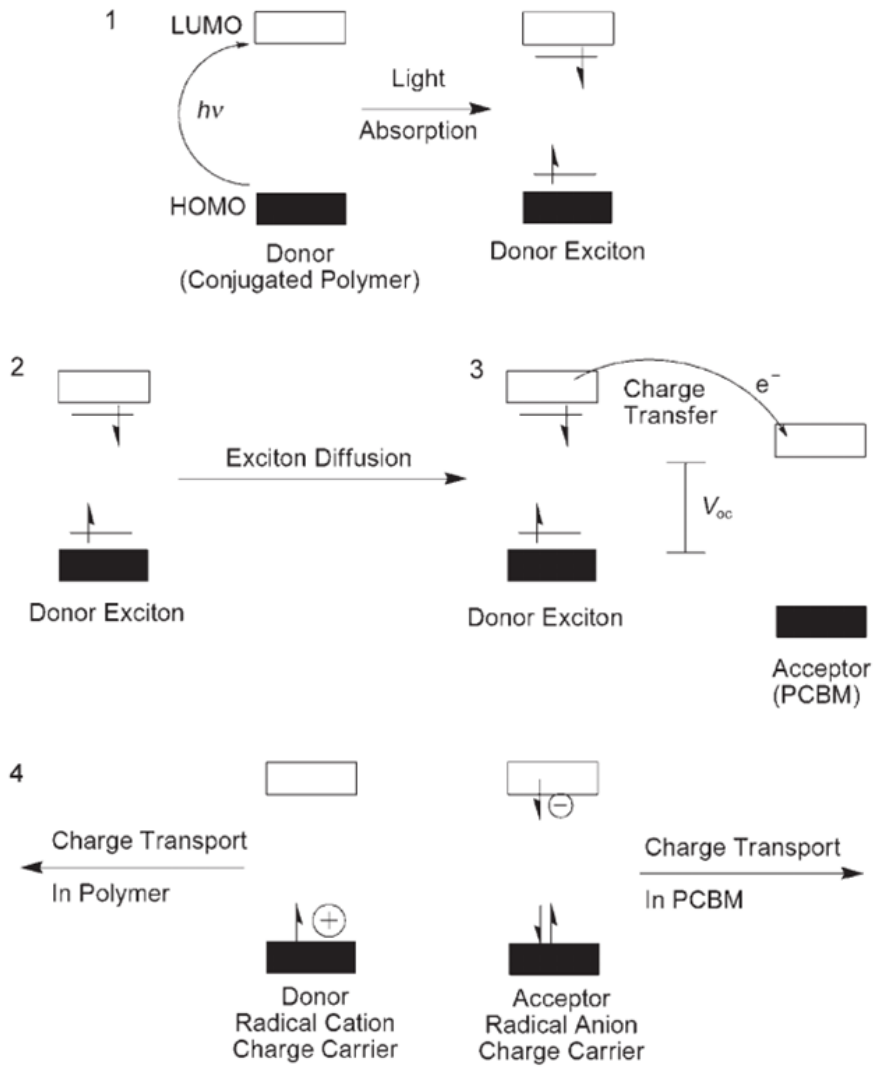

Figure 1-9. Working principles for BHJ OSC devices.[77]

1.3.3. Device characterization

The device performance of OPVs is determined by the power conversion efficiency (PCE), which is defined as the percentage of incident solar power (P_{in}) converted into electrical power (P_{max}). The value of P_{max} is multiply of three parameters: the short-circuit current density (J_{sc}), the open-circuit voltage (V_{oc}) and the fill factor (FF). Thus, the PCE of the device is determined using the following formula:

$$\mathrm{PCE} = \frac{P_{max}}{P_{in}} = \frac{J_{sc} \times V_{oc} \times FF}{P_{in}}$$

J_{sc} is the current density through the cell at zero bias (short circuited). J_{sc} is significantly influenced by the optical properties of active layer materials as well as the various charge loss mechanisms. Therefore, the band gap (range of absorbed wavelength of light), absorption coefficient (intensity of light absorption), and charge carrier mobility of materials should be considered.[78]

The V_{oc} is the maximum voltage of the device at zero current (open circuited). In general, V_{oc} is largely influenced by the energy offset between the HOMO energy level of the donor and a LUMO energy level of the acceptor. Recent studies have shown that the V_{oc} of BHJ OPV is linearly dependent on the energy of the interfacial charge-transfer (CT) state E_{CT} between the donor and acceptor materials as stated in the equation:

$$qV_{oc} \approx E_{CT} - 0.5 \text{ eV}$$

That is, between E_{CT} and qV_{oc} at room temperature there is an energy loss of around 0.5-0.6 eV, due to radiative/non-radiative losses, which can be reduced by decreasing the electronic coupling or by reducing the non-radiative recombination rate.[79,80]

The final term is the FF, which is defined as the ratio of the maximum possible power to the product of V_{oc} and J_{sc}, as shown in following formula:

$$FF = \frac{J_{MPP} * V_{MPP}}{J_{sc} * V_{oc}}$$

J_{MPP} is the current and V_{MPP} is the voltage at the maximum power point. The FF parameter is a measure of the squareness of the *J*-*V* characteristics of the solar cell. The FF are significantly influenced by the film morphology and the interfacial contact, so it is important to optimize the device fabrication process in order to attain the highest FF (**Figure 1-10**).[81]

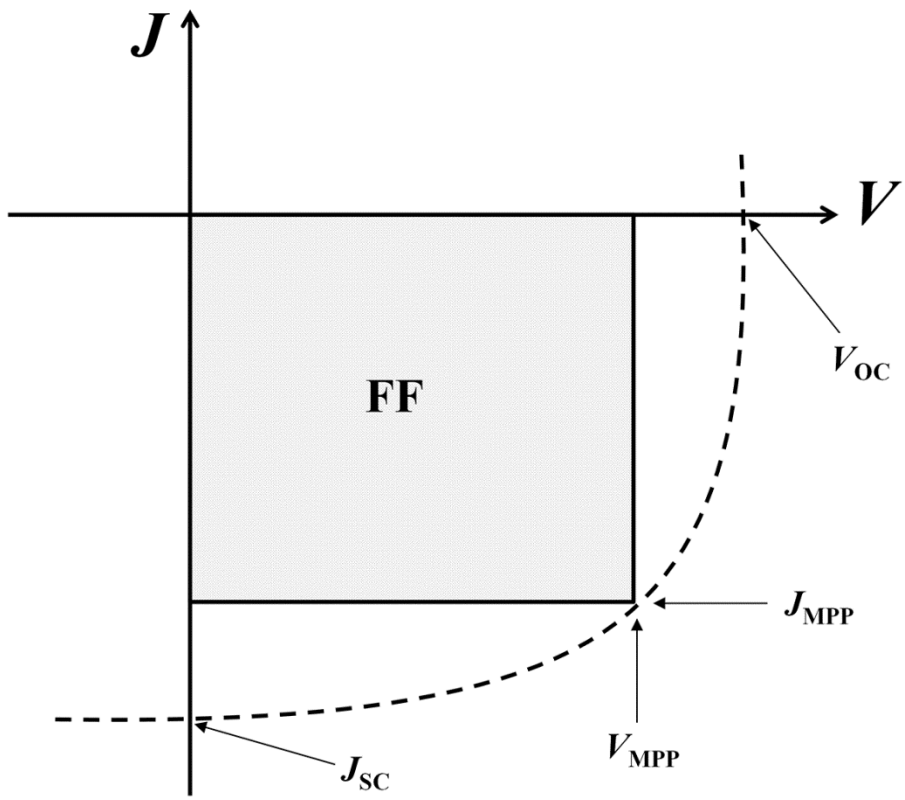

Figure 1-10. The typical current density–voltage (*J*–*V*) characteristics in OPV device.

1.4. Bis-lactam-based organic semiconducting materials

Over the past few decades, organic semiconducting materials have attracted a large amount of attention for their potential use in OFETs, OPVs, OLEDs, and sensors, owing to their possible implementation in flexible, large-area devices. Through in-depth research in this field, the performance of organic optoelectronic devices has improved drastically. Such progress is not only derived from optimization of the device architecture, but also from development of high-performance materials.

Among the many π-conjugated organic semiconducting materials, including small molecules and polymers, bis-lactam-based materials have attracted significant attention due to their distinct advantages: (1) a strong electron withdrawing ability owing to electron deficient properties of the lactam group, which facilitates electron injection and MOs control; (2) structural rigidity and planarity, promoted by intramolecular nonbonding interactions such as intramolecular H bonds between carbonyl oxygen and H atom on the thiophene unit or intramolecular S···O interactions between carbonyl oxygen and S atom on the thiophene unit; (3) facial *N*-alkylation or arylation, which yields a good material solubility and promotes the solid-state packing, which should benefit inter- and intra-molecular charge transport.[82] To this end, bis-lactam-based core units such as diketopyrrolopyrrole (DPP),[83-85] isoDPP,[86,87] isoindigo (II),[88,89] and thienoisoindigo (TII)[90,91] have been employed as efficient electron-withdrawing

building blocks, aimed at the achievement of high-performing small molecular or polymeric semiconducting materials (**Figure 1-11**).

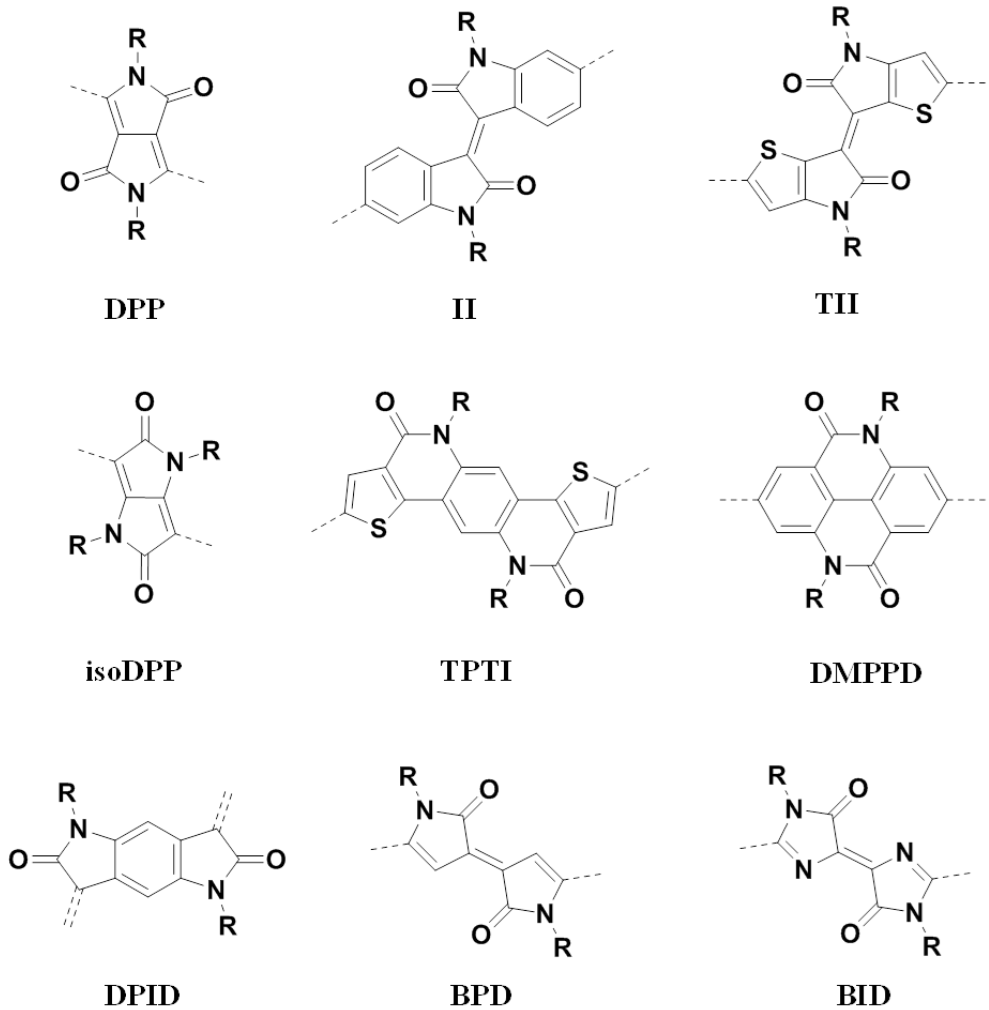

Figure 1-11. Chemical structures of reported bis-lactam-based building blocks.

1.4.1. Diketopyrrolopyrroles and there derivatives

Diketopyrrolopyrroles (DPPs) are one of the most extensively studied bis-lactam-based building blocks, with excellent semiconducting properties. Since the accidental discovery of bicyclic heterocyclic compound, 2,5-dihydropyrrolo[3,4-c]pyrrole-1,4-dione, by Farnum *et al.* in 1974[92] and the significantly improved synthetic pathway by Iqbal and coworkers in 1986, [93] DPP derivatives have been widely used in commercial pigment applications such as paints, plastics, fibers, and inks, owing to their bright red color, low solubility in common organic solvents and outstanding stability to heat.

Because of the synthetic limitations, 2,5-dihydropyrrolo[3,4-c]pyrrole-1,4-dione itself has not been synthesized. The major compound of known DPPs possess aromatic substituents at the 3 and 6 positions, such as diphenyl substituted DPPs (3,6-Diphenylpyrrolo[3,4-*c*]pyrrole-1,4(2*H*,5*H*)-diones, DPPP), dithienyl substituted DPP (3,6-Di(thiophen-2-yl)pyrrolo[3,4-*c*]pyrrole-1,4(2*H*,5*H*)-diones, DPPT), and difuranyl substituted DPP (3,6-Di(furan-2-yl)pyrrolo[3,4-*c*]pyrrole-1,4(2*H*,5*H*)-diones, DPPF) (**Figure 1-12**). As mentioned before, non-alkylated diaryl substituted DPPs exhibit very low solubility, which is advantageous for pigment applications. For example, the characteristic physical properties of DPPP are the high melting point (>350℃) and the extremely low solubility due to the strong π-π interactions and intermolecular hydrogen bonding between the lactam rings.[94] The *N*-alkylation of DPP improves the solubility,

thus easing the solution processability of OFETs and OPVs. Meanwhile, the aromatic substituents strongly influence the optical and electrical properties. DPPP-bearing small molecules and polymers have been used for their distinct photoluminescence and electroluminescence, but never attained high efficiencies in OPVs. The dihedral angle between the phenyl ring and the DPP unit is about 30°, and reduces the conjugation and the tendency to crystallize, leading to a low charge carrier mobility.[95] On the other hand, DPPT has thiophene rings in an anti-orientation with respect to each other and nearly coplanar with respect to the plane of the central DPP, as a result of the intramolecular H bonds between carbonyl oxygen and H atom on the thiophene unit.[96,97] As mentioned in chapter 1, the planar conformation can produce higher charge carrier mobility than the rated molecules; hence, DPPT is potentially suitable for optoelectronic applications. In addition, the charge polarity characteristics of DPPT derivatives can be easily tuned from p-, to ambipolar, to n-type through appropriate combination of electron donating or electron accepting segments. To this end, there are many examples in the literature of DPPT derivatives being successfully applied in OFETs and OPVs as active layer materials via solution processing, vacuum deposition, or crystallization.[98-103]

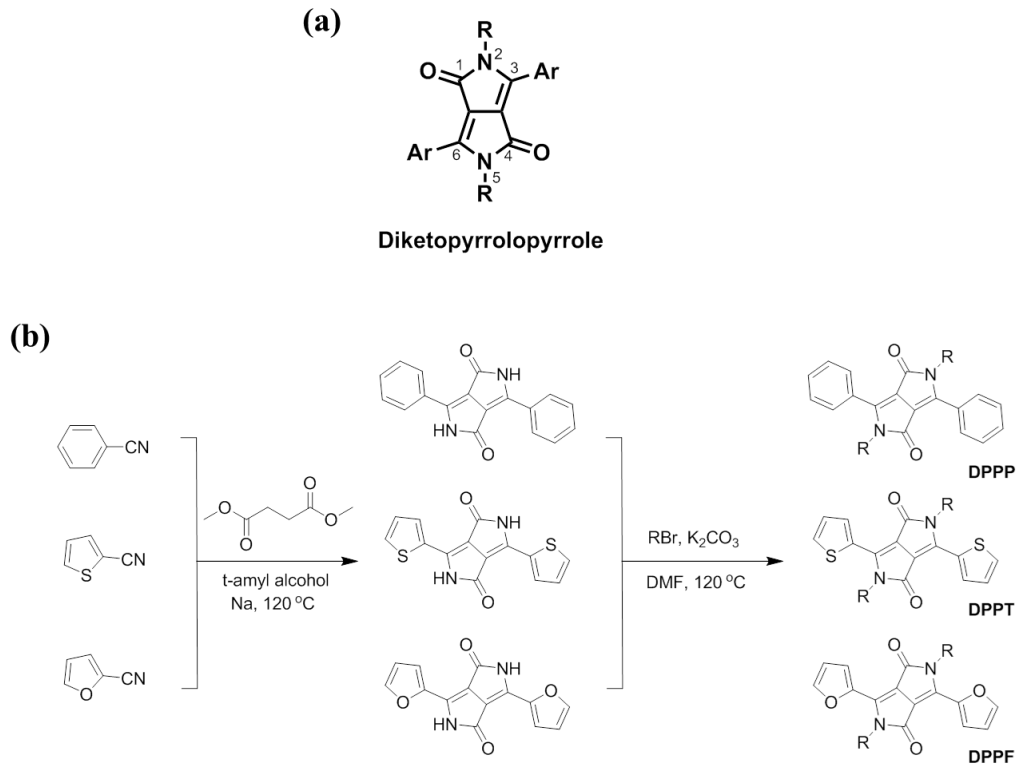

Figure 1-12. (a) General chemical structure of DPPs. (b) Synthetic routes of DPPP, DPPT, and DPPF.

1.4.2. Other bis-lactam containing molecules

After the successful use of DPP derivatives for optoelectronic applications, many other bis-lactam containing molecules have been created and employed as organic semiconductors. Among them, Isoindigo (II), a structural isomer of the well-known dye indigo, is one of the newest bis-lactam-based families of high performance materials. In 2010, Reyonlds *et al.* reported two II-based small molecules for OPVs,[104] and since then isoindigo has been recognized as a promising electron-deficient building block for synthetizing high performance conjugated materials. In addition, McCulloch and coworkers reported a new II derivative called thienoisoindigo (TII), [105] exhibiting a more rigid and planar structure owing to intramolecular S···O interactions between carbonyl oxygen and the S atom on the thiophene unit.

According to the mechanism shown in (**Figure 1-13**), II and TII can be easily prepared in two or three steps with high yield. As in the case of DPPs, through N-alkylation of core, II can be easily transformed into highly soluble materials. This characteristic, combined with their strong electron-withdrawing property, has attracted the attention of researchers and led to extensive application in OFETs and OPVs.[106-110] To this date, II and TII-based semiconductors have attained charge mobility of over 10 $cm^2\ V^{-1}\ s^{-1}$[91] and have also demonstrated balanced ambipolarity and excellent device stability.[111] In addition, II-based polymers generally possess a narrow band gap owing

to their low LUMO level, which facilitates the wide range of light absorption observed in these polymers. OPVs fabricated from II-based copolymers show a PCE of over 8% with high ambient stability.[112]

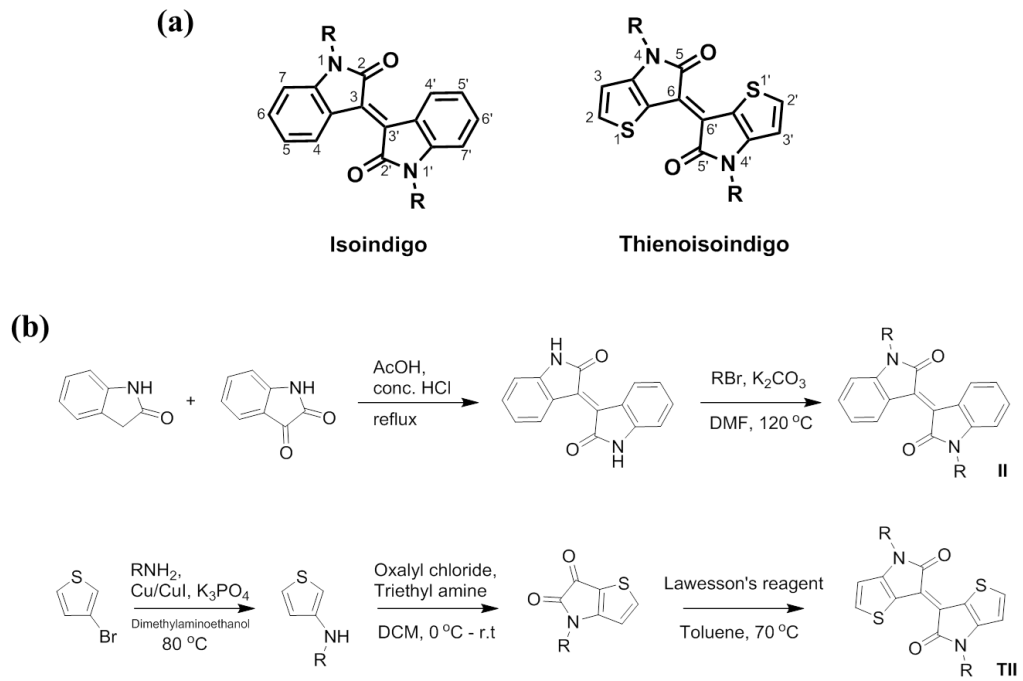

Figure 1-13. (a) General chemical structures of II and TII. (b) Synthetic routes of II and TII.

The DPP, II and TII have shown the most promising properties for use in OFETs and OPVs, which has inspired synthetic chemists to develop new bis-lactam-based materials. For example, bipyrrolydene-2,2'(1H,1'H)-dione, a synthetized pechmann

dye derivative, which has a coplanar structure, exhibits a strong electron-withdrawing property and, when incorporated into polymers, shows ambipolarity with high μ_e and μ_h in OFETs.[113] A structurally novel bis-lactam functionalized building block, pyrido[2,3,4,5-*lmn*]phenyanthridine-5,10-dione (DMPPD), was synthesized and incorporated into polymers with benzodithiophene, thus attaining a moderate PCE of 4.54% with a band gap above 2.1 eV.[114] Cao *et al.* designed and synthesized a new pentacyclic bis-lactam acceptor unit, thieno[2',3':5,6]-pyrido[3,4-*g*]thieno[3,2-c]isoquinoline-5,11(4H,10H)-dione (TPTI), and its copolymerization with thiophene provided a donor-acceptor type copolymer showed a PCE of 7.8%.[115] By replacing the benzene with 2,2'-bithiophene, a new bis-lactam unit, [7,7'-bidithieno[3,2-b:2',3'-*d*]pyridine]-5,5'(4*H*,4'*H*)-dione (BDTP), was also synthesized. A donor-acceptor type copolymer PThBDTP using BDTP as the acceptor building block and thiophene as the donor building block demonstrated a high PCE of over 9% (**Figure 1-14, Figure 1-15**).[116]

As mentioned above, the bis-lactam-based small molecules and polymers have shown promising properties and great success in OFETs and OPVs. Especially in known bis-lactam building units such as DPP and II, the relationship between structure and device properties has been established. However, further research is required in order to develop novel materials, because the performances of optoelectronic devices depend not only on the optimization of the device architecture but also on the discovery of high-performance materials. Therefore, it is necessary to develop new

building blocks through proper design strategy.

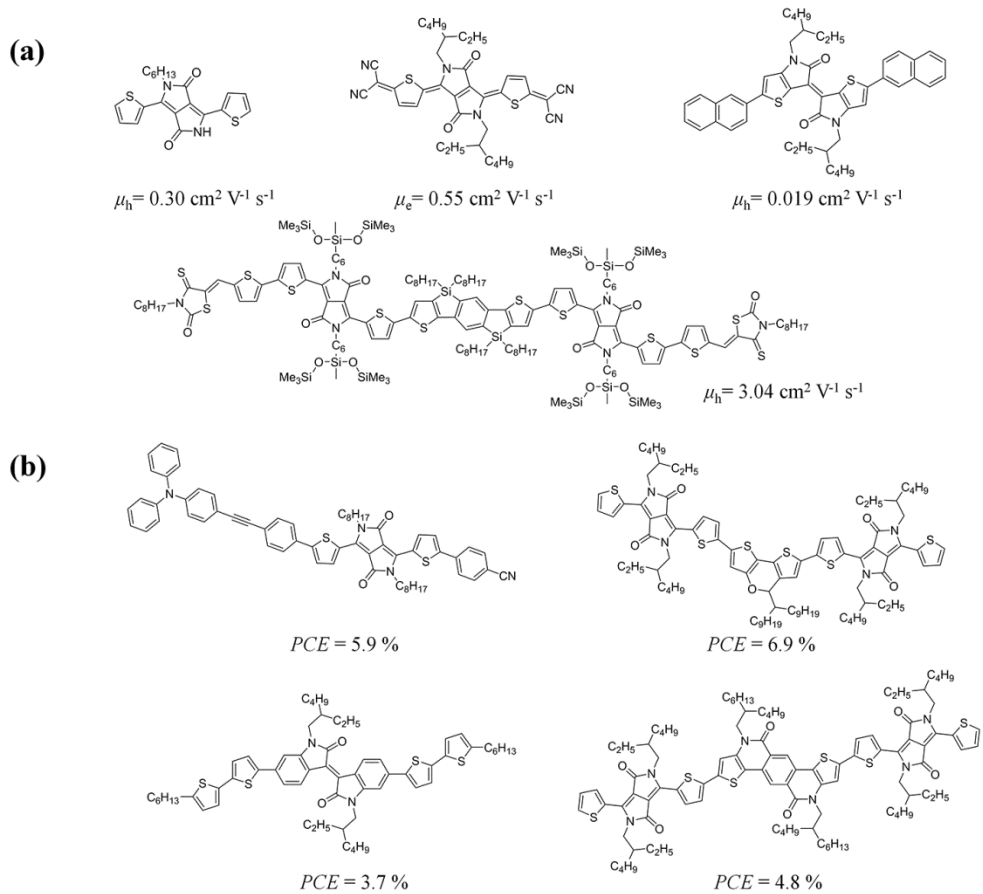

Figure 1-14. The representative bis-lactam-based small molecules for (a) OFETs and (b) OPVs.

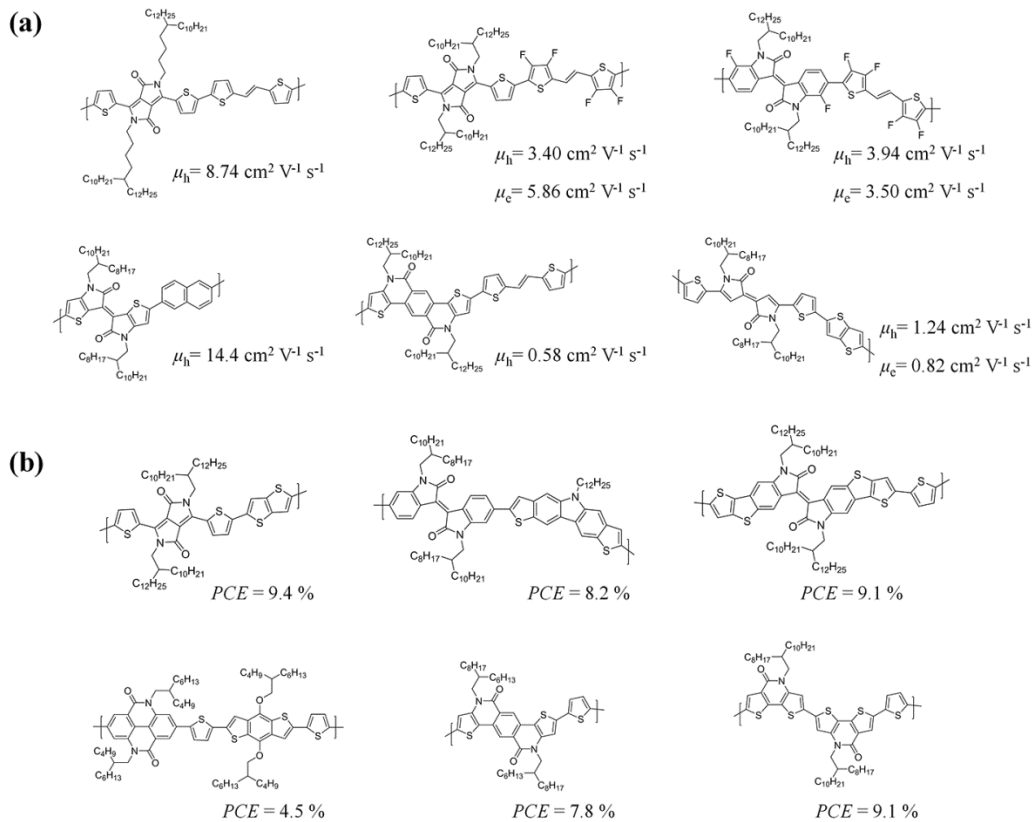

Figure 1-15. The representative bis-lactam-based conjugated polymers for (a) OFETs and (b) OPVs.

1.5. Research objective and contents of thesis

In this chapter, an overview of organic electronics, bis-lactam-based materials, and their optoelectronic properties was given. In recent years, bis-lactam-based materials, such as DPP and II have attracted significant attention as desirable electron-accepting building blocks, because of their high electron affinity driven by the electron withdrawing nature of the lactam units, their quasi-planar backbone structures, and the easy control over the MOs. These properties cooperatively yield outstanding charge carrier transport efficiencies in OFETs and OPVs.

The aim of the study described in this thesis is to investigate in detail the relationship between the molecular structure of bis-lactam-based materials and their electronic structure, optical and electrical properties, and semiconducting properties. For this reason, new DPP-based small molecules have been synthesized and studied with OFETs application.

In addition, I will discuss a novel electron-accepting bis-lactam building block, 3,7-dithiophen-2-yl-1,5-dialkyl-1,5-naphthyridine-2,6-dione (NTDT) and its derivatives. The electronic, thermal, photophysical, electrochemical, structural, and photovoltaic properties of NTDT-based copolymers have been studied in depth, in order to demonstrate the high potential for use of NTDT in organic optoelectronics.

The next three chapters consist of following contents:

Chapter 2. High-Mobility n-Type Organic Transistors Based on a Crystallized Diketopyrrolopyrrole Derivative

Chapter 3. A Novel Bis-Lactam Acceptor with Outstanding Molar Extinction Coefficient and Structural Planarity for Donor-Acceptor Type Conjugated Polymer

Chapter 4. Designing 1,5-Naphthyridine-2,6-dione-Based Conjugated Polymers for Higher Crystallinity and Enhanced Light Absorption to Achieve 9.63% Efficiency Polymer Solar Cells

1.6. References

[1] C. K. Chiang, C. R. Fincher, Y. W. Park, A. J. Heeger, H. Shirakawa, E. J. Louis, S. C. Gau, A. G. MacDiarmid, *Phys. Rev. Lett.* **1977**, *29*, 1098.

[2] C. K. Chiang, M. A. Druy, S. C. Gau, A. J. Heeger, E. J. Louis, A. G. MacDiarmid, Y. W. Park, H. Shirakawa, *J. Am. Chem. Soc.* **1978**, *100*, 1013.

[3] J. H. Burroiughes, D. D. C. Bradley, A. R. Brown, R. N. Marks, K. Mackay, R. H. Friend, P. L. Burns, A. B. Holms, *Nature* **1990**, *347*, 539.

[4] A. Kraft, A. C. Grimsdale, A. B. Holmes, *Angew, Chem. Int. Ed.* **1998**, *37*, 402.

[5] A. Tsumura, H. Koezuka, T. Ando, *Appl. Phys. Lett.* **1986**, *49*, 1210.

[6] G. Horowits, *Adv. Mater.* **1998**, *10*, 365.

[7] H. Minemawari, T. Yamada, H. Matsui, J. Y. Tsutsumi, S. Haas, R. Chiba, R. Kumai, T. Hasegawa, *Nature* **2011**, *475*, 364.

[8] J. Li, Y. Zhao, H. S. Tan, Y. Guo, C. A. Di, G. Yu, Y. Liu, M. Lin, S. H. Lim, Y. Zhou, H. Su, B. S. Ong, *Sci Rep* **2012**, *2*, 754.

[9] N. S. Sariciftci, L. Smilowitz, A. J. Heeger, F. Wudl, *Science* **1992**, *258*, 1474.

[10] S. Günes, H. Neugebauer, N. S. Sariciftci, *Chem. Rev.* **2007**, *107*, 1324.

[11] Y. Liang, L. Yu, *Acc. Chem. Res.* **2010**, *43*, 1227.

[12] E. Maryam, R. Federico, *Nature Photonics* **2016**, *10*, 434.

[13] D. T. McQuade, A. H. Hegedus, T. M. Swager, *J. Am. Chem. Soc.* **2000**, *122*, 12389.

[14] Y. Liang, Z. Tao, J. Chen, *Adv. Energy. Mat.* **2012**, *2*, 742.

[15] A. R. Brown, A. Pomp, C. M. Hart, D. M. Deleeuw, *Science* **1995**, *270*, 972.

[16] B. Crone, A. Dodabalapur, Y. Y. Lin, R. W Filas, Z. Bao, A. LaDuca, R. Sarpeshkar, H. E. Katz, W. Li, *Nature* **2000**, *403*, 521.

[17] J. Zaumseil, H. Sirringhaus, *Chem. Rev.* **2007**, *107*, 1296.

[18] M. Mas-Torrent, C. Rovira, *Chem. Soc. Rev.* **2008**, *37*, 827.

[19] Y. Yuan, G. Giri, A. L. Ayzner, A. P. Zoombelt, S. C. B. Mannsfeld, J. Chen, D. Nordlund, M. F. Toney, J. Huang, Z. Bao, *Nat. Commun.* **2014**, *5*, 3005.

[20] H. Jiang, C. Kloc, *MRS bulletin* **2013**, *38*, 28.

[21] J. Takeya, M. Yamagishi, Y. Tominari, R. Hirahara, Y. Nakazawa, T. Nishikawa, T. Kawase, T. Shimoda, and S. Ogawa, *Appl. Phys. Lett.* **2007**, *90*, 102120.

[22] T. Hasegawa and J. Takeya, Sci. Technol. *Adv. Mater.* **2009**, *10*, 024314.

[23] I.G. Lezama and A.F. Morpurgo, *MRS bulletin.* **2013**, *38*, 51.

[24] H. Yan, Z. Chen, Y. Zheng, C. Newman, J. R. Quinn, F. Dötz, M. Kastler, A. Facchetti, *Nature* **2009**, *457*, 679.

[25] I. Kang, H.-J. Yun, D. S. Chung, S.-K. Kwon, Y.-H. Kim, *J. Am. Chem. Soc.* **2013**, *135*, 14896.

[26] H.-R. Tseng, H. Phan, C. Luo, M. Wang, L. A. Perez, S. N. Patel, L. Ying, E. J. Kramer, T.-Q. Nguyen, G. C. Bazan, *Adv. Mater.* **2014**, *26*, 2993.

[27] V. Coropceanu, J. Cornil, D. A. S. Filho, Y. Olivier, R. Silbey, J. L. Brédas. *Chem. Rev*. **2007**, *107*, 926.

[28] F. Würthner, R. Schmidt, *ChemPhysChem* **2006**, *7*, 793

[29] H. Dong, C. Wang, W. Hu, *Chem. Commun.* **2010**, *46*, 5211.

[30] S. K. Park, T. N. Jackson, *Appl. Phys. Lett.* **2007**, *91*, 063514.

[31] B. J. Kim, H.-S. Lee, J. S. Lee, S. Cho, H. Kim, H. J. Son, H. Kim, M. J. Ko, S. Park, M. S. Kang, S. Y. Oh, B. S. Kim, J. H. Cho, *J. Phys. Chem. C* **2013**, *117*, 11479.

[32] M. S. Chen, J. R. Niskala, D. A. Unruh, C. K. Chu, O. P. Lee, J. M. J. Fréchet, *Chem. Mater.* **2013**, *25*, 4088.

[33] V. Vohra, K. Kawashima, T. Kakara, T. Koganezawa, I. Osaka, K. Takimiya, H. Murata, *Nat. Photonics* **2015**, *9*, 403.

[34] J. Roncali, *Chem. Rev.* **1997**, *97*, 173.

[35] J. Roncali, *Macromol. Rapid Commun.* **2007**, *28*, 1761.

[36] M. Kertez, J. Koller and A. Azman, *J. Chem. Phys.* **1977**, *67*, 1180.

[37] W. P. Su, J. R. Schrieffer and A. J. Heeger, *J. Phys. Rev. Lett.* **1979**, *42*, 1698.

[38] J. P. Lowe and S. A. Kafafi, *J. Am. Chem. Soc.* **1984**, *106*, 5837.

[39] J. L. Brédas, G. B. Street, B. Thémans and J. M. André, *J. Chem. Phys.* **1985**, *83*, 1323.

[40] G. Li, R. Zhu and Y. Yang, *Nature Photon.* **2012**, *6*, 153.

[41] R. S. Loewe, P. C. Ewbank, J. Liu, L. Zhai, R. D. McCullough,

Macromolecules **2001**, *34*, 4324.

[42] Y.-Y. Noh, R. Azumi, M. Goto, B.-J. Jung, E. Lim, H.-K. Shim, Y. Yoshida, K. Yase, D.-Y. Kim, *Chem. Mater.* **2005**, *17*, 3861.

[43] Q. T. Zhang and J. M. Tour, *J. Am. Chem. Soc.* **1997**, *119*, 5065.

[44] T. Xu, L. Yu, *Materials today* **2014**, *17*, 11.

[45] A. Facchetti, *Chem. Mater.* **2011**, *23*, 733.

[46] R. C. Hilborn, *Am. J. Phys.* **1982**, *50*, 982.

[47] M. Nakahara, *Baifukan.* **2002**, 108.

[48] M. S. Vezie, S. Few, I. Meager, G. Pieridou, B. Dörling, R. S. Ashraf, A. R. Goni, H. Bronstein, I. McCulloch, S. C. Hayes, M. Campoy-Quiles, J. Nelson, *Nature Materials* **2016**, *15*, 746.

[49] P. Horowitz and W. Hill, *The Art of Electronics 2nd Ed.* Cambridge University Press, **1990**.

[50] D. J. Gundlach, J. E. Royer, S. K. Park, S. Subramanian, O. D. Jurchescu, B. H. Hamadani, A. J. Moad, R. J. Kline, L. C. Teague, O. Kirillov, C. A. Richter, J. G. Kushmerick, L. J. Richter, S. R. Parkin, T. N. Jackson and J. E. Anthony, *Nat Mater*, **2008**, *7*, 216.

[51] A. Facchetti, M. H. Yoon and T. J. Marks, *Advanced Materials*, **2005**, *17*, 1705.

[52] H. Peisert, M. Knupfer and J. Fink, *Applied Physics Letters*, **2002**, *81*, 2400.

[53] A. R. Brown, D. M. de Leeuw, E. J. Lous, E. E. Havinga, *Synth. Met.* **1994**,

66, 257.

[54] C. A. Di, Y. Q. Liu, G. Yu, D. B. Zhu, *Acc. Chem. Res.* **2009**, *42*, 1573.

[55] Y. Shirota, H, Kageyama, *Chem. Rev.* **2007**, *107*, 953.

[56] J. Zaumseil, H. Sirringhaus, *Chem. Rev.* **2007**, *107*, 1296.

[57] T. D. Anthopoulos, G. C. Anyfantis, G. C. Papavassiliou, D. M. de Leeuw, *Appl. Phys. Lett.* **2007**, *90*, 122105.

[58] NREL Best Research-Cell Efficiencies, **2015**, http://www.nrel.gov /ncpv/images/efficiency_chart.jpg.

[59] C. J. Brabec, *Sol. Energ. Mater. Sol. Cells* **2004**, *83*, 273.

[60] M. Kaltenbrunner, MM. S. White, E. D. Glowacki, T. Sekitani, T. Someya, N. S. Sariciftci and S. Bauer, *Nat. Commun.* **2012**, *3*, 770.

[61] S. R. Forrest, *Nature* **2004**, *428*, 911.

[62] Y. Yu, J. Gao, J. C. Hummelen, F. Wudl, A. J. Heegre, *Science* **1995**, *270*, 1789.

[63] L. Dou, J. You, Z. Hong, Z. Xu, G. Li, R. A. Street, Y. Yang, *Adv. Mater.* **2013**, *26*, 6642.

[64] J. C. Hummelen, B. W. Knight, F. LePeq and F. Wudl, *J. Org. Chem.* **1995**, *60*, 532.

[65] G. Gustafsson, Y. Cao, G. M. Treacy, F. Klavetter, N. Colaneri and A. J. Heeger, *Nature* **1992**, *357*, 477.

[66] Y. Yang and A. J. Heeger, *Appl. Phys. Lett.* **1994**, *64*, 1245.

[67] J. Jang, J. Ha and K. Kim, *Thin Solid Films* **2008**, *516*, 3152.

[68] R. Steim, F. R. Kogler and C. J. Brabec, *J. Mater. Chem.* **2010**, *20*, 2499.

[69] M. P. de Jong, L. J. van Ijzendoom and M. J. Ad. Voigt, *Appl. Phys. Lett.* **2000**, *77*, 2255.

[70] M. Jorgensen, K. Norrman, S. A. Gevogyan, T. Tromholt, B. Andreasen and F. C. Krebs, *Adv. Mater.* **2012**, *24*, 580.

[71] C. B. Nielsen, S. Holliday, H.-Y. Chen, S. J. Cryer, I. McCulloch, *Acc. Chem. Res.* **2015**, *48*, 2803.

[72] D. Meng, D. Sun, C. Zhong, T. Liu, B. Fan, L. Huo, Y. Li, W. Jiang, H. Choi, T. Kim, J. Y. Kim, Y. Sun, Z. Wang, A. J. Heeger, *J. Am. Chem. Soc.* **2016**, *138*, 375.

[73] A. Watanabe and A. Kasuya, *Thin Solid Films* **2005**, *483*, 358.

[74] G. Li, C.-W. Chu, V. Shrotriya, J. Huang and Y. Yang, *Appl. Phys. Lett.* **2006**, *88*, 253503.

[75] D. Tordera, M. Kuik, Z. D. Rengert, E. Bandiello, H. J. Bolink, G. C. Bazan and T.-Q. Nguyen, *J. Am. Chem. Soc.* **2014**, 13*6*, 8500.

[76] H. Choi, C.-K. mai, H.-B. Kim, J. Jeong, S. Song, G. C. Bazan, J. Y. Kim, A. J. Heeger, *Nat. Commun.* **2015**, *6*, 7348.

[77] B. C. Thompson, J. M. J. Fréchet, *Angew. Chem. Int. Ed.* **2008**, *47*, 58.

[78] M. Padilla, B. Michl, B. Thaidigsmann,W. Warta, M. C. Schubert, *Sol. Energy Mater. Sol. Cells* **2014**, *120*, 282.

[79] C. Deibel, T. Strobel, V. Dyakonov, *Adv. Mater.* **2010**, *22*, 4097.

[80] Z. Yunlong, J. H. Russell, *Appl. Mater. Interfaces* **2015**, *7*, 18306.

[81] B. Qi and J. Wang, *Phys. Chem. Chem. Phys.* **2013**, *15*, 8972.

[82] X. Guo, A. Facchetti, T. J. Marks, *Chem. Rev.* **2014**, *114*, 8943.

[83] S. Subramaniyan, F. S. Kim, G. Ren, H. Li, S. A. Jenekhe, *Macromolecules* **2012**, *45*, 9029.

[84] H. Choi, S. J. Ko, T. Kim, P. O. Morin, B. Walker, B. H. Lee, M. Leclerc, J. Y. Kim, A. J. Heeger, *Adv. Mater.* **2015**, *27*, 3318.

[85] T. Ma, K. Jiang, S. Chen, H. Hu, H. Lin, Z. Li, J. Zhao, Y. Liu, Y.-M. Chang, C.-C. Hsiao, H. Yan, *Adv. Energy Mater.* **2015**, *5*, 1501282.

[86] S. Lu, M. Drees, Y. Yao, D. Boudinet, H. Yan, H. Pan, J. Wang, Y. Li, H. Usta, A. Facchetti, *Macromolecules* **2013**, *46*, 3895.

[87] X. Guo, S. R. Puniredd, B. He, T. Marszalek, M. Baumgarten, W. Pisula, K. Müllen, *Chem. Mater.* **2014**, *26*, 3595.

[88] R. Stalder, J. Mei, K. R. Graham, L. A. Estrada, J. R. Reynolds, *Chem. Mater.* **2014**, *26*, 664.

[89] P. Deng, Q. Zhang, *Polym. Chem.* **2014**, *5*, 3298.

[90] R.S. Ashraf, A.J. Kronemeijer, D.I. James, H. Sirringhaus, I. McCulloch, *Chem. Comm.* **2012**, 48, 3939.

[91] G. Kim, S. Kang, G. K. Dutta, Y.K. Han, T.J. Shin, Y.Y. Noh, C. Yang, *J. Am. Chem. Soc.*, **2014**, 136, 9477.

[92] D. G. Farnum, G. Mehta, G. G. I. Moore, F. P. Siegal, *Tetrahedron Letters*

1974, *29*, 2549.

[93] Z. Hao, A. Iqbal, *Chemical Society Reviews* **1997**, *26*, 203.

[94] A. Iqbal, L. Cassar, EP 61426 Ciba-Geigy, **1982**.

[95] C. Kanimozhi, M. Naik, N. Y. Gross, E. K Burnett, A. L. Briseno, T. D. Anthopoulos, S. Patil, *J. Phys. Chem. C* **2014**, *118*, 11536.

[96] C. B. Nielsen, M. Turbiez, I. McCulloch, *Adv. Mater.* **2013,** *25*, 1859.

[97] M. A. Naik, N. Venkatramaiah, C. Kanimozhi, S. Patil, *The Journal of Physical Chemistry C* **2012**, *34*, 159.

[98] B. Tieke, A. R. Rabindranath, K. Zhang, Y. Zhu, *Beilstein J. Org. Chem.* 2010, **6**, 830;

[99] S. Qu, H. Tian, *Chem. Commun.* **2012**, *48*, 3039.

[100] C. B. Nielsen, M. Turbiez, I. McCulloch, *Adv. Funct. Mater.* **2013**, *25*, 1859.

[101] D. Chandran, K.-S. Lee, *Macromol. Res.* **2013**, *21*, 272.

[102] Y. Li, P. Sonar, L. Murphy, W. Hong, *Energy Environ. Sci.* **2013**, *6*, 1684.

[103] M. Kaur, D. H. Choi, *Chem. Soc. Rev.*, **2015**, *44*, 58.

[104] J. Mei, K. R. Graham, R. Stalder, J. R. Reynolds, *Org. Lett.* **2010**, 12, 660 .

[105] R.S. Ashraf, A.J. Kronemeijer, D.I. James, H. Sirringhaus, I. McCulloch, *Chem. Comm.* **2012**, 48, 3939.

[106] E. Wang, W. Mammo, M.R. Andersson, *Adv. Mater.* **2014**, 26, 1801

[107] T. Lei, J.-H. Dou, Z.-J. Ma, C.-H. Yao, C.-J. Liu, J.-Y. Wang, J. Pei, *J. Am. Chem. Soc.* **2012**, 134, 20025.

[108] T. Lei, J.-H. Dou, J. Pei, *Adv. Mater.* **2012,** 24, 6457.

[109] W. Elsawy, C.-L. Lee, S. Cho, S.-H. Oh, S.-H. Moon, A. Elbarbary, J.-S. Lee, *Phys. Chem. Chem. Phys.* **2013**, 15, 15193.

[110] G. Kim, S. Kang, G.K. Dutta, Y.K. Han, T.J. Shin, Y.Y. Noh, C. Yang, *J. Am. Chem. Soc.*, **2014**, 136, 9477.

[111] Y. Gao, Y. Deng, H. Tian, J. Zhang, D. Yan, Y. Geng, F. Wang, *Adv. Mater.* **2017**, *29*, 1606217.

[112] Y. Deng, J. Liu, J. Wang, L. Liu, W. Li, H. Tian, X. Zhang, Z. Xie, Y. Geng and F. Wang, *Adv*. *Mater*. 2**014**, *26*, 471.

[113] Z. Cai, H. Luo, P. Qi, J. Wang, G. Zhang, Z. Liu, D. Zhang, *Macromolecules* **2014**, *47*, 2899.

[114] M. Liu, Y. Liang, P. Chen, D. Chen, K. Liu, Y. Li, S. Liu, X. Gong, F. Huang, S.-J. Su, Y. Cao, *J. Mater. Chem. A* **2014**, *2*, 321.

[115] J. Cao, Q. Liao, X. Du, L. Ding, *Energy Environ. Sci.* **2013**, *6*, 3224.

[116] J. Cao, C. Zuo, B. Du, X. Qiu, L. Ding, *Chem*. *Commun*. **2015**, *51*, 12122.

Chapter 2. High-Mobility n-Type Organic Transistors Based on a Crystallized Diketopyrrolopyrrole Derivative

2.1. Introduction

Over the past decade, extensive studies of organic field-effect transistors (OFETs) have resulted in the development of a few high-performing organic semiconducting materials, with charge carrier mobilities exceeding those of amorphous silicon.[1-4] Although remarkable developments in p-channel organic semiconductors have been achieved, the field of n-channel organic semiconductors has stagnated due to low charge carrier transport efficiencies, which are closely related to inherent instabilities and inappropriate frontier molecular orbitals (MOs).[5] It is therefore imperative to work toward developing new n-channel semiconducting materials with rationally engineered MOs for practical applications (e.g. CMOS, p-n junctions).[6] To realize high-performing n-type organic semiconductors in OFET applications, several crucial prerequisites must be met in the design of the materials. First, highly crystalline strongly fixed structures with a coplanar molecular conformation in the solid-state are required to ensure dense packing, which secures efficient charge carrier transport. In addition, a high electron affinity (a low lowest unoccupied molecular orbital (LUMO) of below –4.0 eV) should be obtained by introducing strong electron-deficient

functionalities that improve electron injection from the contact electrodes to the π-conjugated backbones.[7] The incorporation of aliphatic units with appropriate lengths can afford organic semiconductors with enhanced solubility in organic solvents and a high crystallinity in the condensed state. Such materials can be applied to the fabrication of excellent solution-processed single-crystal OFETs (SC-OFETs).[8,9]

Among the possible π-conjugated organic semiconducting building blocks, diketopyrrolopyrroles (DPP) have attracted significant attention due to their structural strength, driven by strong π-π stacking in the solid state, their quasi-planar backbone structures,[10-12] and the facile control over the MOs, which yields outstanding charge carrier transport efficiencies in organic photovoltaics (OPVs) with DPP-based low-band gap polymers.[13] Even though significant efforts have been made to improve electrical properties of OFETs based on DPP derivatives, high-performance n-type DPP derivatives[14-16,31,32] have less developed than p-type ones[17-28] because of difficulties in securing both low-lying stabilized LUMOs and high crystallinity of films. To realize n-type molecules, strong electron-withdrawing substituents can effectively lower the LUMO and, hence, improve electron injection from the contact electrodes. To this end, dicyanomethylene-substituted quinoidal structures have strong electron-withdrawing properties and show electrochemical amphoteric electrochemical redox behaviors. Derivatives of such structures based on oligothiophene,[29] tetrathienoquinoid,[30] and DPP[31,32] have been applied toward high-performing n-type or ambipolar OFETs. Zhu and coworkers reported that dicyanomethylene-substituted DPP-containing quinoidal

small molecules 1 and 2 (see **Figure 2-1**c for their structures) yielded energy levels that were adequate for the preparation of air-stable n-type organic semiconductors.[31] Efficient electron injection and a high electron mobility (μ_e) up to 0.55 $cm^2\ V^{-1}\ s^{-1}$ in 1 were achieved by vacuum-evaporation procedures, and 0.35 $cm^2\ V^{-1}\ s^{-1}$ was achieved in 2 by solution-processing procedures. Although typical n-type organic semiconductors with conserved aromaticity exhibit excellent electrical performances, studies of aromatic DPP-based semiconductors are rare, particularly for n-type semiconductors. Dicyanovinyl is similar to the dicyanomethylene unit and is one of the strongest electron-withdrawing functionalities. The unit conserves aromaticity when introduced into an aromatic core. The vinyl component of the dicyanovinyl substituents can extend the conjugation length without distorting the backbone structure; thus, such structures can yield efficient intermolecular π-π interactions upon introduction of dicyanovinyl units. The properties are expected to be distinct from those of dicyanomethylene-substituted compounds.[33] Moreover, the dicyanovinyl group can be readily synthesized from various aromatic aldehyde-containing cores to control the energy levels, crystallinity, and charge carrier properties.[34] Hence, it is worth considering dicyanovinyl-substituted π-conjugated organic material systems for further investigations as high-crystallinity n-type organic semiconductors.

Herein, I designed a dicyanovinyl-substituted DPP-based n-channel organic semiconductor, 2,2'-(5,5'-(2,5-bis(2-ethylhexyl)-3,6-dioxo-2,3,5,6-tetrahydropyrrolo[3,4-c]pyrrole-1,4-diyl)bis(thiophene-5,2-diyl))bis(methan-1-yl-1-ylidene)dimalononitrile

(DPP-T-DCV) (see **Figure 2-1**a). The strong electron-withdrawing dicyanovinyl units in DPP-T-DCV stabilize the LUMO level. The solubility and crystallinity are slightly higher than those of dicyanomethylene-substituted quinoidal molecule 1. The outstanding self-assembly characteristics and good solubility render the newly synthesized DPP-T-DCV useful as an organic semiconductor for solution-processed n-channel SC-OFETs, with an excellent μ_e (μ_e up to 0.96 $cm^2 V^{-1} s^{-1}$).

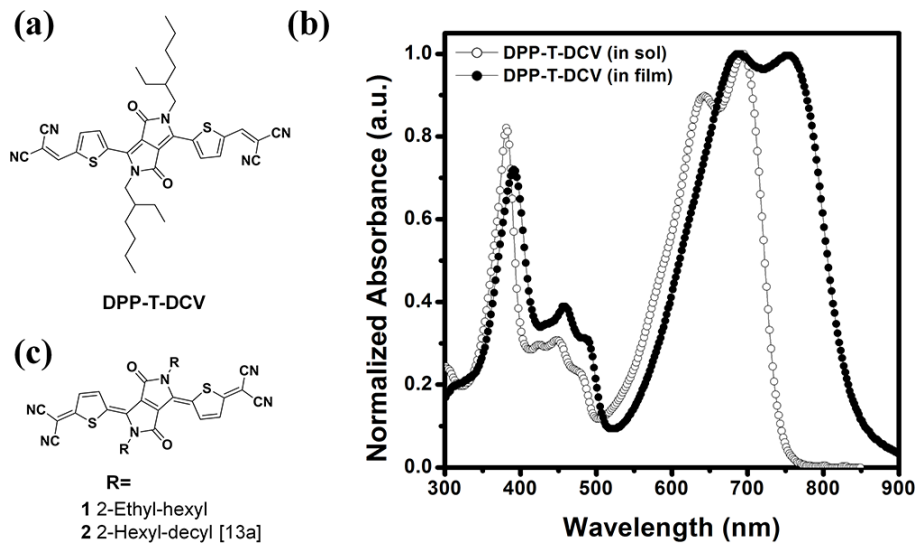

Figure 2-1. (a) Molecular structure of DPP-T-DCV. (b) UV-vis absorption spectra of DPP-T-DCV in the solution and thin film states. (c) Molecular structure of the reference quinoidal molecules 1 and 2.

2.2. Results and Discussion

2.2.1 Optical absorption and frontier orbital levels

The characteristic features of the primary chemical structure and the molecular stacking effects in the solid-state were analyzed by UV-vis absorption spectroscopy in both the solution state (1.0×10^{-5} M, chloroform) and the thin solid-state film state (a spin-coated film on quartz). As shown in **Figure 2-1**b, DPP-T-DCV exhibited a maximum absorption (λ_{max}^{abs}) at 690 nm in solution, whereas the reference core moiety, DPP-T (compound b), showed a λ_{max}^{abs} at 550 nm. The sequentially alternating intramolecular electron donor (thiophene) and acceptor (DPP and dicyanovinylene) moieties in DPP-T-DCV produced strong intramolecular charge transfer (ICT), which substantially decreased the energy band gap and increased the intensity of the resolvable vibronic peak at low energies (690 nm). In the solid-state film, the absorption spectrum of DPP-T-DCV broadly spanned the long wavelength region (550–900 nm). A bathochromic spectral shift and a new strong absorption band were observed in the film state (755 nm), indicating that strong intermolecular interactions most probably resulted from π–π interactions.

To estimate the frontier MO energies, photoelectron spectroscopy analysis of the solid-state films (vacuum-deposited) was carried out (check **Figure 2-2**). The highest

occupied molecular orbital (HOMO) energy level was determined to be –5.93 eV, and the LUMO energy level (–4.45 eV) was measured from the optical band gap (E_g: 1.48 eV). The optical and photoelectron spectroscopy results were supported by theoretical quantum chemical calculations using Gaussian09 at the B3LYP level with the 6-31G basis set.[35] The calculated HOMO/LUMO values for DPP-T-DCV (HOMO: –5.84 eV, LUMO : –4.03 eV) based on the optimized geometry agreed well with the experimental values. These results suggest that DPP-T-DCV is highly suitable for the preparation of high-mobility n-type OFETs.

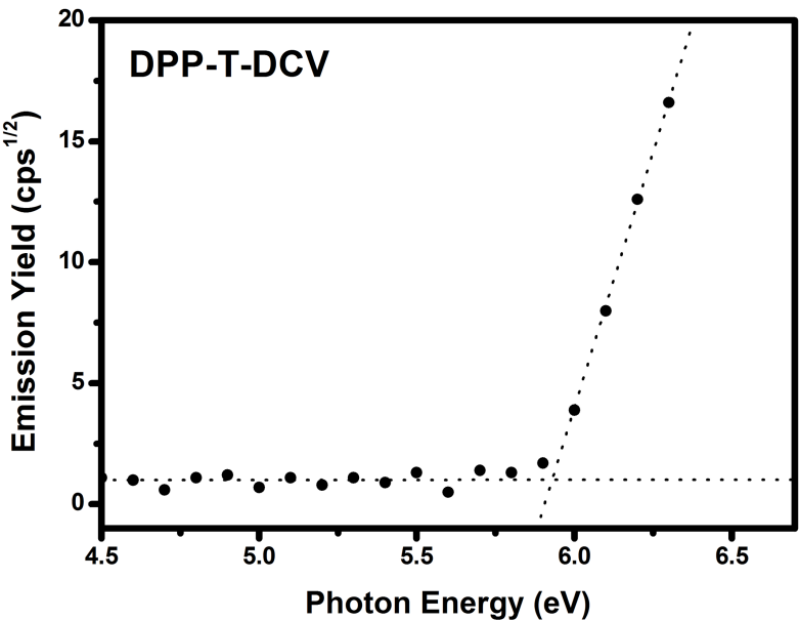

Figure 2-2. Photoelectron spectra of the DPP-T-DCV film. The crossing point of the background and yield curves indicates the work function.

2.2.2. OFET performance

To take advantage of the structural and energetic benefits of DPP-T-DCV, I prepared highly crystalline active layers for OFET fabrication using the "solvent–vapor evaporation crystal growth method", as described previously.[36] SiO_2/Si substrates were leaned against the inner wall of a 20 mL vial containing a 0.1 wt% solution of DPP-T-DCV in dichloromethane. Spontaneous evaporation of solvent produced high-quality elongated two-dimensional DPP-T-DCV crystals fixed firmly on the substrates. Neat terrace topographies with an average step height of 11.6 Å were observed by atomic force microscopy (AFM), which resulted in good charge carrier transport characteristics due to the highly ordered layered structures, see **Figure 2-3**. The crystal thickness (50–200 nm) was estimated using AFM and was found to be appropriately thin for use in single-crystalline devices. Single crystals were used to fabricate and evaluate top-contact SC-OFETs that exhibited an μ_e up to 0.96 $cm^2 V^{-1} s^{-1}$ with an on/off current ratio of ~10^5 (see **Figure 2-3**, **Table 1**). To the best of our knowledge, this is the first report of an SC-OFET investigation using DPP-containing derivatives.

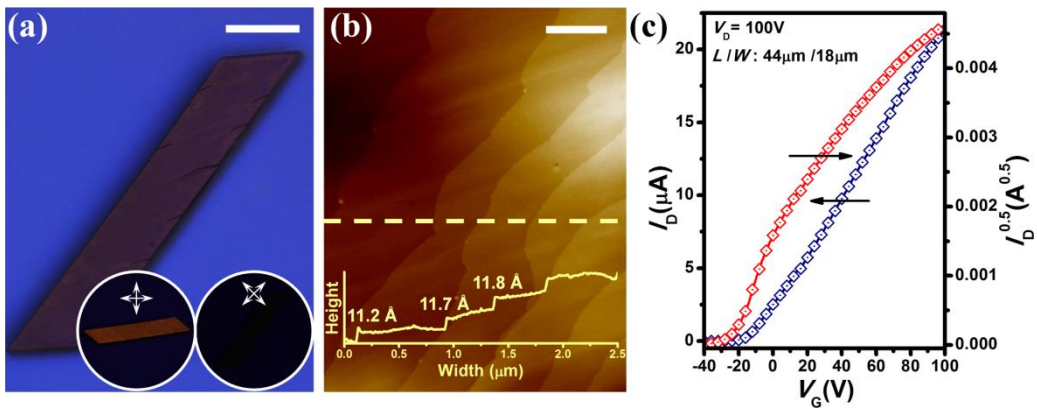

Figure 2-3. (a) OM images of the DPP-T-DCV crystal (scale bar: 20 μm, insets in circles show the birefringence images of the same crystal collected by polarized optical microscopy). (b) AFM image of the film surface of the DPP-T-DCV crystal device (scale bar: 1 μm, inset: thickness profile along the yellow dashed line). (c) Transfer characteristics of the DPP-T-DCV crystal device.

For practical applications, I fabricated and evaluated bottom-gate, top-contact vacuum-deposited polycrystalline OFETs using surface-treated SiO_2/Si substrates for various substrate temperatures (T_{SUB}). Polycrystalline DPP-T-DCV devices exhibited effective electron transport characteristics, as shown in **Figure 2-4** and **Table 1**. As shown in **Table 1**, the μ_e values increased dramatically up to 0.64 $cm^2 V^{-1} s^{-1}$ with an on/off current ratio of ~10^4, when deposited on an octadecyltrichlorosilane (ODTS)-treated substrate at a T_{SUB} of 120℃, which significantly influenced the film morphology and grain size. The dependence of morphology on T_{SUB} was investigated by examining the surfaces of the device channel areas by AFM. Substantial increases in the grain size occurred as a result of increases in T_{SUB}, as shown in **Figure 2-4**; however, the mobility values were slightly lower than those of the SC-OFETs due to the plentiful grain boundaries, impurities, and defects in the polycrystalline state. Nonetheless, the average μ_e exceeded 0.4 $cm^2 V^{-1} s^{-1}$ even in vacuum-deposited polycrystalline state which is highly favorable for next-generation electronics applications, because of highly ordered terrace structured grains with sufficiently large sizes.

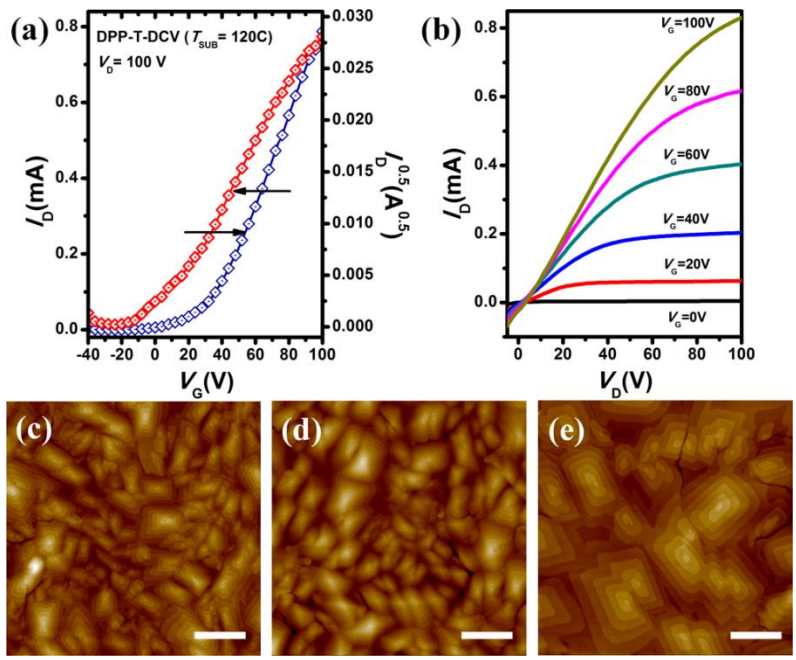

Figure 2-4. (a) Transfer and (b) output characteristics of the vacuum-deposited DPP-T-DCV film. AFM images (scale bar: 1 μm) of the vacuum-deposited DPP-T-DCV films on the ODTS-treated SiO_2/Si substrate at TSUB of (c) 100℃, (d) 120℃, (e) 140℃.

Table 2-1. Characterized electrical properties of the OFET devices.

Sample	μ_e [$cm^2\ V^{-1}\ s^{-1}$][a)]	I_{on}/I_{off}	V_{th}[V][b)]	n[c)]
SC-OFETs device[d)]	9.6×10^{-1} (7.0×10^{-1} ± 2.4×10^{-1})	10^5	–25	8
VD film (T_{SUB}=RT)[e)]	8.8×10^{-4} (7.2×10^{-4} ± 1.2×10^{-4})	10^3	10	10
VD film (T_{SUB}=70°C)[e)]	1.1×10^{-1} (4.1×10^{-2} ± 2.8×10^{-2})	10^3	7	10
VD film (T_{SUB}=100°C)[e)]	4.7×10^{-1} (3.0×10^{-1} ± 9.3×10^{-2})	10^3–10^4	–14	10
VD film (T_{SUB}=120°C)[e)]	6.4×10^{-1} (3.9×10^{-1} ± 9.4×10^{-2})	10^3–10^4	–19	10
VD film (T_{SUB}=140°C)[e)]	5.5×10^{-1} (4.8×10^{-1} ± 5.0×10^{-2})	10^3–10^4	–21	10

[a)]Maximum and average electron mobility values with standard deviations in the parentheses; [b)]Average threshold voltage; [c)]Number of devices tested; [d)]Devices fabricated by the solvent evaporation crystal growth technique; [e)]Device fabricated by vacuum deposition techniques using an ODTS-treated SiO_2/Si substrate.

2.2.3. Structural analysis

The structural origin of the excellent electronic properties was examined by conducting geometry optimization calculations based on density functional theory using Gaussian09 at the B3LYP level with the 6-31G basis set. The optimized geometry included a coplanar conformation with a small dihedral angle (< 5.0°) between the DPP core unit and the thiophenyl counterpart, as shown in **Figure 2-5**; thus, the quasi-planar conformation greatly enhanced the μ_e through strong π-π interactions and π-orbital overlap. Information relating to molecular stacking in the solid state was further confirmed by powder wide-angle X-ray scattering (WAXS) and out-of-plane X-ray diffraction (XRD) measurements. As indicated in **Figure 2-6**, I could assign the d_{100}-spacings (11.7 Å) and the π–π distance values (3.6 Å) based on the characteristic X-ray peaks.

The d_{100}-spacing value (11.9 Å) for the DPP-T-DCV crystal device was further confirmed by out-of-plane XRD analysis, which agreed well with the powder WAXS data (see **Figure 2-7**). The AFM results from single crystals and thermally deposited polycrystalline films (**Figure 2-3**, **Figure 2-7**) showed that the average step heights of the terrace structures were equivalent. These results indicated that the molecular stacking structures in the single crystal and polycrystalline film yielded identical d_{100}-spacing values. The molecular stacking information showed that DPP-T-DCV assumes

a well-defined lamellar structure and a highly dense packed molecular conformation in the solid state, providing efficient electron transport. Compared to reports of the dicyanomethylene-substituted DPP-based quinoidal molecules 1 and 2,[31] DPP-T-DCV presented certain differences that improved their prospects for use in solution-processed SC-OFET devices: (1) The solubility of DPP-T-DCV (~6 mg/mL) was slightly better than that of the quinoidal molecule 1 (<3 mg/mL), despite having identical alkyl chains in the structures. This may have been due to the presence of a single bonding component in the vinyl group of DPP-T-DCV; (2) In the film absorption spectra, the absorption of DPP-T-DCV was bathochromically shifted relative to 1 and 2 by about 40 nm, and a strong shoulder absorption appeared, characteristic of intermolecular π-π stacking; (3) DPP-T-DCV has higher melting temperature (T_m: 239℃) than 2 (T_m: 206℃), indicating that the thermal stability of DPP-T-DCV is high due to strong intermolecular stacking (see **Figure 2-8**); (4) Structure analysis indicated the *d*-spacing values for the DPP-T-DCV (11.7–11.9 Å), which were smaller than those of 1 (~16.2 Å) or 2 (~24.0 Å). This result provides direct evidence for the strong π-π stacking, which generally promotes crystal formation. In this regard, DPP-T-DCV showed obvious terraced structures in the crystalline state and a high μ_e.

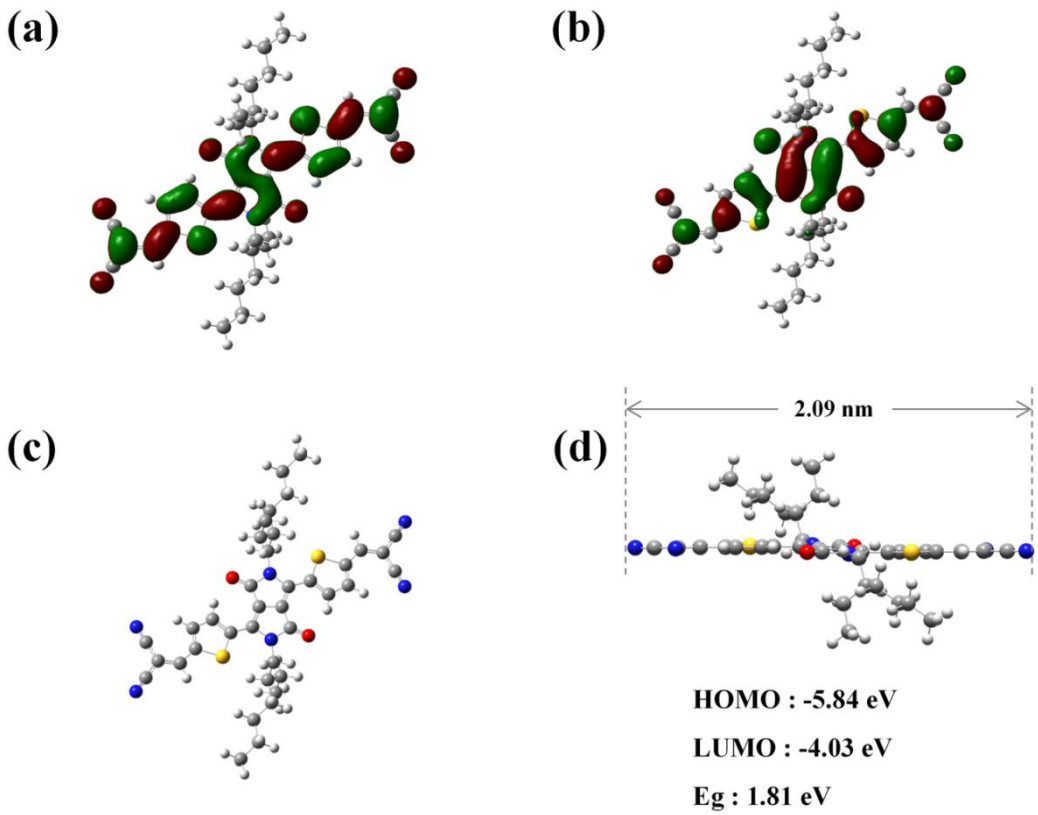

Figure 2-5. Electron distributions of the (a) HOMO and (b) LUMO. (c) Front and (d) side views of the optimized DPP-T-DCV geometries.

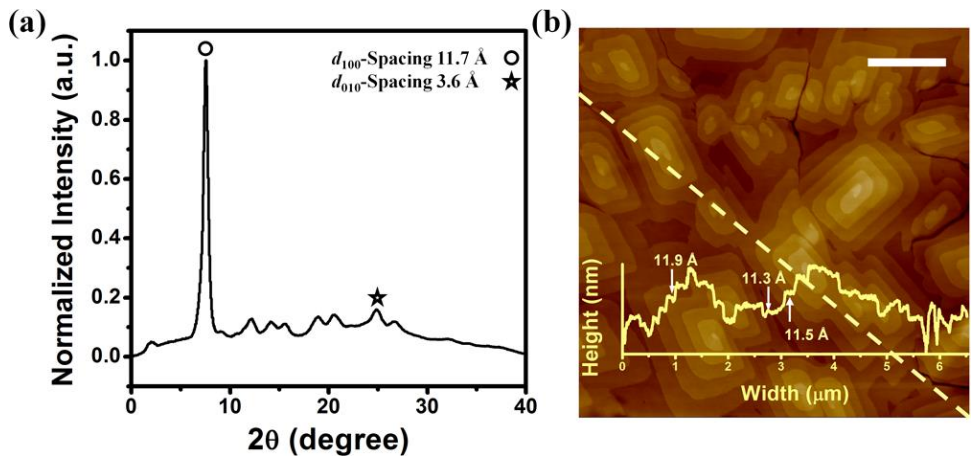

Figure 2-6. (a) Two-dimensional WAXS spectrum of the DPP-T-DCV powder. (b) AFM image of the film surface of the DPP-T-DCV vacuum-deposited film on an ODTS-treated SiO_2/Si substrate (scale bar: 1 μm, inset: thickness profile along the yellow dashed line).

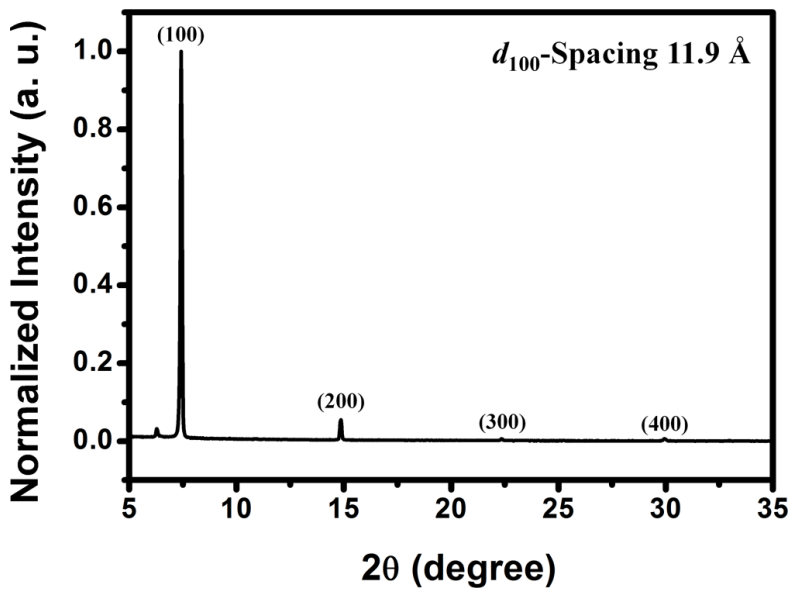

Figure 2-7. Out-of-plane XRD analysis of the DPP-T-DCV crystal.

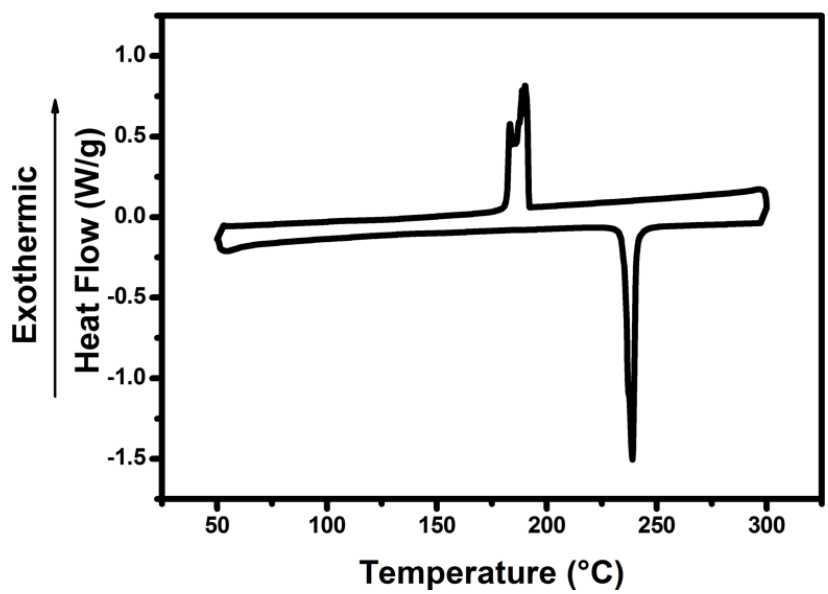

Figure 2-8. DSC trace of the DPP-T-DCV.

2.3. Experimental

Materials and Characterization: All commercially available reagents were purchased from Sigma Aldrich Chemical Co., Tokyo Chemical Industry Co., or Alfa Aesar Co., and were used without further purification. Detailed synthetic procedures are described in the Synthesis section. Chemical structures were identified by ^{1}H NMR (Bruker, Avance-300), ^{13}C NMR (Bruker, Avance-500), GC-Mass spectrometry (JEOL, JMS-700), and elemental analysis EA1110, CE Instrument). UV-Vis absorption spectra were recorded on a SHIMADZU UV-1650PC spectrometer. The HOMO energy levels were measured in films using a photoelectron spectrometer (Hitachi High Tech, AC-2). The LUMO level was calculated based on the HOMO level and the optical band gap, which was obtained from the edge of the absorption spectra. Powder wide-angle X-ray scattering (WAXS) measurements were conducted using a Bruker GADDS instrument. Out-of-plane X-ray diffraction (XRD) measurements were performed using a D8-Advance X-ray diffractometer (Bruker Miller Co., Germany). The operating conditions included a step size of 0.02, a scan rate of 3 degree/min, a 40 KV generator voltage, a 40 mA tube current, and room temperature (Cu std target λ = 1.5418 Å). Atomic force microscopy was performed using a Multimode with a NanoScope V controller, Bruker, in the tapping mode.

Device fabrication and Evaluation: Prior to device fabrication, SiO_2/Si (300 nm thick SiO_2) substrates were rinsed by sonication in acetone and isopropyl alcohol. The substrates were then exposed to UV light (360 nm) for 10 min. The fabrication of a simple solution-processable single crystalline field-effect transistor was carried out via the solvent evaporation crystal growth technique. A SiO_2/Si wafer was leaned against the inner wall of a 20 mL vial containing a 0.05 wt% DPP-T-DCV solution (in dichloromethane) under ambient conditions. DPP-T-DCV single crystal films grew spontaneously (directly and slowly) on the substrates, producing firm contact between the substrates and the crystal films. After crystal formation, the substrates were annealed at 50℃ for 1 hour to eliminate residual solvent. The 50 nm thick source–drain Au electrodes were thermally deposited directly onto the crystalline layers through a metal mask to fabricate top-contact SC-OFETs (the deposition rate was 0.1–0.2 Å s^{-1}). The thermal evaporation and vacuum deposition of polycrystalline FETs was achieved by introducing an octadecyltrichlorosilane (ODTS) layer to reduce charge trapping sites and to increase the domain size. ODTS was treated in the vapor phase in a vacuum oven, and the substrates were brought into a nitrogen-filled glove box. A series of 50 nm thick DPP-T-DCV active layers was thermally deposited with a deposition rate of 0.1–0.2 Å s^{-1} at different substrate temperatures (T_{SUB}) (RT, 70℃, 100℃, 120℃, and 140℃), under a vacuum of 7×10^{-7} Torr. The current–voltage characteristics of the OFETs were measured using a Keithley 4200 connected to a probe station. The electron field-effect mobility values of both SC-OFETs and

polycrystalline FETs in saturation region were calculated from the $\partial I_{D,sat}{}^{1/2} / \partial V_G$, where,

$$I_{D,sat} = \frac{W}{2L} C_{ox} \mu_{sat} (V_G - V_T)^2$$

W, *L* values were estimated by optical microscope and V_D = 100V.[37]

Synthesis of 3,6-di(thiophen-2-yl)pyrrolo[3,4-c]pyrrole-1,4(2H,5H)-dione (a): The precursor (a) was synthesized according to the procedure reported previously. To a solution of tert-amyl alcohol (120 mL) in a two-necked 500 mL round-bottom flask were slowly added sodium metal pieces (4.21 g, 183.23 mmol) under an Ar atmosphere. The mixture was heated to 120℃ and stirred for 3 h. 2-Thiophenecarbonitrile (10 g, 91.62 mmol) was added, followed by the dropwise addition of diethylsuccinate (6.38 g, 36.65 mmol) to the reaction mixture over 1 h. The mixture was stirred at 120℃ for 3 h, and then cooled to room temperature. The mixture were poured into acidic MeOH (200 mL MeOH and 10 mL HCl) in an ice bath and stirred for 1.5 h. The suspension was filtered, yielding a dark red solid, which was used in next step without further purification. Yield: 64.52% (17.76 g).

Synthesis of 2,5-bis(2-ethylhexyl)-3,6-di(thiophen-2-yl)pyrrolo[3,4-c]pyrrole-1,4(2H,5H)-dione (b): In a two-necked 500 mL round-bottom flask, compound (a) (7.5 g, 24.97 mmol), anhydrous potassium carbonate (11.39 g, 82.40 mmol), and catalytic amounts of 18-crown-6, were dissolved in anhydrous N,N-dimethylformamide (140

mL), and the solution was heated to 120℃ under an Ar atmosphere. 2-Ethylhexyl bromide (14.12 g, 73.11 mmol) was then added dropwise using a drop funnel. The reaction mixture was further stirred for 24 h at 120℃. After the reaction had gone to completion, the solution was cooled to room temperature, poured into water (400 mL), and the solid was collected by vacuum filtration. The filter cake was washed with water and methanol several times and then dried under vacuum. After drying in a vacuum, the crude product was purified by recrystallization in MeOH to obtain a dark red solid powder. Yield: 16.66% (2.18 g). ^{1}H NMR (300 MHz, $CDCl_3$, δ): 8.89 (dd, J = 3.9 Hz, J = 0.9 Hz, 2H), 7.63 (dd, J = 5.0 Hz, J = 0.9 Hz, 2H), 7.28 (d, J = 5.3 Hz, 2H), 4.05 (dd, J = 10.8 Hz, J = 3.6 Hz, 4H), 1.8–1.9 (m, 2H), 1.2–1.4 (m, 16H), 0.8–1.0 (m, 12H). ^{13}C NMR (500MHz, $CDCl_3$, δ): 161.8, 140.5, 135.2, 130.5, 130.0, 128.4, 108.0, 45.9, 39.1, 30.2, 28.4, 23.6, 23.0, 14.0, 10.5.

Synthesis of 5,5'-(2,5-bis(2-ethylhexyl)-3,6-dioxo-2,3,5,6-tetrahydropyrrolo[3,4-c]pyrrole-1,4-diyl)dithiophene-2-carbaldehyde (c): In a two-necked 500mL round-bottom flask, compound (b) (2.5 g, 4.77 mmol) was dissolved in anhydrous THF (90 mL). At –78 ℃, LDA (2 M, 9.5 mL) was added slowly dropwise under an Ar atmosphere. After 2 h stirring at this temperature, DMF (0.935 mL) was rapidly added to the solution. The resulting mixture was warmed slowly to room temperature. To the solution was added dichloromethane (30 mL), and the organic phase was washed with brine three times and dried over anhydrous $MgSO_4$. The residual solvent in the crude

product was evaporated by rotary evaporation, and the crude product was purified by column chromatography (MC/n-hexane/EA, 5:2:3 v/v/v) to give a purple-black solid powder. Yield: 27.83% (0.77g). ^{1}H NMR (300 MHz, $CDCl_3$, δ): 10.03 (s, 2H), 9.04 (d, J = 4.1 Hz, 2H), 7.88 (d, J = 1.7 Hz, 2H), 4.07 (m, 4H), 1.8–1.9 (m, 2H), 1.2–1.4 (m, 16H), 0.8–1.0 (m, 12H). ^{13}C NMR (500MHz, $CDCl_3$, δ): 182.77, 161.37, 146.52, 140.57, 136.70, 136.10, 136.00, 110.86, 46.15, 39.26, 30.10, 28.24, 23.49, 22.99, 13.97, 10.40.

Synthesis of 2,2'-(5,5'-(2,5-bis(2-ethylhexyl)-3,6-dioxo-2,3,5,6-tetrahydropyrrolo[3,4-c]pyrrole-1,4-diyl)bis(thiophene-5,2-diyl))bis(methan-1-yl-1-ylidene)dimalononitrile (DPP-T-DCV): In a two necked 250 mL round bottom flask, compound (c) (0.77 g, 1.33 mmol), malononitrile (0.26 g, 3.98 mmol), and aluminum oxide (0.77 g, 9.3 mmol) were dissolved in dichloromethane (60 mL), and stirred for 1 h at room temperature. After the reaction had gone to completion, the mixture was filtered, and residual solvent was evaporated by rotary evaporation. The crude product was purified by reprecipitation in MeOH. MC gave a dark blue solid powder. Yield: 61.29% (0.55g). ^{1}H NMR (300 MHz, $CDCl_3$, δ): 9.20 (d, J = 4.3 Hz, 2H), 7.89 (s, 2H), 7.84 (d, J = 4.4 Hz, 2H), 4.10 (dd, J = 8.2 Hz, J = 2.3 Hz, 4H), 1.8–1.9 (m, 2H), 1.2–1.4 (m, 16H), 0.8–1.0 (m, 12H). HRMS (ESI, *m/z*): $[M + H]^+$ calcd for $C_{38}H_{41}N_6O_2S_2$, 677.27; found 677.27. Anal. calcd for $C_{38}H_{40}N_6O_2S_2$: C 67.43, H 5.96, N 12.42, O 4.73, S 9.47; found: C 67.48, H 5.96, N 12.35, O 4.73, S 9.50.

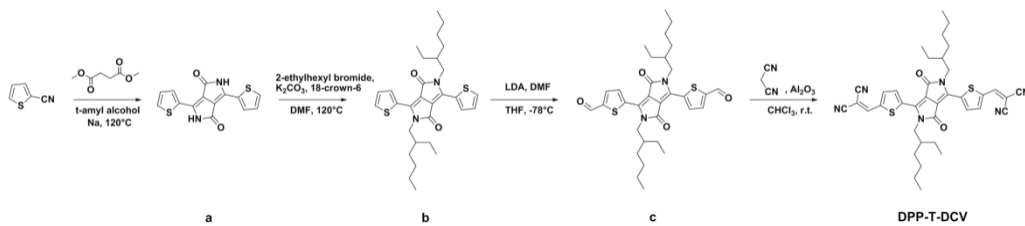

Scheme 2-1. Synthesis of DPP-T-DCV.

2.4. Conclusion

In conclusion, I successfully synthesized and characterized a dicyanovinyl-substituted DPP-based small molecule, DPP-T-DCV, for use in high-performance n-type SC-OFET applications. The LUMO level was lowered due to the inherent electron deficiencies of the DPP and dicyanovinyl groups. In combination with the dense molecular packing among the planar structures, DPP-T-DCV was found to display excellent potential for use in n-type solution-processed SC-OFET applications. DPP-T-DCV exhibited high-crystalline behavior with good solubility and an outstanding μ_e of up to 0.96 $cm^2 V^{-1} s^{-1}$ in SC-OFETs.

2.5. Reference

[1] V. Podzorov, V. M. Pudalov, M. E. Gershenson, *Appl. Phys. Lett.* **2003**, *82*, 1739.

[2] H. Ebata, T. Izawa, E. Miyazaki, K. Takimiya, M. Ikeda, H. Kuwabara, and T. Yui, *J. Am. Chem. Soc.* **2007**, *129*, 15732.

[3] M. Jin Kang, I. Doi, H. Mori, E. Miyazaki, K. Takimiya,, M. Ikeda, H. Kuwabara, *Adv. Mater.* **2011**, *23*, 1222.

[4] S. W. Yun, J. H. Kim, S. Shin, H. Yang, B.-K. An, L. Yang, S. Y. Park, *Adv. Mater.* **2012**, *24*, 911.

[5] A. R. Brown, D. M. de Leeuw, E. J. Lous, E. E. Havinga, *Synth. Met.* **1994**, *66*, 257.

[6] A. Facchetti, M.-H. Yoon, T. J. Marks, *Adv. Mater.* **2005**, *17*, 1705.

[7] T. D. Anthopoulos, G. C. Anyfantis, G. C. Papavassiliou, D. M. de Leeuw, *Appl. Phys. Lett.* **2007**, *90*, 122105.

[8] J. Soeda, T. Uemura, Y. Mizuno, A. Nakao, Y. Nakazawa, A. Facchetti, J. Takeya, *Adv. Mater.* **2011**, *23*, 3681.

[9] L. Jiang, H. Dong, Q. Meng, H. Li, M. He, Z. Wei, Y. He, W. Hu, *Adv. Mater.* **2011**, *23*, 2059.

[10] A. B. Tamayo, B. Walker, T.-Q. Nguyen, *J. Phys. Chem. C* **2008**, *112*, 11545.

[11] J. Mizuguchi, A. Grubenmann, G. Wooden, G. Rihs, *Acta Cryst.* **1992**, *B48*, 696.

[12] J. Mizuguchi, *J. Phys. Chem. A.* **2000**, *104*, 1817.

[13] S. Qu, H. Tian, *Chem. Commun.* **2012**, *48*, 3039.

[14] H. Chen, Y. Guo, G. Yu, Y. Zhao, J. Zhang, D. Gao, H. Liu, Y. Liu, *Adv. Mater.* **2012**, *24*, 4618.

[15] C. Kanimozhi, N. Yaacobi-Gross, K. W. Chou, A. Amassian, T. D. Anthopoulos, S. Patil, *J. Am. Chem. Soc.* **2012**, *134*, 16532.

[16] J.-R Pouliot, L. G. Mercier, S. Caron, M. Leclerc, *Macromol. Chem. Phys.* **2012**, *214*, 453.

[17] S.-L. Suraru, U. Zschieschang, H. Klauk, F. Würthner, *Chem. Commun.* **2011**, *47*, 1767.

[18] H. Bronstein, Z. Chen, R. S. Ashraf, W. Zhang, J. Du, J. R. Durrant, P. Shakya Tuladhar, K. Song, S. E. Watkins, Y. Geerts, M. M. Wienk, R. A. J. Janssen, T. Anthopoulos, H. Sirringhaus, M. Heeney, I. McCulloch, *J. Am. Chem. Soc.* **2011**, *133*, 3272.

[19] Y. Li, P. Sonar, S. P. Singh, M. S. Soh, M. van Meurs, J. Tan, *J. Am. Chem. Soc.* **2011**, *133*, 2198.

[20] T. L. Nelson, T. M. Young, J. Liu, S. P. Mishra, J. A. Belot, C. L. Ballet, A. E. Javier, T. Kowalewski, R. D. McCullough, *Adv. Mater.* **2010**, *22*, 4617.

[21] J. S. Ha, K. H. Kim, D. H. Choi, *J. Am. Chem. Soc.* **2011**, *133*, 10364.

[22] T.-J. Ha, P. Sonar, A. Dodabalapur, *Appl. Phys. Lett.* **2011**, *98*, 255305.

[23] Y. Li, P. Sonar, S. P. Singh, W. Zeng, M. S. Soh, *J. Mater. Chem.* **2011**, *21*, 10829.

[24] D. Cortizo-Lacalle, S. Arumugam, S. E. T. Elmasly, A. L. Kanibolotsky, N. J. Findlay, A. R. Inigo, P. J. Skabara, *J. Mater. Chem.* **2012**, *22*, 11310.

[25] J. B. Lee, K. H. Kim, C. S. Hong, D. H. Choi, *J. Polym. Sci., Part A: Polym. Chem.* **2012**, *50*, 2809.

[26] J. W. Jung, F. Liu, T. P. Russell, W. H. Jo, *Energy Environ. Sci.* **2012**, *5*, 6857.

[27] M. Tantiwiwat, A. Tamayo, N. Luu, X.-D. Dang, T.-Q. Nguyen, *J. Phys. Chem. C* **2008**, *112*, 17402.

[28] J. Mei, K. R. Graham, R. Stalder, S. P. Tiwari, H. Cheun, J. Shim, M. Yoshio, C. Nuckolls, B. Kippelen, R. K. Castellano, J. R. Reynolds, *Chem. Mater.* **2011**, *23*, 2285.

[29] J. Casado, R. P. Ortiz, J. T. Lopez Navarrete, *Chem. Soc. Rev.* **2012**, *41*, 5672.

[30] Q. Wu, R. Li, W. Hong, H. Li, X. Gao, D. Zhu, *Chem. Mater.* **2011**, *23*, 3138.

[31] Y. Qiao, Y. Guo, C. Yu, F. Zhang, W. Xu, Y. Liu, D. Zhu, *J. Am. Chem. Soc.* **2012**, *134*, 4084.

[32] H. Zhong, J. Smith, S. Rossbauer, A. J. White, T. D. Anthopoulos, M. Heeney, *Adv. Mater.* **2012**. *24*, 3205.

[33] R. Fitzner, E. Reinold, A. Mishra, E. Mena-Osteritz, H. Ziehlke, C. Körner, K. Leo, M. Riede, M. Weil, O. Tsaryova, A. Weiß, C. Uhrich, M. Pfeiffer, P. Bäuerle, *Adv.*

Funct. Mater. **2011**, *21*, 897.

[34] T. Qi, Y. Liu, W. Qiu, H. Zhang, X. Gao, Y. Liu, K. Lu, C. Du, G. Yu, D. Zhu, *J. Mater. Chem.* **2008**, *18*, 1131.

[35] M. J. Frisch, G. W. Trucks, H. B. Schlegel, G. E. Scuseria, M. A. Robb, J. R. Cheeseman, J. A. Montgomery Jr., T. Vreven, K. N. Kudin, J. C. Burant, J. M. Millam, S. S. Iyengar, J. Tomasi, V. Barone, B. Mennucci, M. Cossi, G. Scalmani, N. Rega, G. A. Petersson, H. Nakatsuji, M. Hada, M. Ehara, K. Toyota, R. Fukuda, J. Hasegawa, M. Ishida, T. Nakajima, Y. Honda, O. Kitao, H. Nakai, M. Klene, X. Li, J. E. Knox, H. P. Hratchian, J. B. Cross, V. Bakken, C. Adamo, J. Jaramillo, R. Gomperts, R. E. Stratmann,O. Yazyev, A. J. Austin, R. Cammi, C. Pomelli, J. W. Ochterski, P. Y. Ayala, K. Morokuma, G. A. Voth, P. Salvador, J. J. Dannenberg, V. G. Zakrzewski, S. Dapprich, A. D. Daniels, M. C. Strain, O. Farkas, D. K. Malick, A. D. Rabuck, K. Raghavachari, J. B. Foresman, J. V. Ortiz, Q. Cui, A. G. Baboul, S. Clifford, J. Cioslowski, B. B. Stefanov, G. Liu, A. Liashenko, P. Piskorz, I. Komaromi, R. L. Martin, D. J. Fox, T. Keith, M. A. Al-Laham, C. Y. Peng, A. Nanayakkara, M. Challacombe, P. M. W. Gill, B. Johnson, W. Chen, M. W. Wong, C. Gonzalez, J. A. Pople, *Gaussian 09, Revision A.02, Gaussian, INC., Wallingford, CT,* **2009**.

[36] S. K. Park, J. H. Kim, S.-J. Yoon, O. K. Kwon, B.-K. An, S. Y. Park, *Chem. Mater.* **2012**, *24*, 3263.

[37] C. R. Newman, C. D. Frisbie, D. A. da Silva Filho, J.-L. Brédas, P. C. Ewbank, K. R. Mann, *Chem. Mater.* **2004**, *16*, 4436.

Chapter 3. A Novel Bis-Lactam Acceptor with Outstanding Molar Extinction Coefficient and Structural Planarity for Donor-Acceptor Type Conjugated Polymer

3.1. Introduction

Over the past few decades, π-conjugated polymer semiconductors have drawn great attention for use in solution-processed organic photovoltaic devices owing to their applicability in flexible, large-area devices.[1-5] Recently, bulk heterojunction (BHJ)-type polymer solar cells (PSCs) with a power conversion efficiency (PCE) greater than 10% have been reported.[6-12] Although a PCE of this level for PSCs is quite impressive, further improvements in the conversion efficiency are necessary for these devices to find practical use. To this end, great efforts are being devoted not only to optimizing the device architecture[13,14] but also to developing high-performance materials.[15-17]

Donor-acceptor (D-A) type conjugated polymers, involving intramolecular charge transfer via an alternative combination of D and A building blocks along the π-conjugated backbone, are being investigated intensively for use in PSCs, since these materials allow for the facile control of the electronic characteristics based on the rational choice of the D and A units.[18-25] A large number of studies have revealed that

the photovoltaic properties of D-A conjugated polymers are closely associated with the characteristics of both the D and the A moieties in the polymer backbone: [26,27] (a) the quasi-planar conjugated backbones of these polymers, which contain the D and A units, enhance the charge-carrier mobility owing to the strong π-stacking interactions[28] and (b) the light absorptivity of these polymers scales with the oscillator strength of the conjugated backbone, which, in turn, is modulated by the transition dipole moments of the D and A units.[29] To this end, numerous studies have reported the synthesis as well as the optoelectrical properties of conjugated polymers comprising different D and A building blocks and also the characteristics of devices based on these polymers.[30-37] However, while many D building blocks have been studied, only a few A building blocks have been reported so far. These include benzothiadiazole,[38-40] quinoxaline,[41-43] thieno[3,4-c]pyrrole-4,6-dione,[44,45] and lactam moieties.[46-51] Therefore, it is imperative that more A building blocks should be developed through the proper design strategy for high-performance D-A type conjugated polymers.

In this context, planar bis-lactam-based materials, such as thiophenyl substituted diketopyrrolopyrrole (DPPT),[52-54] isoindigo (II),[55,56] and isoDPPT[57,58] (**Figure 3-1**) have attracted much attention lately as desirable electron-accepting building blocks because of their unique features, which include (a) a high electron affinity because of the electron-withdrawing effect of the lactam units, (b) high degree of π-π stacking, which is driven by their quasi-planar backbone structure, and (c) the possibility of controlling their solubility by incorporating suitable alkyl and aryl side chains in the

lactam *N*-atom position.[59]

Inspired by such beneficial effects of bis-lactam compounds, I attempted to develop a high-performance bis-lactam compound of 3,7-dithiophen-2-yl-1,5-dialkyl-1,5-naphthyridine-2,6-dione (NTDT) (**Figure 3-1**) in this work. NTDT is structurally based on 1,5-dihydro-1,5-naphthyridine-2,6-dione, which was first synthesized by Rapoport in 1971[60] and barely used as monomer of conjugated polymer.[61,62] While both NTDT and DPPT are expected to be electron deficient, based on the bis-lactam unit, their electronic and photophysical properties are probably different, owing to the difference in the ring sizes of their lactam units. Interestingly, density functional theory (DFT) calculations and single-crystal analyses have revealed that the optimized geometry of NTDT corresponds to a coplanar conformation. It is worth noting that, through time-dependent DFT (TD-DFT) calculations, I found that NTDT has a higher oscillator strength (f value) than that of DPPT, which is known to be a compound with a high molar absorption coefficient. In addition, NTDT allows for alkylation through the introduction of various solubilizing side groups at the lactam *N*-position. This could allow for the realization of simple solubility control without having to use any solubilizing comonomers.

Given these advantages of NTDT, I designed and synthesized a new D-A type conjugated copolymer P(NTDT-BDT) with NTDT as a novel bis-lactam-based A building block and the representative D unit of benzo[1,2-*b*:4,5-*b*']dithiophene (BDT) as the first example of an NTDT-incorporating polymer semiconductor. P(DPPT-

BDT)[63-65] was also synthesized as a reference sample for P(NTDT-BDT), since the DPPT unit has extensively been used as the most efficient bis-lactam unit in the D-A type conjugated polymer. Furthermore, the electronic, thermal, photophysical, electrochemical, structural, and photovoltaic properties of P(NTDT-BDT) were studied in depth, in order to demonstrate the high potential of NTDT for use in organic optoelectronics.

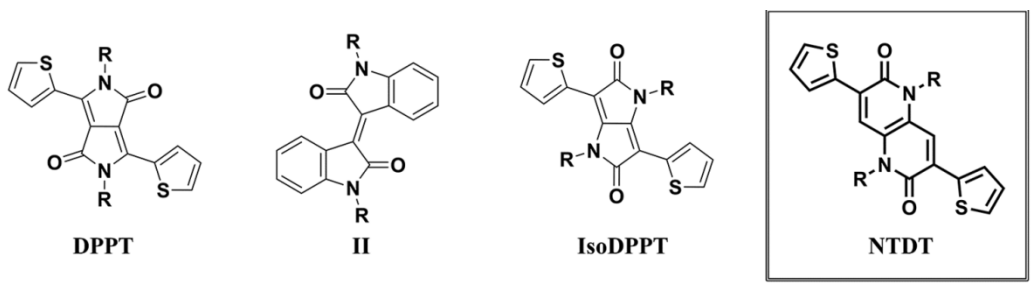

Figure 3-1. Molecular structures of widely used bis-lactam acceptors and NTDT.

3.2. Results and Discussion

3.2.1 Synthesis and characterization

The route for synthesizing the thienyl-substituted NTD monomer (NTDT) is depicted in **Scheme 3-1**. 6-methoxy-1,5-naphthyridin-2(1H)-one (2) was synthesized as reported.[66] The subsequent O-demethylation of 2 with hydrogen bromide yielded the 1,5-dihydro-1,5-naphthyridine-2,6-dione compound 3, which was then *N*-alkylated with 1-bromooctane in the presence of cesium carbonate to obtain 1,5-dioctyl-1,5-naphthyridine-2,6-dione (4, NTD). This compound was brominated with bromine to obtain 3,7-dibromo-1,5-dioctyl-1,5-naphthyridine-2,6-dione (5), which was then reacted with tributyl(thiophen-2-yl)stannane under typical Stille coupling reaction conditions; this yielded the NTDT monomer 6. The copolymers containing the NTDT and DPPT building blocks, namely, P(NTDT-BDT) and P(DPPT-BDT), were prepared through Stille-coupling polymerization using BDT as an electron-rich counterpart. The number average molecular weight (M_n) and polydispersity index (PDI) values of P(NTDT-BDT) and P(DPPT-BDT) were determined by gel permeation chromatography (GPC). The results revealed that both polymers had a high molecular weight (M_n = 60.7 KDa, PDI = 3.15 for P(NTDT-BDT) and M_n = 59.3 KDa, PDI = 2.84 for P(DPPT-BDT)). Thermal gravimetric analysis (TGA) measurements were

performed to investigate the thermal stabilities of the monomers (NTDT and DPPT) and polymers (P(NTDT-BDT) and P(DPPT-BDT)). As shown in **Figure 3-2**, the NTDT-based materials (NTDT thermally stable up to 350°C and P(NTDT-BDT)) up to 358°C) exhibited higher thermal stabilities than the DPPT-based materials (DPPT thermally stable up to 316°C and P(DPPT-BDT) up to 343°C).

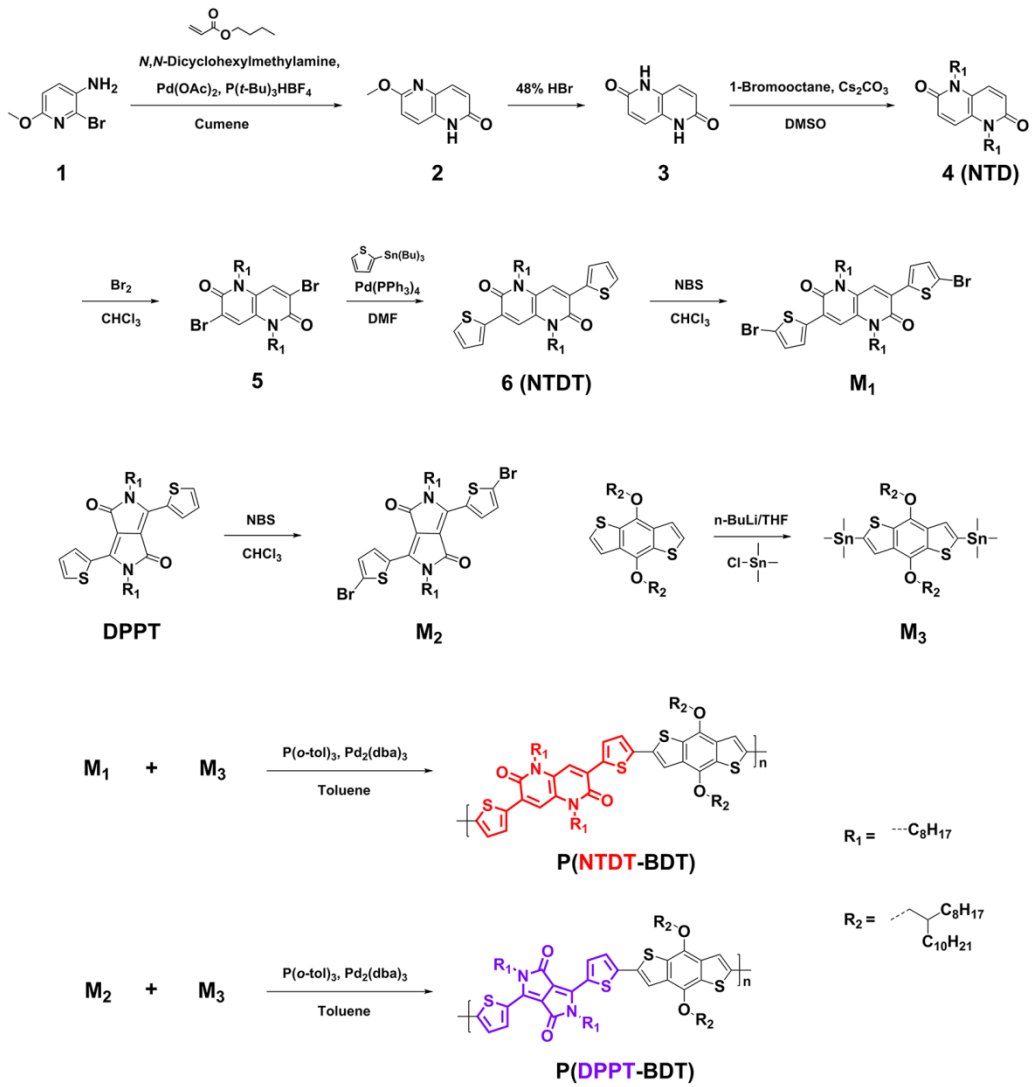

Scheme 3-1. Synthesis of P(NTDT-BDT) and P(DPPT-BDT).

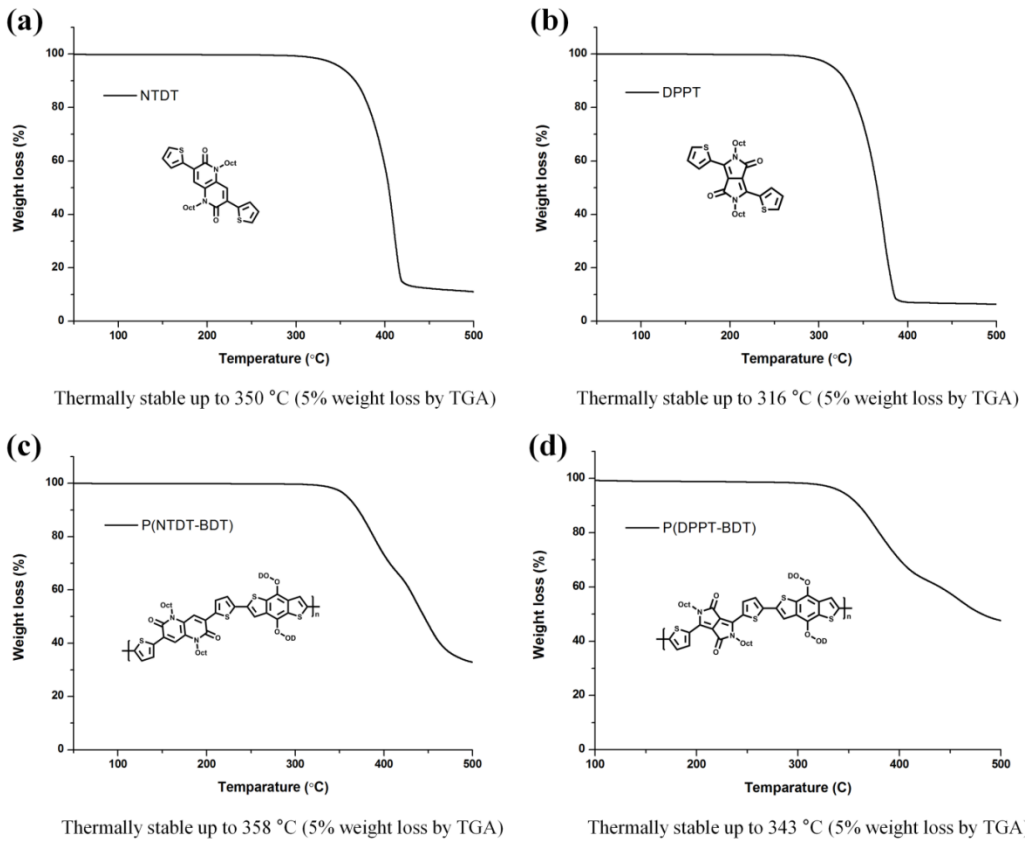

Figure 3-2. TGA curves of (a) NTDT, (b) DPPT, (c) P(NTDT-BDT), and (d) P(DPPT-BDT).

3.2.2. Theoretical calculations

The molecular structures and optimized geometries of the electron-deficient building blocks (NTDT and DPPT (R = Me)) were analyzed through theoretical quantum chemical calculations, which were performed using Gaussian 09 at the B3LYP level with the basis set of 6-31G**, as shown in **Figure 3-3**a and **3-3**b, respectively. As expected, both NTDT and DPPT exhibited a higher degree of planarity with a small thiophene-core dihedral angle (<1°), which facilitated charge-carrier transport via strong π-π stacking interactions.[67] The calculated highest occupied molecular orbital (HOMO)/lowest unoccupied molecular orbital (LUMO) values for the two building blocks were found to be -5.15/-2.56 eV (for NTDT) and -4.97/-2.52 eV (for DPPT) (**Table 3-1**). Furthermore, to be able to predict the optimized geometries of P(NTDT-BDT) and P(DPPT-BDT), I performed calculations on double-repeat units ((NTDT-$BDT)_2$ and $(DPPT\text{-}BDT)_2$) of the two polymers with methyl-substituted alkyl chains (**Figure 3-3**c and **3-3**d). The computational results confirmed that they also had highly planar geometries, with the NTDT-based molecules having deeper HOMO levels than those of the DPPT-based molecules.

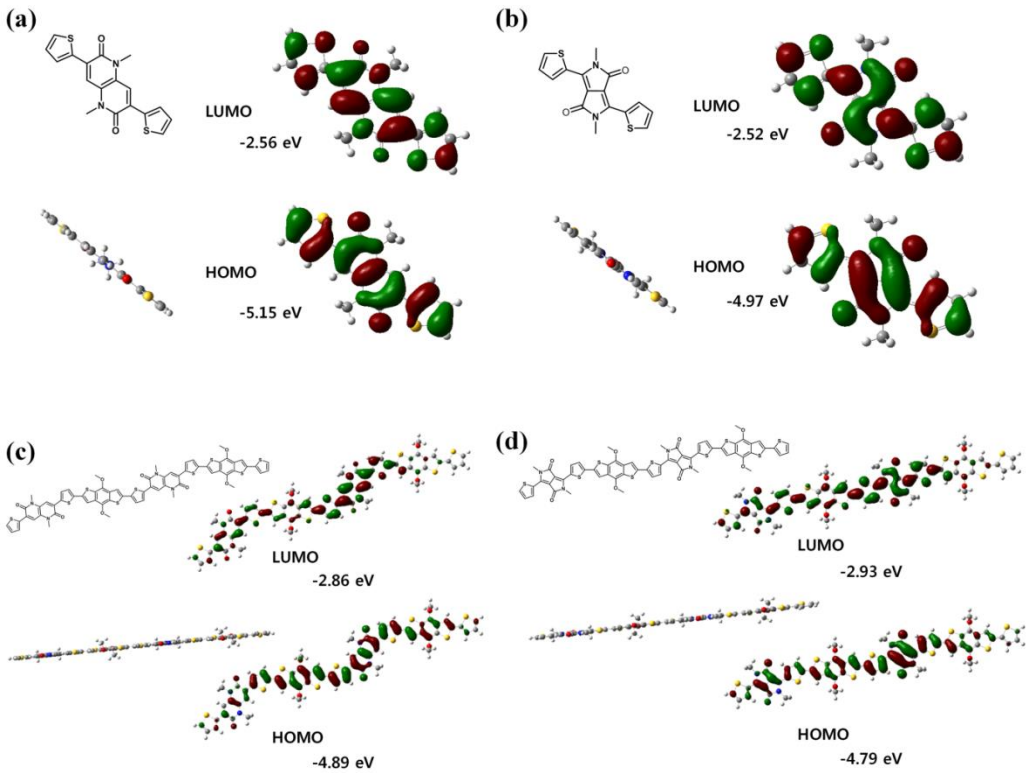

Figure 3-3. Molecular structures, side views of optimized geometries, and electron distributions of the HOMO and LUMO levels of the model compound for (a) NTDT, (b) DPPT, (c) P(NTDT-BDT), and (d) P(DPPT-BDT), as determined using DFT calculations performed using the Gaussian 09 software.

Table 3-1. Characteristics of NTDT, DPPT, P(NTDT-BDT), and P(DPPT-BDT).

	M_n [a)] [kDa]	PDI[a)]	T_d [b)] [°C]	$\lambda_{max,sol}$ [c)] / λ_{film} [d)] [nm]	ε at $\lambda_{max} \times 10^4$ [e)] [$M^{-1}cm^{-1}$]	ε at $\lambda_{max} \times 10^4$ [f)] [cm^{-1}]	E_g^{opt} [g)] [eV]
NTDT	-	-	350	497/533	5.10	-	2.29
DPPT	-	-	316	549/601	3.14	-	1.96
P(NTDT-BDT)	60.7	3.15	358	651/667	-	31.7	1.66
P(DPPT-BDT)	59.3	2.84	343	748/754	-	15.7	1.32

[a)]Determined by GPC using polystyrene standards in $CHCl_3$; [b)]5% weight-loss temperature measured by TGA under nitrogen flow; [c)]Measured in $CHCl_3$ solution (5×10^{-5} M); [d)]Thin film was spin-coated from $CHCl_3$ solution onto a quartz substrate; [e)]Measured from solution absorption spectra at λ_{max}; [f)]Measured from solution absorption spectra at λ_{max}; [g)]Determined from the onset of UV-vis absorption spectra.

3.2.3. Single crystal analysis

To gain a deeper insight into the conformations of these core units, single-crystal X-ray diffraction analyses were conducted. Single crystals of NTDT and DPPT were prepared by the solvent diffusion crystal growth method using a dichloromethane/methanol (7:3 v/v for NTDT and 8:2 v/v for DPPT) solution. As shown in **Figure 3-4**, the single-crystal XRD structure of both NTDT (**Figure 3-4**a) and DPPT (**Figure 3-4**b) belongs to the monoclinic crystal system (see the **Table 3-2** and **Table 3-3** for the crystallographic data). It can be seen clearly that, in DPPT, intramolecular hydrogen-bonded (O···H) interactions occur with the bond distance being 2.28 Å. In contrast, in NTDT, S···O interactions occur between the sulphur of the thiophene molecule and the oxygen of the carbonyl group, with the bond distance being 2.69 Å. These results indicated that the energetically preferable conformations of the two units are determined by different nonbonding interactions, which, in turn, are influenced by the steric factor, inter- and intramolecular interactions, and the degree of π-conjugation.[68] Interestingly, the single crystal of NTDT showed a quasi-planar structure, with the torsional angle (1.38°) between thiophene and the mean plane of the NTDT core being much smaller than that in the case of DPPT (10.93°). In addition, the intermolecular *π-π* distance in the NTDT crystal (3.40 Å) is slightly smaller than that in DPPT (3.42 Å), indicating that the π-π interaction in the NTDT is as strong as DPPT,

owing to the rigid molecular structure.

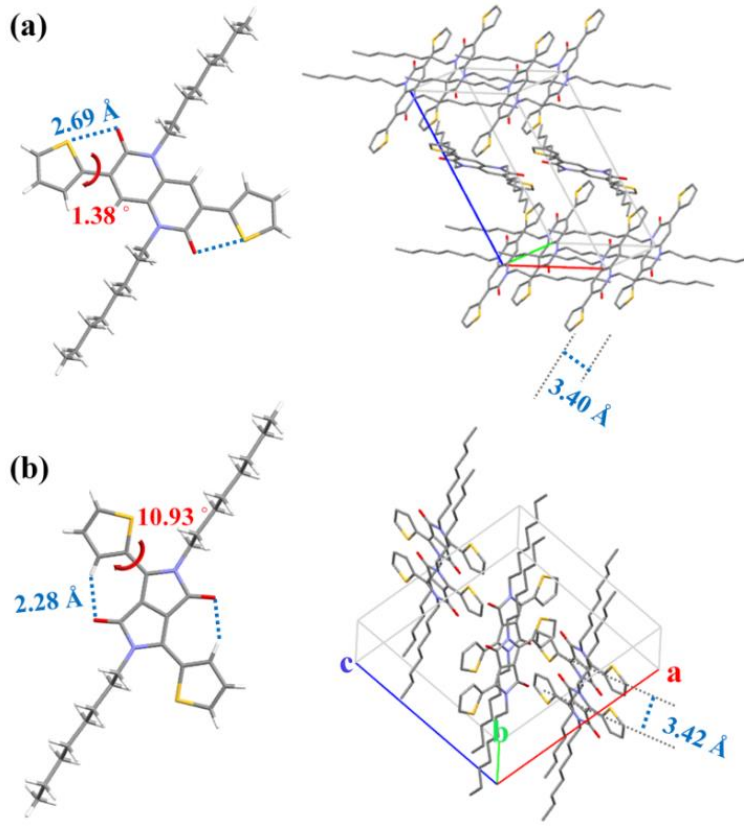

Figure 3-4. Crystal structures and molecular stacking structures of (a) NTDT and (b) DPPT.

Table 3-2. Crystallographic data of NTDT single crystal.

Empirical formula	C32 H42 N2 O2 S2
Formula weight	550.79
Temperature	173(2) K
Wavelength	0.71073 Å
Crystal system	Monoclinic
Space group	P 21/c
Unit cell dimensions	a = 16.0039(3) Å α = 90°
	b = 5.6678(10) Å β = 111.918(10)°
	c = 17.5189(3) Å γ = 90°
Volume	1474.22(5) $Å^3$
Z	2
Density (calculated)	1.241 Mg/m^3
Absorption coefficient	0.212 mm^{-1}
F(000)	592
Crystal size	0.750 x 0.140 x 0.100 mm^3
Theta range for data collection	1.372 to 28.246°.
Index ranges	-21<=h<=21, -7<=k<=7, -22<=l<=23
Reflections collected	13647
Independent reflections	3647 [R(int) = 0.0256]
Completeness to theta = 25.242°	99.9 %
Absorption correction	Semi-empirical from equivalents
Max. and min. transmission	0.7457 and 0.6622
Refinement method	Full-matrix least-squares on F^2
Data / restraints / parameters	3647 / 0 / 172
Goodness-of-fit on F^2	1.037
Final R indices [I>2sigma(I)]	R1 = 0.0411, wR2 = 0.1121
R indices (all data)	R1 = 0.0504, wR2 = 0.1211
Extinction coefficient	n/a

Table 3-3. Crystallographic data of DPPT single crystal.

Empirical formula	C30 H40 N2 O2 S2
Formula weight	524.76
Temperature	173(2) K
Wavelength	0.71073 Å
Crystal system	Monoclinic
Space group	P 21/c
Unit cell dimensions	a = 16.7285(5) Å α = 90°
	b = 5.2556(2) Å β = 90.651(2)°
	c = 15.6848(5) Å γ = 90°
Volume	1378.89(8) $Å^3$
Z	2
Density (calculated)	1.264 Mg/m^3
Absorption coefficient	0.223 mm^{-1}
F(000)	564
Crystal size	0.620 x 0.130 x 0.030 mm^3
Theta range for data collection	2.435 to 28.381°.
Index ranges	-18<=h<=22, -6<=k<=6, -20<=l<=20
Reflections collected	12472
Independent reflections	3396 [R(int) = 0.0370]
Completeness to theta = 25.242°	99.8 %
Absorption correction	Semi-empirical from equivalents
Max. and min. transmission	0.7457 and 0.6655
Refinement method	Full-matrix least-squares on F^2
Data / restraints / parameters	3396 / 0 / 163
Goodness-of-fit on F^2	1.024
Final R indices [I>2sigma(I)]	R1 = 0.0431, wR2 = 0.0929
R indices (all data)	R1 = 0.0712, wR2 = 0.1060
Extinction coefficient	n/a

3.2.4. Optical and electrochemical properties

The photophysical properties of the bis-lactam monomers (NTDT and DPPT) as well as the polymers (P(NTDT-BDT) and P(DPPT-BDT)) were examined by UV-vis absorption spectroscopy both in the solution state (1.0×10^{-5} M, $CHCl_3$) and in the film state (using spin-cast films formed on quartz substrates). NTDT exhibited the maximum absorption (λ_{max}^{abs}) at 497 nm in solution (533 nm in film form) whereas that of DPPT was observed at 549 nm (601 nm in film form) (**Figure 3-5** and **Table 3-1**), indicating that NTDT exhibits a relatively weaker intramolecular charge transfer (ICT) transition between the NTD unit and the flanked thiophene unit than that seen in DPPT. However, NTDT showed a markedly larger molar extinction coefficient (51,000 M^{-1} cm^{-1}) at the λ_{max}^{abs} level in solution form than that of DPPT, which was 31,400 M^{-1} cm^{-1} (**Figure 3-5**b). To elucidate the reason for these differences in the absorption characteristics, TD-DFT calculations were performed for NTDT and DPPT. As shown in **Figure 3-6**, the S_0–S_1 transition energy spectra of the two units matched well with the corresponding experimental results. Furthermore, the computed oscillator strength indicated that the f value of NTDT (= 0.9064) was much larger than that of DPPT (= 0.4773); this was consistent with the trend observed in the experimentally determined molar extinction coefficients. **Figure 3-5**c and **Figure 3-5**d show the UV-vis absorption spectra of P(NTDT-BDT) and P(DPPT-BDT); As for the solid-state film,

the absorption spectra of both polymers are broadly spanned and extended to the longer wavelength region compared to the solution-state absorption region. However, both polymers showed different degrees of bathochromically shifted maximum absorption ($\Delta \lambda_{max}^{abs}$) in the solid states from those in solution (16 nm for P(NTDT-BDT) and 6 nm for P(DPPT-BDT) (**Table 3-1**)). Compared to P(DPPT-BDT), P(NTDT-BDT) showed a larger solution-to-thin film peak shift, indicating that the intermolecular π–π stacking of P(NTDT-BDT) is more efficient than that of P(DPPT-BDT) in the solid state. Most significantly, P(NTDT-BDT) exhibits absorption maximum in the shorter-wavelength but with much higher absorption coefficient when compared with P(DPPT-BDT) (317,000 cm^{-1} for P(NTDT-BDT) and 157,000 cm^{-1} for P(DPPT-BDT)) in the film state). It should be noted that this value of the absorption coefficient is one of the highest reported for D-A type copolymers and would ensure that the material is suitable for harvesting photons and increasing the short-circuit current (J_{sc}) in photovoltaic devices.

To estimate the frontier MO energies of the core units and polymers, cyclic voltammetry (CV) analyses were performed on the solutions (CH_2Cl_2/0.1 M Bu_4NBF_4) and solid-state films (spin-coated on indium tin oxide (ITO) substrates) of the compounds (**Figure 3-7**). From the CV analyses, the HOMO energy levels of NTDT, DPPT, P(NTDT-BDT), and P(DPPT-BDT) were determined to be -5.42, -5.22, -5.33, and -5.23 eV, respectively. In addition, the LUMO energy levels of these molecules were evaluated from their HOMO levels and optical band gaps (E_g^{opt} of NTDT: 2.29 eV,

E_g^{opt} of DPPT: 1.96 eV, E_g^{opt} of P(NTDT-BDT): 1.66 eV, E_g^{opt} of P(DPPT-BDT): 1.32 eV), as depicted in **Figure 3-5**e and **3-5**f. The experimental HOMO/LUMO values of these molecules were in good agreement with the calculated ones. Specifically, the NTDT monomer and its polymer were found to exhibit relatively deeper HOMO levels than those of the corresponding DPPT derivatives. This should make the former suitable for increasing the open-circuit voltage (V_{oc}) of PSCs.

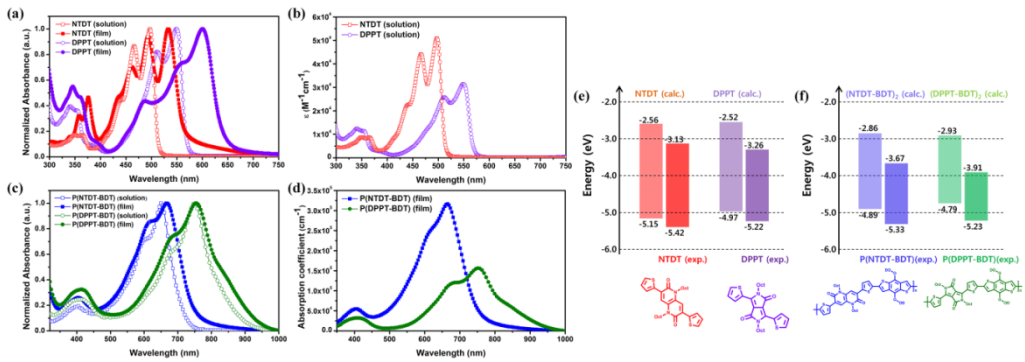

Figure 3-5. UV-vis absorption spectra of (a-b) NTDT and DPPT and (c-d) P(NTDT-BDT) and P(DPPT-BDT) in $CHCl_3$ solution and thin-film form on glass substrates. Energy level diagrams of (e) NTDT and DPPT and (f) P(NTDT-BDT) and P(DPPT-BDT). Light bars denote data obtained from DFT calculations while dark bars represent experimental data.

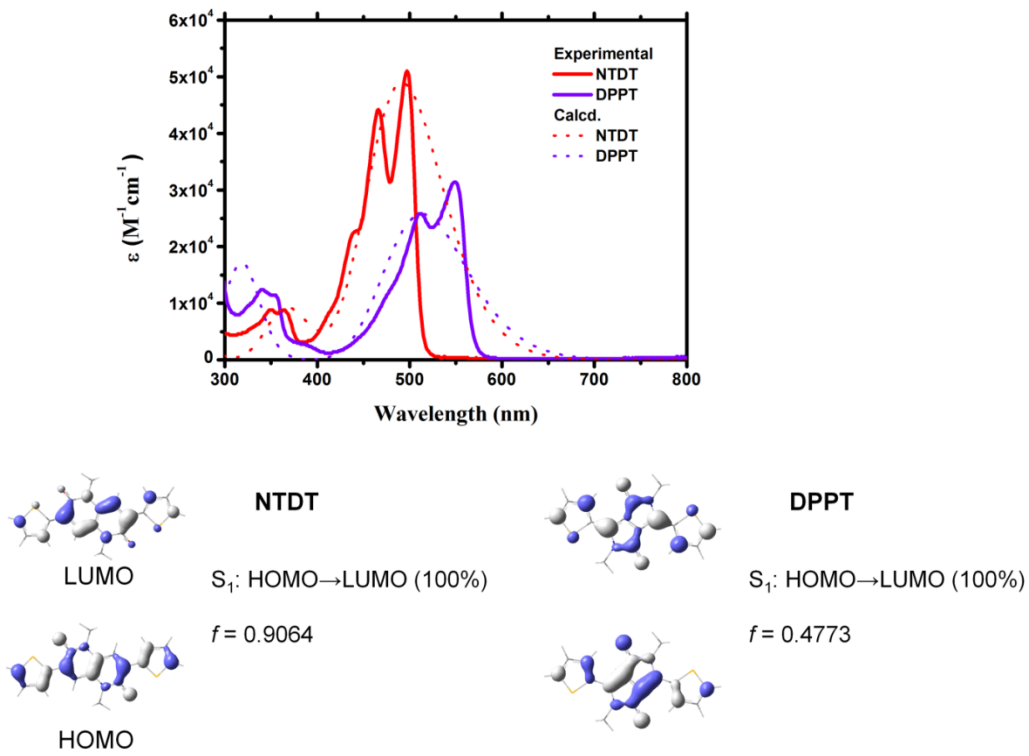

Figure 3-6. S_0–S_1 transition energy spectra of NTDT and DPPT.

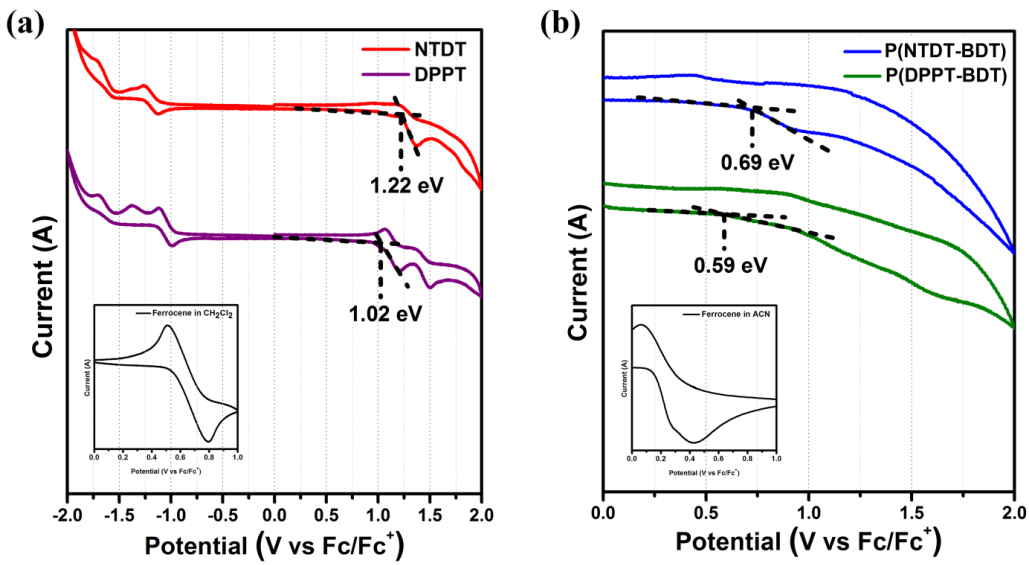

Figure 3-7. Cyclic voltammetry (CV) curves of (a) the two monomers in CH_2Cl_2/0.1 M Bu_4NBF_4 and (b) the two polymers in thin film state (inset: CV of ferrocene shown for comparison).

3.2.5. Photovoltaic properties

PSCs were fabricated using each of the two polymers as the electron donor and $PC_{71}BM$ as the electron acceptor. The structure of the devices was that of a conventional BHJ device: ITO/PEDOT:PSS/polymer:$PC_{71}BM$/Ca/Al. In order to optimize the performances of the PSCs, I fabricated the devices under different conditions by varying the solvent conditions and polymer concentrations. To optimize the charge-transporting network of the photoactive layer, I also used various additives, such as 1,2-dichlorobenzene (DCB) and 1,8-diiodooctane (DIO) (**Table 3-4**).[69,70] The PSC devices without an additive were found to exhibit low PCEs; this was the case for both P(NTDT-BDT) and P(DPPT-BDT). The device formed using P(NTDT-BDT)/$PC_{71}BM$ = 1:2 (w/w) and in which DCB was added to $CHCl_3$ ($CHCl_3$/DCB = 85:15 v/v) showed the best performance, with the V_{oc} of 0.72 V, the J_{sc} of 16.99 mA cm^{-2}, the fill factor (FF) of 0.58, and the PCE of 7.11% (**Table 3-5** and **Figure 3-8**a). In the case of the P(DPPT-BDT)-based device, the addition of DIO to $CHCl_3$ ($CHCl_3$/DIO = 95:5 v/v) resulted in the optimization of its performance, with V_{oc} of 0.66 V, J_{sc} of 7.72 mA cm^{-2}, the FF of 0.60, and the PCE of 3.08% (**Table 3-5** and **Figure 3-8**b); these values are comparable to previously reported results.[63-65] The higher V_{oc} value of the P(NTDT-BDT):$PC_{71}BM$ device was consistent with the fact that the HOMO level of P(NTDT-BDT) was lower than that of P(DPPT-BDT).

To further improve the performance of the P(NTDT-BDT) device, inverted devices were fabricated with the ITO/ZnO/polyethyleneimine/polymer:$PC_{71}BM$/MoO_3/Ag configuration. **Figure 3-9**a shows the current-voltage (*J*-*V*) characteristics of the optimized inverted PSC device; the other related data are listed in **Table 3-5**. The inverted device exhibited higher J_{sc} (18.51 mA cm^{-2}) and FF (0.63) than those of the conventional cell. To the best of my knowledge, this J_{sc} value of P(NTDT-BDT) is the highest value yet reported for BDT-based polymer in PSCs.[71] As a result, the inverted device exhibited the highest PCE, which was 8.16%. The corresponding incident photon-to-current efficiency (IPCE) of the polymer:$PC_{71}BM$ devices under the optimized conditions are displayed in **Figure 3-9**b; it can be seen that the integrated current values from the IPCE spectrum (18.06 mA cm^{-2} for P(NTDT-BDT) device and 7.22 mA cm^{-2} for P(DPPT-BDT) device) are well matched with the J_{sc} values obtained from their *J*-*V* curves.

Table 3-4. Photovoltaic parameters of polymer:$PC_{71}BM$ (1:2 w/w) BHJ devices[a] fabricated under different conditions.

Polymer	Solvent	Polymer conc. [mg mL^{-1}]	V_{oc} [V]	J_{sc} [mA cm^{-2}]	FF	PCE (PCE_{max}) [%]
P(NTDT-BDT)[b]	$CHCl_3$	16	0.70	3.18	0.57	1.28 ± 0.26 (1.54)
	$CHCl_3$ + 5 vol% DIO	16	0.72	9.61	0.55	3.81 ± 0.40 (4.33)
		18	0.72	12.70	0.48	4.35 ± 0.10 (4.48)
		20	0.72	12.72	0.45	4.15 ± 0.10 (4.25)
	$CHCl_3$ + 5 vol% DCB	16	0.73	11.70	0.64	5.41 ± 0.31 (5.85)
		18	0.72	12.43	0.61	5.46 ± 0.24 (5.78)
		20	0.72	13.21	0.58	5.48 ± 0.22 (5.75)
	$CHCl_3$ + 10 vol% DCB	16	0.71	12.97	0.59	5.38 ± 0.22 (5.79)
		18	0.73	12.57	0.56	5.15 ± 0.17 (5.27)
		20	0.70	14.43	0.50	5.03 ± 0.16 (5.22)
	$CHCl_3$ + 15 vol% DCB	16	0.71	12.12	0.61	5.20 ± 0.26 (5.60)
		18	0.71	14.23	0.61	6.16 ± 0.20 (6.39)
		20	**0.71**	**15.52**	**0.60**	**6.67 ± 0.23 (7.11)**
P(DPPT-BDT)[c]	$CHCl_3$	16	0.64	2.08	0.48	0.65 ± 0.24 (0.97)
	$CHCl_3$ + 5 vol% DCB	16	0.62	5.05	0.41	1.29 ± 0.13 (1.51)
	$CHCl_3$ + 5 vol% DIO	**16**	**0.65**	**7.50**	**0.61**	**2.95 ± 0.08 (3.08)**
		18	0.65	7.07	0.61	2.80 ± 0.16 (3.01)
		20	0.68	6.24	0.53	2.23 ± 0.23 (2.62)

[a]ITO/PEDOT:PSS/polymer:$PC_{71}BM$/Ca/Al; [b]Average values of P(NTDT-BDT) devices were obtained from 10 devices; [c]Average values of P(DPPT-BDT) devices were obtained from 5 devices.

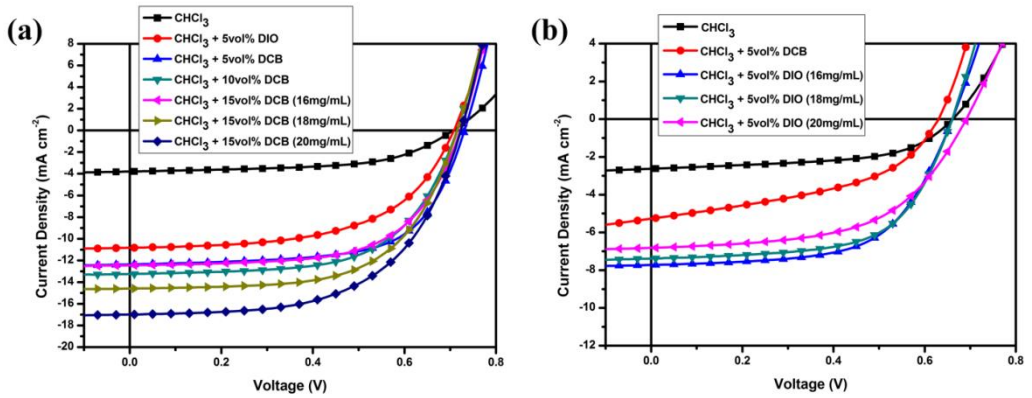

Figure 3-8. Current density-voltage (*J*–*V*) of conventional photovoltaic devices based on (a) P(NTDT-BDT):$PC_{71}BM$ and (b) P(DPPT-BDT): $PC_{71}BM$ blends.

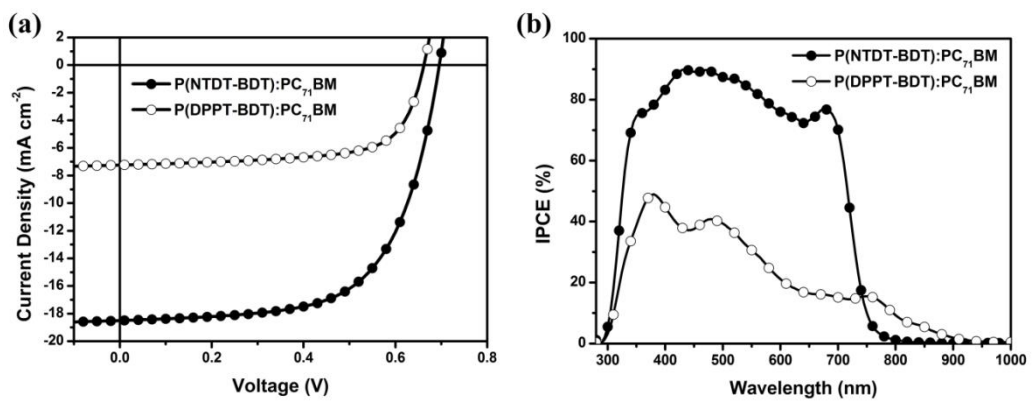

Figure 3-9. (a) Current density-voltage (*J*–*V*) curves and (b) IPCE spectra of optimized inverted photovoltaic devices based on P(NTDT-BDT):$PC_{71}BM$ and P(DPPT-BDT): $PC_{71}BM$ blends.

Table 3-5. Photovoltaic parameters of optimized P(NTDT-BDT):$PC_{71}BM$ and P(DPPT-BDT):$PC_{71}BM$ BHJ devices.[a)]

Polymer[b)]	V_{oc}[c)] (V)	J_{sc}[c)] (mA cm^{-2})	FF[c)]	PCE[c)] (%)
P(NTDT-BDT)	0.70 (0.70 ± 0.01)	18.51 (17.10 ± 0.89)	0.63 (0.64 ± 0.01)	8.16 (7.64 ± 0.27)
P(DPPT-BDT)	0.66 (0.65 ± 0.01)	7.24 (6.74 ± 0.35)	0.68 (0.67 ± 0.01)	3.26 (2.95 ± 0.18)

[a)]ITO/PEDOT:PSS/polymer:$PC_{71}BM$/Ca/Al; [b)]Average values of P(NTDT-BDT) devices were obtained from 10 devices; [c)]Average values of P(DPPT-BDT) devices were obtained from 5 devices.

3.2.6. Morphology investigation

To investigate the ordered structures of solid-state films of these polymers, grazing incidence wide-angle X-ray scattering (GIWAXS) measurements were carried out on pristine films of the polymers as well as polymer:$PC_{71}BM$ blended films and polymer:$PC_{71}BM$ blended films with additives (**Figure 3-10**). The GIWAXS pattern of the pristine P(NTDT-BDT) film showed interlamellar stacking (*h*00) peaks in the in-plane direction and a π–π stacking peak (010) in the out-of-plane direction at q_z = 1.68 $Å^{-1}$, which corresponded to face-on π–π stacking. The face-on orientation of P(NTDT-BDT) is suitable for increasing the vertical charge-carrier mobility and resulted in a high J_{sc} value in the corresponding PSCs.[72-74] On the other hand, the GIWAXS pattern of the pristine P(DPPT-BDT) film displayed weak and broad interlamellar scattering (*h*00) and (010) peaks in both the in-plane and the out-of-plane directions, indicating that P(DPPT-BDT) exhibits a mix of face-on and edge-on orientations. Furthermore, the π–overlap distances (d_π) in the pristine polymer films were calculated to be 3.74 Å (q_z = 1.68 $Å^{-1}$) and 3.78 Å (q_z = 1.66 $Å^{-1}$) for P(NTDT-BDT) and P(DPPT-BDT), respectively. When P(NTDT-BDT) was blended with $PC_{71}BM$ (**Figure 3-10**c) and $PC_{71}BM$/DCB additive (**Figure 3-10**e), the intensities of the π–π stacking peak (010) in the out-of-plane direction somewhat decreased; however, the blended films exhibited diffraction patterns similar to those of the pristine polymer films; the only difference

was that the diffraction pattern of $PC_{71}BM$ was present in the case of the blended films, indicating that the blend films maintain the face-on orientation due to the highly crystalline nature of P(NTDT-BDT). In case of P(DPPT-BDT)**,** however, diffraction patterns of the blended films were quite different from those of the pristine film. As shown in **Figure 3-10**d, the π–π stacking peak (010) in the q_z direction disappered, indicating that the molecular ordering of P(DPPT-BDT) could be easily affected by the presence of $PC_{71}BM$. After adding the DIO additive (**Figure 3-10**f), however, the molecular orientation largely changed to normal to the substrate plane again, which is beneficial for vertical charge transport.

Atomic force microscopy (AFM) and transmission electron microscopy (TEM) were used for investigating the nanoscale morphologies of the two polymers (**Figure 3-11**). The effect of the additive treatment could be visualized through the AFM and TEM images. When an additive was not used, both the P(NTDT-BDT):$PC_{71}BM$ and P(DPPT-BDT):$PC_{71}BM$ blend films exhibited macroscopic phase separation between the polymer and $PC_{71}BM$. After treatment with an additive, however, bicontinuous network with finer nanoscale features was observed in the P(NTDT-BDT):$PC_{71}BM$ blend film. Although the additive treatment of P(DPPT-BDT):$PC_{71}BM$ blend was also effective to form the nanoscale morphology, they showed poorer film homogeneity with high root-mean-square roughness (6.23 nm) than the P(NTDT-BDT):$PC_{71}BM$ blend film (1.02 nm). Thus, the more extensive and homogeneous interface formed in the P(NTDT-BDT):$PC_{71}BM$ blend film led to more efficient charge separation,

resulting in the J_{sc} values of the PSC devices based on this blend film being higher than those of the devices based on the P(DPPT-BDT):$PC_{71}BM$ blend film.

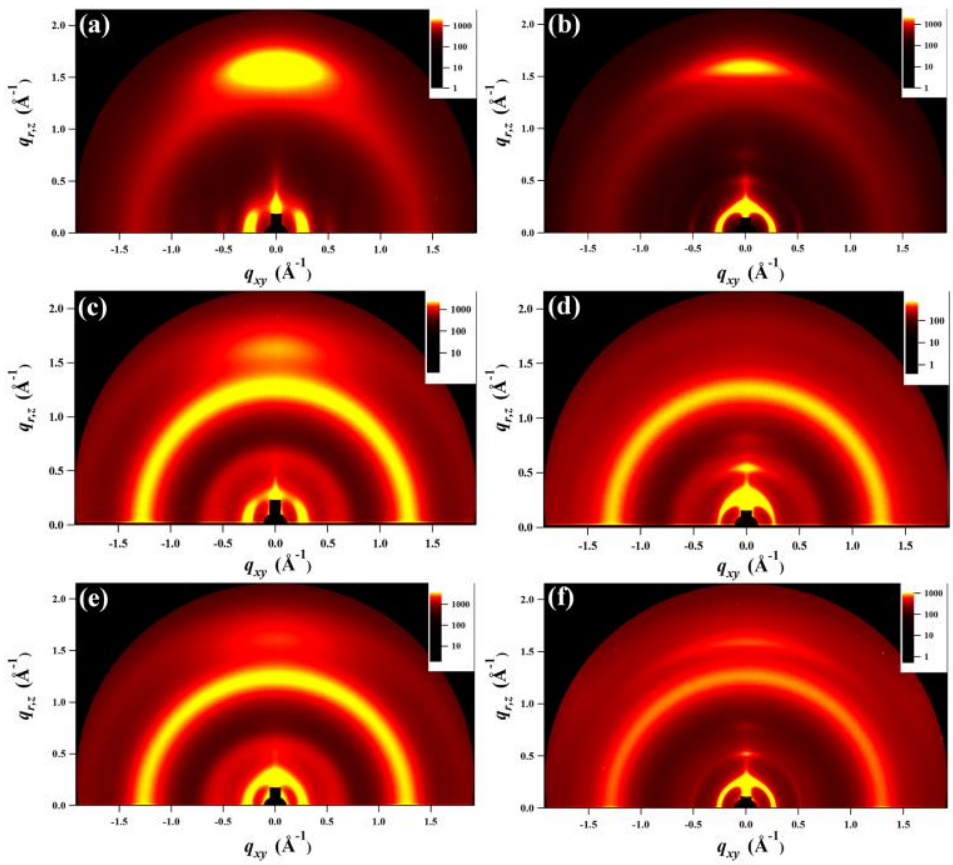

Figure 3-10. Two-dimensional GIWAXS images of pristine films of (a) P(NTDT-BDT) and (b) P(DPPT-BDT), films of (c) P(NTDT-BDT):$PC_{71}BM$ and (d) P(DPPT-BDT):$PC_{71}BM$ blends and optimized films of (e) P(NTDT-BDT):$PC_{71}BM$ with 15 vol% DCB and (f) P(DPPT-BDT):$PC_{71}BM$ with 5 vol% DIO blends.

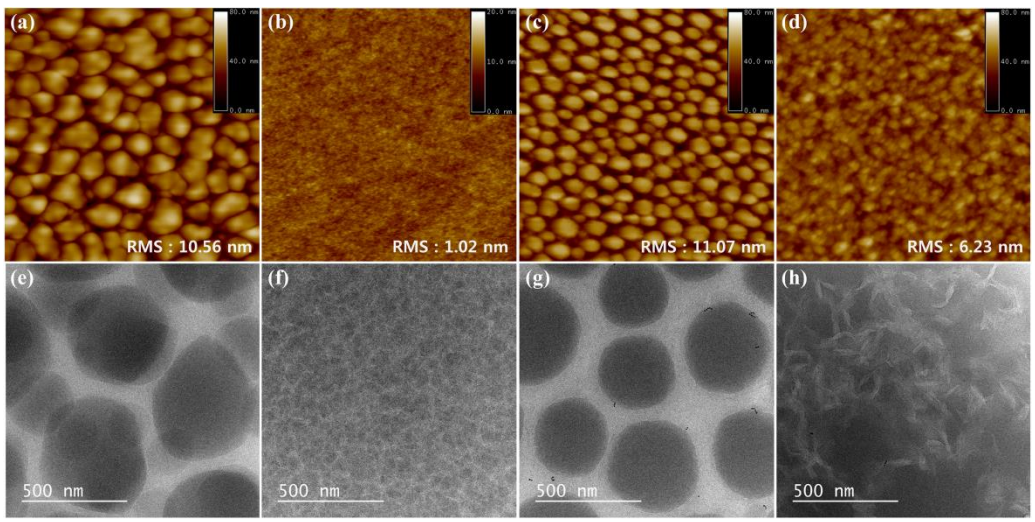

Figure 3-11. (a−d) AFM height images (5 μm × 5 μm) of (a) P(NTDT-BDT):$PC_{71}BM$ blend film, (b) P(NTDT-BDT):$PC_{71}BM$:additive (DCB; 15 vol%) blend film, (c) P(DPPT-BDT):$PC_{71}BM$ blend film, and (d) P(DPPT-BDT):$PC_{71}BM$:additive (DIO; 5 vol%) blend film; (e−h) TEM images of (e) P(NTDT-BDT):$PC_{71}BM$ blend film, (f) P(NTDT-BDT):$PC_{71}BM$:additive (DCB; 15 vol%) blend film, (g) P(DPPT-BDT):$PC_{71}BM$ blend film, and (h) P(DPPT-BDT):$PC_{71}BM$:additive (DIO; 5 vol%) blend film.

3.2.7. Charge carrier transport properties

To further elucidate the charge-transport characteristics of the polymers, their charge-carrier mobilities were investigated by using the space-charge-limited current (SCLC) model as well as organic field-effect transistors (OFETs). The measured SCLC hole mobilities of P(NTDT-BDT) and P(DPPT-BDT) were found to be 3.4×10^{-3} cm^2 V^{-1} s^{-1} and 2.5×10^{-4} cm^2 V^{-1} s^{-1}, respectively (**Figure 3-12**). The field-effect mobilities of the two polymers were determined by using the polymers for the active layers in typical bottom-gate top-contact OFETs. As shown in **Figure 3-13**, P(NTDT-BDT) and P(DPPT-BDT) exhibited *p*-type organic semiconductor characteristics (hole mobility of 5.8×10^{-3} cm^2 V^{-1} s^{-1} for P(NTDT-BDT) and 1.2×10^{-2} cm^2 V^{-1} s^{-1} for P(DPPT-BDT)). That is to say, P(NTDT-BDT) exhibited a much higher hole mobility than P(DPPT-BDT) in the vertical direction (SCLC method; the charge carriers flowed in the vertical direction), while P(DPPT-BDT) showed a higher hole mobility than P(NTDT-BDT) in the lateral direction (OFET; the charge carriers flowed in the lateral direction). From these results, it was concluded that the preferentially face-on oriented P(NTDT-BDT) film was more suitable for vertical charge transport than the mixed (face-on + edge-on) orientation P(DPPT-BDT) film. This leads to a higher J_{sc} values for P(NTDT-BDT).

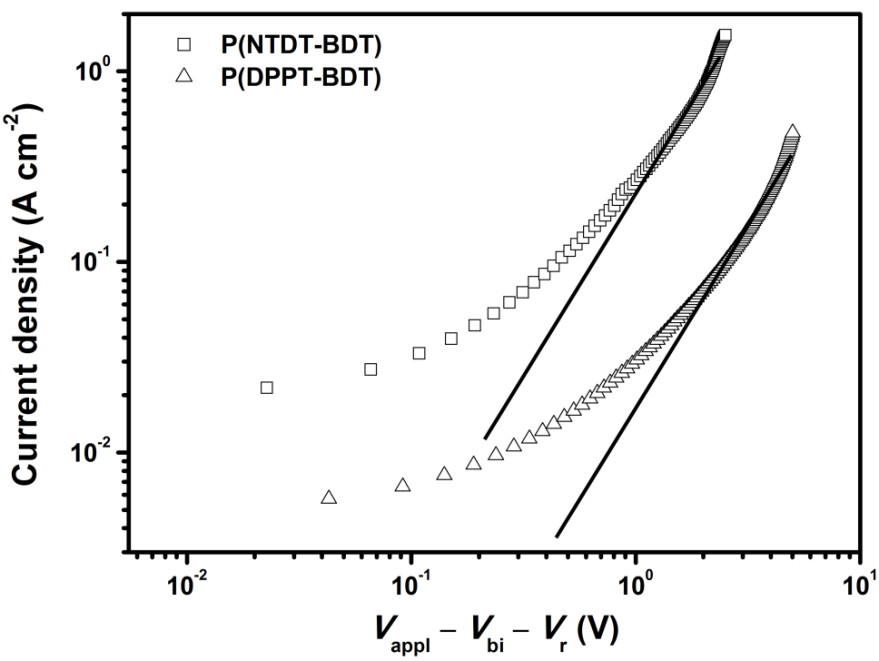

Figure 3-12. *J-V* curves of hole-only P(NTDT-BDT):$PC_{71}BM$ and P(DPPT-BDT):$PC_{71}BM$ devices.

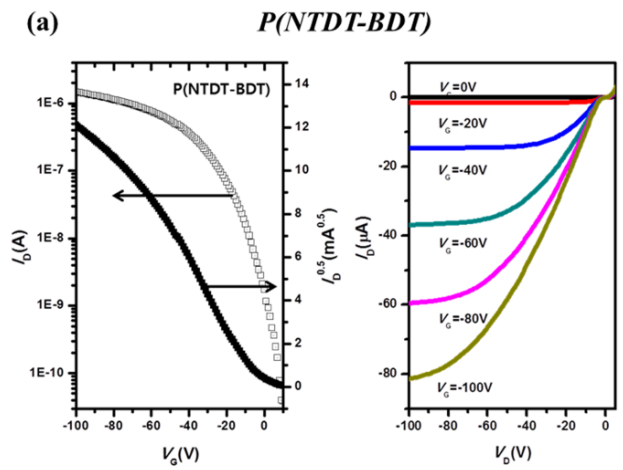

$\mu_{h,max}$ = **5.8 x 10^{-3}** cm^2 v^{-1} s^{-1}
$\mu_{h,avg}$ = 3.4 x 10^{-3} cm^2 v^{-1} s^{-1}

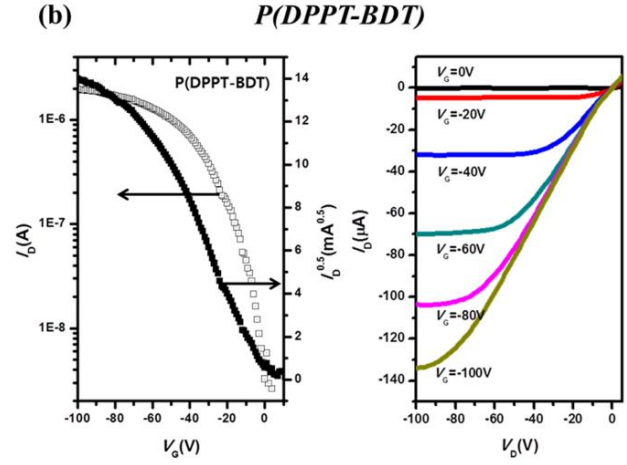

$\mu_{h,max}$ = **1.2 x 10^{-2}** cm^2 v^{-1} s^{-1}
$\mu_{h,avg}$ = 5.6 x 10^{-3} cm^2 v^{-1} s^{-1}

Figure 3-13. Transfer and output curves of spin-coated (a) P(NTDT-BDT) and (b) P(DPPT-BDT) films.

3.3. Experimental

Materials and Characterization: All commercially available reagents were purchased from Sigma Aldrich Chemical Co., Tokyo Chemical Industry Co., or Alfa Aesar Co., and were used without further purification. 6-methoxy-1,5-naphthyridin-2(1H)-one (2), 3,6-bis(5-bromothiophen-2-yl)-2,5-dioctyl-2,5-dihydropyrrolo[3,4-*c*]pyrrole-1,4-dione (M2) and (4,8-bis((2-octyldodecyl)oxy)benzo[1,2-*b*:4,5-*b*']dithiophene-2,6-diyl)bis(trimethylstannane) (M3) were prepared following previously reported in the literature.[75,76] Chemical structures were fully identified by ^{1}H NMR (Bruker, Avance-300) and elemental analysis EA1110, CE Instrument). The thermal properties of the compounds were obtained using TGA under an N_2 atmosphere, with a TA instruments Q50 model. Single crystal structures were analyzed by using SMART–APEX II ULTRA (Bruker) in Central Instrument Facility, Gyeongsang National University. UV-Vis absorption spectra were recorded on a SHIMADZU UV-1650PC spectrometer. The cyclic voltammetry experiments were carried out using a Princeton Applied Research Potentiostat/Galvanostat Model 273A (Princeton Applied Research) onto which was configured a three electrode cell assembly including an ITO-coated glass working electrode, a platinum wire counter electrode, and a silver wire quasi-reference electrode. The HOMO levels were estimated based on the onset oxidation potentials (E_{ox}), and E_{ox} was calibrated using ferrocene ($E_{Fc/Fc+}$) as a reference (Energy level = $-[E_{ox} - E_{Fc/Fc+} + 4.8]$). The film thickness was measured using a KLA Tencor Alpha-

Step IQ surface profiler. The GIWAXS measurements were taken at the PLS-II 9A U-SAXS beamline (X-ray E = 11.06 keV, λ= 1.121 Å) of the Pohang Accelerator Laboratory in Korea. The incidence angle was adjusted to 0.08–0.14°. Atomic force microscopy (AFM) was performed using a Multimode with a Nano Scope V controller, Bruker, in the tapping mode.

Device fabrication and Evaluation

OPV device fabrication and measurements

The patterned indium tin oxide (ITO) glass substrates were cleaned in an ultrasonic bath with distilled water, acetone, and isopropanol, and then exposed to a UV-ozone clean for 20 min. For the conventional devices, a PEDOT:PSS (Clavious P VP AI 4083) was spin-coated onto the ITO glass substrate at 5000 rpm for 30 s (30nm) and dried on a hot plate at 150℃ for 10 min. The blend solutions of polymers and $PC_{71}BM$ in $CHCl_3$/additive were fully dissolved at 50℃ overnight before use. The blend solutions were filtered using 0.50 μm syringe filters and deposited through spin casting onto the PEDOT:PSS coated ITO glass in a N_2 glovebox. After drying the resulting films in a N_2 glovebox at room temperature for 1 hour, a 5 nm layer of Ca and a 100 nm layer of Al were deposited by thermal evaporation under a vacuum of 10^{-6} Torr. For the inverted organic solar cells, sol-gel ZnO solution was spin-coated onto the ITO glass substrate (~20nm) and annealed at 150℃ on a hot plate for 10 min. Polyethylene imine (PEI) was spin-coated onto the ZnO layer (~2nm) and dried on a hot plate at 100℃ for

10 min. The blend solutions of polymers and $PC_{71}BM$ in $CHCl_3$/additive were then spin-coated in a N_2 glovebox. Subsequently, MoO_3 (10nm) and Ag (100nm) were deposited by thermal evaporation under a vacuum of 10^{-6} Torr. The current density-voltage (*J*–*V*) characteristics of the solar cells were measured using a Keithley 4200 source measurement unit. The solar cell performances were characterized under AM 1.5G condition with an illumination intensity of 100 mW cm^{-2}, as generated using an Oriel Sol3A solar simulator (Oriel model 94023A). The measurements were carried out through a shadow mask with well-defined aperture area of 0.04 cm^2 under an ambient atmosphere. The incident photon-to-current efficiency (IPCE) was measured using an Oriel QE/IPCE Measurement Kit composed of a 300 W xenon lamp, a monochromator (74125), an order sorting filter wheel, a Merlin lock-in amplifier (70104), a calibrated silicon photodiode (70356_70316NS) and an optical chopper.

Mobility measurements (SCLC)

The hole mobilities were measured using the SCLC model, using a device configuration of ITO/PEDOT:PSS/P(NTDT-BDT) or P(DPPT-BDT):$PC_{71}BM$/MoO_3/Ag for the hole-only devices. The SCLC mobilities were calculated using the following Mott-Gurney law:

$$J = \frac{9}{8}\varepsilon_r\varepsilon_0\mu_0\frac{V^2}{L^3}$$

where J is the current density, ε_r is the dielectric constant of the polymer (dielectric

constant assumed to be 3), ε_0 is the permittivity of free space, μ_0 is the zero-field hole mobility, L is the polymer thickness, and the effective voltage, $V = V_{appl} - V_{bi} - V_r$, where V_{appl} is the applied voltage to the device, V_{bi} is the built-in voltage, and V_r is the voltage drop. The J–V curves of the devices were measured using a Keithley 4200 source measurement unit.

Mobility measurements (OFET)

Prior to device fabrication, SiO_2/Si (300 nm thick SiO_2) substrates were rinsed by sonication in acetone and isopropyl alcohol. The substrates were then exposed to a UV-ozone clean for 20 min. Then substrates were treated by octadecyltrichlorosilane (ODTS). Series of P(NTDT-BDT) and P(DPPT-BDT) active layers were spin coated on the ODTS treated SiO_2/Si wafer with a spin rate of 2500rpm under ambient conditions at room temperature. The 50 nm thick source–drain Au electrodes were thermally deposited directly onto the active layers through a metal mask to fabricate top-contact OFETs (the deposition rate was 0.1–0.2 k Å s^{-1}). The current–voltage characteristics of the OFETs were measured using a Keithley 4200 connected to a probe station.

Synthesis of 3,6-di(thiophen-2-yl)pyrrolo[3,4-c]pyrrole-1,4(2H,5H)-dione (2): The precursor (a) was synthesized according to the procedure reported previously. To a solution of tert-amyl alcohol (120 mL) in a two-necked 500 mL round-bottom flask were slowly added sodium metal pieces (4.21 g, 183.23 mmol) under an Ar atmosphere.

The mixture was heated to 120℃ and stirred for 3 h. 2-Thiophenecarbonitrile (10 g, 91.62 mmol) was added, followed by the dropwise addition of diethylsuccinate (6.38 g, 36.65 mmol) to the reaction mixture over 1 h. The mixture was stirred at 120℃ for 3 h, and then cooled to room temperature. The mixture were poured into acidic MeOH (200 mL MeOH and 10 mL HCl) in an ice bath and stirred for 1.5 h. The suspension was filtered, yielding a dark red solid, which was used in next step without further purification. Yield: 64.52% (17.76 g).

Synthesis of 1,5-dihydro-1,5-naphthyridine-2,6-dione (3): In a two-necked 250 mL round-bottom flask, compound (2) (2.34 g, 13.28 mmol) was taken up in 48% HBr in water (59 mL), and the solution was heated to 125℃ and stirred for 2.5h. After the reaction had gone to completion, the solution was cooled to room temperature, and the PH was adjusted to ~7. The solid was collected by vacuum filtration and washed with water and then dried under vacuum to give a beige solid. Yield: 95.18% (2.05 g). Anal. calcd for $C_8H_6N_2O_2$: C 59.26, H 3.73, N 17.28; found: C 58.62, H 3.84, N 16.90. HRMS (ESI, m/z): $[M + H]^+$ calcd for $C_8H_7N_2O_2$ 163.0508; Found 163.0508.

Synthesis of 1,5-dioctyl-1,5-naphthyridine-2,6-dione (4, NTD): In a two-necked 100 mL round-bottom flask, compound (3) (1.85 g, 11.41 mmol) and cesium carbonate (4.84 g, 14.85 mmol) were taken up in DMSO (20 mL), and the solution was stirred under an Ar atmosphere. Then to this was added 1-bromooctane (3.26 mL, 18.87

mmol), and further stirred for 24h at 95℃. After the reaction had gone to completion, the solution was cooled to room temperature. Water was added to the reaction mixture and extracted using EtOAc. The organic phase was washed with water three times and dried over anhydrous $MgSO_4$. The residual solvent in the crude product was evaporated by rotary evaporation, and the crude product was purified by column chromatography (MC/MeOH, 99:1 v/v) to give a yellow powder. Yield: 8.62% (0.38 g). ^{1}H NMR (300 MHz, $CDCl_3$, δ): 7.55 (d, J = 10.1 Hz, 2H), 6.88 (d, J = 10.0Hz, 2H), 4.22 (t, J = 7.6 Hz, 4H), 1.73 (m, 4H), 1.49–1.20 (m, 24H), 0.88 (t, J = 6.9 Hz, 6H). Anal. calcd for $C_{24}H_{38}N_2O_2$: C 74.57, H 9.91, N 7.25; found: C 74.31, H 9.73, N 7.25. HRMS (ESI, m/z): $[M + H]^+$ calcd for $C_{24}H_{39}N_2O_2$ 387.3012; Found 387.3011.

Synthesis of 3,7-dibromo-1,5-dioctyl-1,5-naphthyridine-2,6-dione (5): In a two-necked 100 mL round-bottom flask, compound (4) (0.26 g, 0.67 mmol) was dissolved in $CHCl_3$ (15 mL), and the solution was stirred. To this solution was added bromine (0.076 mL, 1.48 mmol), and the solution was heated to 55℃ and stirred overnight. After the reaction had gone to completion, the solution was cooled to room temperature, poured into MeOH (60 mL), and the solid was collected by vacuum filtration. The solid was washed with water and methanol several times and then dried under vacuum to obtain an orange solid. Yield: 57.36% (0.21 g). ^{1}H NMR (300 MHz, $CDCl_3$, δ): 7.94 (s, 2H), 4.26 (t, J = 8.4 Hz, 4H), 1.72 (m, 4H), 1.49–1.21 (m, 24H), 0.89 (t, J = 6.9 Hz, 6H). Anal. calcd for $C_{24}H_{36}Br_2N_2O_2$: C 52.95, H 6.67, N 5.15; found: C 53.38, H 6.62,

N 5.15. HRMS (ESI, m/z): $[M + H]^+$ calcd for $C_{24}H_{37}Br_2N_2O_2$ 543.1222; Found 543.1223.

Synthesis of 1,5-dioctyl-3,7-dithiophen-2-yl-1,5-naphthyridine-2,6-dione (6, NTDT): In a two-necked 25 mL round-bottom flask, compound (5) (0.21 g, 0.39 mmol) and tributyl(thiophen-2-yl)stannane (0.37 mL, 1.16 mmol) were dissolved in degassed DMF (7 mL), and the solution was stirred under an Ar atmosphere. To this solution was added $Pd(PPh_3)_4$ (0.023 g, 0.02 mmol), and the solution was heated to 130℃ and stirred overnight. After the reaction had gone to completion, the solution was cooled to room temperature. Water was added to the reaction mixture and extracted using MC. The organic phase was washed with brine three times and dried over anhydrous $MgSO_4$, and evaporated by rotary evaporation. The crude product was purified by column chromatography (MC/MeOH, 99:1 v/v) to give a red solid. Yield: 75.30% (0.16 g). ^1H NMR (300 MHz, $CDCl_3$, δ): 7.97 (s, 2H), 7.78 (d, J = 3.5 Hz, 2H), 7.54 (d, J = 4.5 Hz, 2H), 7.18 (t, J = 4.6 Hz, 2H), 4.43 (t, J = 7.2 Hz, 4H), 1.84 (m, 4H), 1.49–1.21 (m, 24H), 0.89 (t, J = 6.8 Hz, 6H). Anal. calcd for $C_{32}H_{42}N_2O_2S_2$: C 69.78, H 7.69, N 5.09, S 11.64; found: C 69.66, H 7.40, N 5.10, S 10.95. HRMS (ESI, m/z): $[M + H]^+$ calcd for $C_{32}H_{43}N_2O_2S_2$ 551.2766; Found 551.2766.

Synthesis of 3,7-bis(5-bromothiophen-2-yl)-1,5-dioctyl-1,5-naphthyridine-2,6-dione (M1): In a two-necked 50 mL round-bottom flask, compound (6) (0.16 g, 0.29 mmol)

was dissolved in $CHCl_3$ (20 mL), and the solution was stirred at 0℃. To this solution was added N-bromosuccinimide (NBS) (0.10 g, 0.59 mmol), and the solution was heated to 25℃ and stirred overnight. After the reaction had gone to completion, the solution was cooled to room temperature, and then water was added to the reaction mixture and extracted using $CHCl_3$. The organic phase was washed with brine three times and dried over anhydrous $MgSO_4$, and evaporated by rotary evaporation. The crude product was purified by column chromatography (MC/ EtOAc/n-Hexane, 20:1:30 v/v/v) to give a red solid. Yield: 68.02% (0.14 g). ^{1}H NMR (300 MHz, $CDCl_3$, δ): 7.89 (s, 2H), 7.46 (d, J = 4.2 Hz, 2H), 7.14 (d, J = 4.0 Hz, 2H), 4.40 (t, J = 7.9 Hz, 4H), 1.80 (m, 4H), 1.49–1.21 (m, 24H), 0.89 (t, J = 6.4 Hz, 6H). Anal. calcd for $C_{32}H_{40}Br_2N_2O_2S_2$: C 54.24, H 5.69, N 3.95, S 9.05; found: C 54.37, H 5.53, N 3.97, S 8.99. HRMS (ESI, m/z): $[M + H]^+$ calcd for $C_{32}H_{41}Br_2N_2O_2S_2$ 707.0976; Found 707.0975.

Polymerization for P(NTDT-BDT): In an oven-dried 50 mL Schlenk flask, M1 (100 mg, 0.141 mmol), M3 (157 mg, 0.141 mmol), (*o*-tol)$_3$P (3.8 mg, 0.012 mmol) and $Pd_2(dba)_3$ (2.8 mg, 0.003 mmol) were added. The flask was purged three times with successive vacuum and argon filling cycle, and then anhydrous toluene (5 mL) was added. After 5 mL of distilled toluene was added, the solution was refluxed for 1 h under an Ar atmosphere. After cooling down to room temperature, the solution was precipitated into MeOH. The solid was further purified by Soxhlet extraction with MeOH, acetone,

hexane, MC and then $CHCl_3$. Finally the $CHCl_3$ fraction was concentrated, and then precipitated in MeOH. The dark purple solid was obtained after filtering and vacuum drying. Yield: 62.83% (140 mg). GPC: (Mn = 60 kDa, PDI = 3.1). ^{1}H NMR (400 MHz, 1,1,2,2-tetrachloroethane-d_2, 110 ˚C, δ): 7.82–7.43 (br, 2H), 7.39–6.45 (br, 6H), 4.48–3.51 (br, 8H), 2.11–0.55 (br, 108H). Anal. calcd: C 73.93, H 9.53, N 2.10, S 9.63; found: C 73.84, H 9.47, N 2.10, S 9.40.

Polymerization for P(DPPT-BDT): P(DPPT-BDT) was synthesized from M2 (100 mg, 0.147 mmol), M3 (163 mg, 0.147 mmol) by following a same procedure as P(NTDT-BDT). The resulting co-polymer P(DPPT-BDT) was obtained as a dark blue solid. Yield: 66.81% (152 mg). GPC: (Mn = 59 kDa, PDI = 2.8). ^{1}H NMR (400 MHz, 1,1,2,2-tetrachloroethane-d_2, 110 ˚C, δ): 9.03 (br, 2H), 7.72–6.75 (br, 4H), 4.29–3.71 (br, 8H), 2.07–0.74 (br, 108H). Anal. calcd: C 73.57, H 9.57, N 2.14, S 9.82; found: C 73.57, H 9.58, N 2.13, S 9.89.

3.4. Conclusion

I synthesized and characterized a novel bis-lactam-based A building block, NTDT, for D-A type conjugated polymers. The NTDT unit exhibits a high coplanarity of the conjugated backbone owing to the intramolecular S···O interactions. The electron-deficient nature and quasi-planar structure with remarkably high molar extinction coefficient of the NTDT unit could allow for the realization of high efficient D-A copolymer. In fact, the NTDT incorporated conjugated polymer P(NTDT-BDT) exhibited a deeper HOMO level, higher absorption coefficient, and higher vertical charge-carrier mobility than those of the widely used copolymer P(DPPT-BDT). Furthermore, P(NTDT-BDT) also exhibited the appropriate nanoscale morphology and the proper ordered structure with a coplanar geometry. All these factors ensured that the PSCs based on P(NTDT-BDT) exhibited better performance. As a result, a BHJ PSC device based on P(NTDT-BDT) with $PC_{71}BM$ showed an high PCE of 8.16% with a high J_{sc} value of 18.51 mA cm^{-2}. This J_{sc} value is one of the highest values yet obtained for BDT-based polymer in PSCs. Based on these results, I strongly believe that the NTDT is a promising building block for conjugated polymers and can potentially replace DPPT in organic solar cells.

3.5. Reference

[1] S. Günes, H. Neugebauer, N. S. Sariciftci, *Chem. Rev.* **2007**, *107*, 1324.

[2] F. C. Krebs, *Sol. Energy Mater. Sol. Cells* **2009**, *93*, 394.

[3] C. J. Brabec, *Sol. Energy Mater. Sol. Cells* **2004**, *83*, 273.

[4] S. B. Darling,; F. You, *RSC Adv.* **2013**, *3*, 17633.

[5] M. C. Scharber, N. S. Sariciftci, *Prog. Polym. Sci.* **2013**, *38*, 1929.

[6] J. B. You, L. T. Dou, K. Yoshimura, T. Kato, K. Ohya, T. Moriarty, K. Emery, C.-C. Chen, J. Gao, G. Li, Y. Yang, *Nat. Commun.* **2013**, *4*, 1446.

[7] Y. H. Liu, J. B. Zhao, Z. K. Li, C. Mu, W. Ma, H. Hu, K. Jiang, H. R. Lin, H. Ade, H. Yan, *Nat. Commun.* **2014**, *5*, 5293.

[8] Z. He, B. Xiao, F. Liu, H. Wu, Y. Yang, S. Xiao, C. Wang, T. P. Russell, Y. Cao, *Nat. Photonics* **2015**, *9*, 174.

[9] C. Liu, C. Yi, K. Wang, Y. Yang, R. S. Bhatta, M. Tsige, S. Xiao, X. Gong, *ACS Appl. Mater. Interfaces* **2015**, *7*, 4928.

[10] H. Q. Zhou, Y. Zhang, C. K. Mai, S. D. Collins, G. C. Bazan, T.-Q. Nguyen, A. J. Heeger, *Adv. Mater.* **2015**, *27*, 1767.

[11] J. Zhao, Y. Li, G. Yang, K. Jiang, H. Lin, H. Ade, W. Ma, H. Yan, *Nat. Energy* **2016**, *1*, 15027.

[12] W. Zhao, D. Qian, S. Zhang, S. Li, O. Inganäs, F. Gao, J. Hou, *Adv. Mater.*

2016, *28*, 4734.

[13] S. K. Hau, H.-L. Yip, A. K.-Y. Jen, *Polym. Rev.* **2010**, *50*, 474.

[14] W. Cao, J. Xue, *Energy Environ. Sci.* **2014**, *7*, 2123.

[15] A. Facchetti, *Chem. Mater.* **2011**, *23*, 733.

[16] L. Bian, E. Zhu, J. Tang, W. Tang, F. Zhang, *Prog Polym Sci.* **2012**, *37*, 1292.

[17] H. Benten, D. Mori, H. Ohkita, S. Ito, *J. Mater. Chem. A.* **2016,** *4*, 5340.

[18] M. Svensson, F. Zhang, S. C. Veenstra, W. J. H. Verhees, J. C. Hummelen, J. M. Kroon, O. Inganäs, M. R. Andersson, *Adv. Mater.* **2003**, *15*, 988.

[19] B. C. Thompson, J. M. J. Fréchet, *Angew. Chem. Int. Ed.* **2008**, *47*, 58.

[20] Y.-J. Cheng, S.-H. Yang, C.-S. Hsu, *Chem. Rev.* **2009**, *109*, 5868.

[21] G. Li, R. Zhu, Y. Yang, *Nat. Photonics* **2012**, *6*, 153.

[22] S. Subramaniyan, H. Xin, F. S. Kim, N. M. Murari, B. A. E. Courtright, S. A. Jenekhe, *Macromolecules* **2014**, *47*, 4199.

[23] C. Liu, K. Wang, X. Gong, A. J. Heeger, *Chem. Soc. Rev.* **2016**, *45*, 4825.

[24] Y. Li, L. Xue, H. Li, Z. Li, B. Xu, S. Wen, W. Tian, *Macromolecules* **2009**, *42*, 4491.

[25] Y. Li, Y. Chen, X. Liu, Z. Wang, X. Yang, Y. Tu, X. Zhu, *Macromolecules* **2011**, *44*, 6370.

[26] L. Lu, T. Zheng, Q. Wu, A. M. Schneider, D. Zhao, L. Yu, *Chem. Rev.* **2015**, *115*, 12666.

[27] R. Kroon, M. Lenes, J. C. Hummelen, P. W. M. Blom, B. de Boer, *Polym. Rev.*

2008, *48*, 531.

[28] K. Kranthiraja, K. Gunasekar, W. Cho, M. Song, Y. G. Park, J. Y. Lee, Y. Shin, I.-N. Kang, A. Kim, H. Kim, B. Kim, S.-H. Jin, *Macromolecules* **2014**, *47*, 7060.

[29] B. Carsten, J. M. Szarko, H. J. Son, W. Wang, L. Lu, F. He, B. S. Rolczynski, S. J. Lou, L. X. Chen, L. Yu, *J. Am. Chem. Soc.* **2011**, *133*, 20468.

[30] N. Blouin, A. Michaud, D. Gendron, S. Wakim, E. Blair, R. Neagu-Plesu, M. Belletête, G. Durocher, Y. Tao, M. Leclerc, *J. Am. Chem. Soc.* **2008**, *130*, 732.

[31] J. Hou, H.-Y. Chen, S. Zhang, G. Li, Y. Yang, *J. Am. Chem. Soc.* **2008**, *130*, 16144.

[32] Y. Huang, L. Huo, S. Zhang, X. Guo, C. C. Han, Y. Li, J. Hou, *Chem. Commun.* **2011**, *47*, 8904.

[33] Y. Wu, Z. Li, W. Ma, Y. Huang, L. Huo, X. Guo, M. Zhang, H. Ade, J. Hou, *Adv. Mater.* **2013**, *25*, 3449.

[34] J.-H. Kim, C. E. Song, B. Kim, I.-N. Kang, W. S. Shin, D.-H. Hwang, *Chem. Mater.* **2014**, *26*, 1234.

[35] R. Kroon, A. D. Z. Mendaza, S. Himmel-berger, J. Bergqvist, O. Bäcke, G. C. Faria, F. Gao, A. Obaid, W. Zhuang, D. Gedefaw, E. Olsson, O. Inganäs, A. Salleo, C. Müller, M. R. Andersson, *J. Am. Chem. Soc.* **2014**, *136*, 11578.

[36] M. Wang, H. Wang, T. Yokoyama, X. Liu, Y. Huang, Y. Zhang, T.-Q. Nguyen, S. Aramaki, G. C. Bazan, *J. Am. Chem. Soc.* **2014**, *136*, 12576.

[37] M. Saito, I. Osaka, Y. Suda, H. Yoshida, K. Takimiya, *Adv. Mater.* **2016**,

28, 6921.

[38] P. M. Beaujuge, W. Pisula, H. N. Tsao, S. Ellinger, K. Müllen, J. R. Reynolds, *J. Am. Chem. Soc.* **2009**, *131*, 7514.

[39] J. Subbiah, B. Purushothaman, M. Chen, T. S. Qin, M. Gao, D. Vak, F. H. Scholes, X. W. Chen, S. E. Watkins, G. J. Wilson, A. B. Holmes, W. W. H. Wong, D. J. Jones, *Adv. Mater.* **2015**, *27*, 702.

[40] P. Sonar, E. L. Williams, S. P. Singh, A. Dodabalapur, *J. Mater. Chem.* **2011**, *21*, 10532.

[41] E. G. Wang, L. Hou, Z. Wang, S. Hellström, F. L. Zhang, O. Inganäs, M. R. Andersson, *Adv. Mater.* **2010**, *22*, 5240.

[42] E. Zhou, J. Cong, K. Tajima, K. Hashimoto, *Chem. Mater.* **2010**, *22*, 4890.

[43] Y. Zhang, J. Zou, H.-L. Yip, K.-S. Chen, D. F. Zeigler, Y. Sun, A. K.-Y. Jen, *Chem. Mater.* **2011**, *23*, 2289.

[44] C. Piliego, T. W. Holcombe, J. D. Douglas, C. H. Woo, P. M. Beaujuge, J. M. J. Fréchet, *J. Am. Chem. Soc.* **2010**, *132*, 7595.

[45] Y. Zou, A. Najari, P. Berrouard, S. Beaupré, B. R. Aïch, Y. Tao, M. Leclerc, *J. Am. Chem. Soc.* **2010**, *132*, 5330.

[46] Y. Li, P. Sonar, L. Murphy, W. Hong, *Energy Environ. Sci.* **2013**, *6*, 1684.

[47] W. Li, K. H. Hendriks, M. M. Wienk, R. A. J. Janssen, *Acc. Chem. Res.* **2016**, *49*, 78.

[48] J. Cao, Q. Liao, X. Du, J. Chen, Z. Xiao, Q. Zuo, L. Ding, *Energy Environ.*

Sci. **2013**, *6*, 3224.

[49] J. Cao, L. Qian, F. Lu, J. Zhang, Y. Feng, X. Qiu, H.-L. Yip, L. Ding, *Chem*. *Commun*. **2015**, *51*, 11830.

[50] J. Cao, C. Zuo, B. Du, X. Qiu, L. Ding, *Chem*. *Commun*. **2015**, *51*, 12122.

[51] L. Qian, J. Cao, L. Ding, *J. Mater. Chem. A* **2015**, *3*, 24211.

[52] S. Subramaniyan, F. S. Kim, G. Ren, H. Li, S. A. Jenekhe, *Macromolecules* **2012**, *45*, 9029.

[53] H. Choi, S. J. Ko, T. Kim, P. O. Morin, B. Walker, B. H. Lee, M. Leclerc, J. Y. Kim, A. J. Heeger, *Adv. Mater.* **2015**, *27*, 3318.

[54] T. Ma, K. Jiang, S. Chen, H. Hu, H. Lin, Z. Li, J. Zhao, Y. Liu, Y.-M. Chang, C.-C. Hsiao, H. Yan, *Adv. Energy Mater.* **2015**, *5*, 1501282.

[55] R. Stalder, J. Mei, K. R. Graham, L. A. Estrada, J. R. Reynolds, *Chem. Mater.* **2014**, *26*, 664.

[56] P. Deng, Q. Zhang, *Polym. Chem.* **2014**, *5*, 3298.

[57] S. Lu, M. Drees, Y. Yao, D. Boudinet, H. Yan, H. Pan, J. Wang, Y. Li, H. Usta, A. Facchetti, *Macromolecules* **2013**, *46*, 3895.

[58] X. Guo, S. R. Puniredd, B. He, T. Marszalek, M. Baumgarten, W. Pisula, K. Müllen, *Chem. Mater.* **2014**, *26*, 3595.

[59] X. Guo, A. Facchetti, T. J. Marks, *Chem. Rev.* **2014**, *114*, 8943.

[60] B. Frydman, M. Los, H. Rapoport, *J. Org. Chem.* **1971**, *36*, 450.

[61] A. K. Mishra, S. Vaidyanathan, H. Noguchi, F. Doetz, Y. Guan, *PCT Int. Appl.*

WO 2012146574 A1, November 1, **2012**.

[62] L. Nanson, N. Blouin, W. Mitchell, S. Tierney, T. Cull, *PCT Int. Appl.* WO 2013182262 A1, December 12, **2013**.

[63] L. J. Huo, J. Hou, H.-Y. Chen, S. Q. Zhang, Y. Jiang, T. L. Chen, Y. Yang, *Macromolecules* **2009**, *42*, 6564.

[64] Q. Peng, Q. Huang, X. Hou, P. Chang, J. Xu, S. Deng, *Chem. Commun.* **2012**, *48*, 11452.

[65] J. W. Jung, J. W. Jo, F. Liu, T. P. Russell, W. H. Jo, *Chem. Commun.* **2012**, *48*, 6933.

[66] P. S. Hameed, V. Patil, S. Solapure, U. Sharma, P. Madhavapeddi, A. Raichurkar, M. Chinnapattu, P. Manjrekar, G. Shanbhag, J. Puttur, V. Shinde, S. Menasinakai, S. Rudrapatana, V. Achar, D. Awasthy, R. Nandishaiah, V. Humnabadkar, A. Ghosh, C. Narayan, V. K. Ramya, P. Kaur, S. Sharma, J. Werngren, S. Hoffner, V. Panduga, C. N. N. Kumar, J. Reddy, K. N. M. Kumar, S. Ganguly, S. Bharath, U. Bheemarao, K. Mukherjee, U. Arora, S. Gaonkar, M. Coulson, D. Waterson, V. K. Sambandamurthy, S. M. de Sousa, *J. Med. Chem.* **2014**, *57*, 4889.

[67] M. Hultell, S. Stafström, *Phys. Rev. B* **2007**, *75*, 104304.

[68] N. E. Jackson, B. M. Savoie, K. L. Kohlstedt, M. Olvera de la Cruz, G. C. Schatz, L. X. Chen, M. A. Ratner, *J. Am. Chem. Soc.* **2013**, *135*, 10475.

[69] H.-C. Liao, C.-C. Ho, C.-Y. Chang, M.-H. Jao, S. B. Darling, W.-F. Su, *Mater. Today* **2013**, *16*, 326.

[70] C. Li, Y. Chen, Y. Zhao, H. Wang, W. Zhang, Y. Li, X. Yang, C. Ma, L. Chen, X. Zhu, Y. Tu, *Nanoscale* **2013**, *5*, 9536.

[71] H. Yao, L. Ye, H. Zhang, S. Li, S. Zhang, J. Hou, *Chem. Rev.* **2016**, *116*, 7397.

[72] L. Murphy, B. Sun, W. Hong, H. Aziz, Y. Li, *Aust. J. Chem.* **2015**, *68*, 1741.

[73] M. S. Chen, J. R. Niskala, D. A. Unruh, C. K. Chu, O. P. Lee, J. M. J. Fréchet, *Chem. Mater.* **2013**, *25*, 4088.

[74] V. Vohra, K. Kawashima, T. Kakara, T. Koganezawa, I. Osaka, K. Takimiya, H. Murata, *Nat. Photonics* **2015**, *9*, 403.

[75] E. J. Zhou, S. P. Yamakawa, K. Tajima, C. H. Yang, K. Hashimoto, *Chem. Mater*. **2009**, *21*, 4055.

[76] T. Yamamoto, T. Ikai, M. Kuzuba, T. Kuwabara, K. Maeda, K. Takahashi, S. Kanoh, *Macromolecules* **2011**, *44*, 6659.

Chapter 4. Designing 1,5-Naphthyridine-2,6-dione-Based Conjugated Polymers for Higher Crystallinity and Enhanced Light Absorption to Achieve 9.63% Efficiency Polymer Solar Cells

4.1. Introduction

For over two decades, polymer solar cells (PSCs) with bulk heterojunction (BHJ) structures have attracted significant attention for use in large area devices because of their unique advantages such as easy fabrication, low cost, and light weight.[1-6] One of the most promising approaches for high-performance PSCs is the use of crystalline donor (D)-acceptor (A)-type low-bandgap polymers as active layers. There are distinct benefits of using crystalline polymers in PSC devices: (1) the polymers facilitate interchain charge transport via close packing of chains and π-π interactions, and (2) their high crystallinities enhance domain purity, which effectively minimizes bimolecular recombination.[7,8] Most PSCs that use D-A polymers have been optimized with a thin active layer (< 110 nm) since the fill factor (FF) decreases rapidly as the active layer thickness increases. The drastic FF degradation in thick active layers eventuates from low vertical charge mobility and insufficient light absorption.[9-11]

Crystalline polymers with sufficient light-absorbing capability enable the fabrication of PSC devices with thick active layers (> 200 nm), thus affording reproducible, pinhole-free large area devices.

To this end, efforts to produce thick-active-layer PSCs via the development of crystalline D-A polymers are underway. Early studies of thick-active-layer PSCs focused primarily on benzo[1,2-*b*:4,5-*b*']dithiophene (BDT)-containing polymers owing to its chemical and electronic tunability, which allowed substitution of the 2′ and 6′ positions with aliphatic or aromatic substituents. However, since most BDT-based polymers have insufficient polymer crystallinity and vertical hole mobility, only a few of them afford efficient PSCs with active layer thicknesses of over 200 nm.[12-15] In recent years, naphthobisthiadiazole (NTz) and benzothiadiazole (BT) derivatives have been considered as the most successful building blocks for efficient thick-layer PSCs owing to their strong electron-accepting ability and structural planarity.[16-19] For instance, the NTz-based D-A polymer PNTz4T, synthesized by Kawashima *et al*. exhibited a power conversion efficiency (PCE) of 10.1% with a thick active layer (≈290 nm).[20,21] Liu *et al*. designed a fluorinated BT (ffBT)-based polymer PffBT4T-2OD and achieved a PCE of 10.8% with a 300 nm-thick device, which represents the state-of-the-art for thick-film PSCs in single-cell devices.[22,23] Recently, Zhao *et al*. synthesized a crystalline donor polymer, PffBX4T-2DT, based on fluorinated benzoxadizole (ffBX). Its efficiency reached 9.4% with a thick (250 nm) active layer and it offered a higher open circuit voltage (V_{oc}) than PffBT4T-2OD-based cells.[24]

However, the thick-active-layer PSCs with NTz- or BT-based crystalline polymers exhibited high PCEs only after hot processing that produced aggregated morphologies and small domain sizes (30~40 nm).[25,26] Device performance varied with the solution and substrate processing temperatures, resulting in irregular π-π distances and varying domain sizes, which prevented mass production and device efficiency reproducibility. In addition, the absorption coefficients of NTz- and BT-based polymers are limited to less than 10^5 cm^{-1}, which can be unfavorable to increasing PSC photocurrents.

In fact, optical absorption is a crucial factor for efficient thick-active-layer PSCs; polymers with high absorption coefficients can harvest more solar photons, thus generating large quantities of photo-induced carriers, which lead to high short-circuit current densities (J_{sc}) and PCEs.[27,28] Moreover, sufficient light absorption can compensate for FF degradation in thick-active-layer PSCs by photo-generating large numbers of charge carriers. Therefore, it is important to design new crystalline polymers with process reproducibility and high absorption coefficients (*ca.* 10^5 cm^{-1}) via optimized integration of novel D and A building blocks.

I recently reported a new bis-lactam-based compound, 1,4-naphthyridine-2,6-dione (NTD) (**Figure 4-1**), as a promising A building block for the development of efficient D-A conjugated polymers.[29] Compared to thiophenyl-substituted DPP (DPPT), which has been widely used as the most efficient bis-lactam A unit, thiophenyl-substituted NTD (NTDT) exhibited a remarkably higher molar extinction coefficient and greater coplanar conformation owing to its intramolecular S···O interactions. Therefore, the

BHJ PSC device fabricated by using an NTDT-based conjugated polymer (P(NTDT-BDT)) with phenyl-C_{71}-butyric acid methyl ester ($PC_{71}BM$) exhibited better performance (8.16% PCE) than the DPPT-based conjugated polymer (P(DPPT-BDT)) device.[29] Although the performance of the first successful NTDT-based PSC example was promising, it operated best with a medium-thick active-layer (≈ 140 nm) due to insufficient polymer crystallinity. Therefore, its polymer crystallinity must be increased via backbone structure modification in order to produce more efficient (> 9% PCE) thick-active-layer (> 200 nm) PSCs.

Herein, I report newly synthesized NTDT-based D-A polymers (**Figure 4-1**), referred to as PNTDT-2T, PNTDT-TT, and PNTDT-2F2T with 2,2'-bithiophene (2T), thieno[3,2-*b*]thiophene (TT), and 3,3'-difluoro-2,2'-bithiophene (2F2T) D units, respectively. I examine the structure-property relationships with regard to polymer crystallinities and absorption coefficients. Since the D unit of P(NTDT-BDT), octyl-dodecyl substituted BDT, appeared unsuitable for achieving high polymer crystallinities, I adopted simpler and more compact D units, *i.e.*, 2T, TT, and 2F2T. Of the resulting NTDT-based polymers, PNTDT-2F2T exhibited an excellent PCE of 9.63% with outstanding polymer crystallinity and enhanced absorption coefficient. Interestingly, the PNTDT-2F2T-based devices were not sensitive to processing conditions and exhibited the best photovoltaic performances with an active layer thickness of over 200 nm.

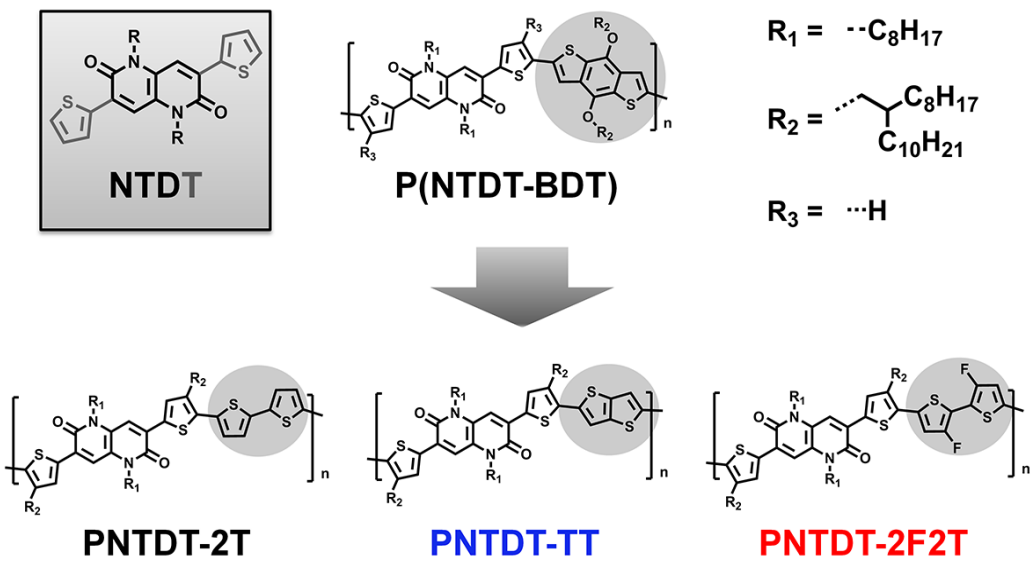

Figure 4-1. Chemical structures of NTDT, P(NTDT-BDT), and the target polymers (PNTDT-2T, PNTDT-TT, and PNTDT-2F2T).

4.2. Results and Discussion

4.2.1. Synthesis and characterization

The synthetic route used to produce the NTDT-based polymers (PNTDT-2T, PNTDT-TT, and PNTDT-2F2T) is depicted in **Scheme 4-1,** and the synthetic procedure is described in the Experimental section. Unlike our previously reported NTDT monomer (1,5-dioctyl-3,7-di(thiophen-2-yl)-1,5-naphthyridine-2,6-dione), I attached the additional octyl-dodecyl alkyl side chain to the NTDT thiophene group to ensure the polymer's solubility and processability. A series of new donor polymers (PNTDT-2T, PNTDT-TT, and PNTDT-2F2T) were synthesized via Stille coupling polymerization with NTDT as the A unit and 2T, TT, or 2F2T as the D units. The number-average molecular weight (M_n) and polydispersity index (PDI) of the donor polymers were measured via high-temperature gel permeation chromatography (GPC) at 90 °C with chloroform as the eluent and polystyrene as the standard. The M_n and PDI are, respectively, 33.8 kDa and 1.6 for PNTDT-2T, 84.6 kDa and 4.2 for PNTDT-TT, and 54.4 kDa and 28.5 for PNTDT-2F2T (**Figure 4-2**). The bimodal spectra and large PDI value of PNTDT-2F2T indicate strong aggregation, which suggests that the measured M_n value may represent that of aggregate. The thermal properties of the three polymers were evaluated via thermal gravimetric analysis (TGA) and differential

scanning calorimetry (DSC). As shown in **Figure 4-3**, the three polymers exhibit high thermal stabilities, with decomposition temperatures for 5% weight loss of approximately 419 °C for PNTDT-2T, 415 °C for PNTDT-TT, and 426 °C for PNTDT-2F2T. Thus, they are sufficiently stable for PSC device fabrication. The DSC results reveal distinct thermal transitions at 286/265 °C for PNTDT-2T and 325/296 °C for PNTDT-TT during the second heating/cooling scan (**Figure 4-4**). However, PNTDT-2F2T exhibits no obvious thermal transition below 350 °C during the second heating/cooling scan, which suggests restricted molecular motion during temperature changes and indicates that PNTDT-2F2T has a more rigid structure than the other two polymers.

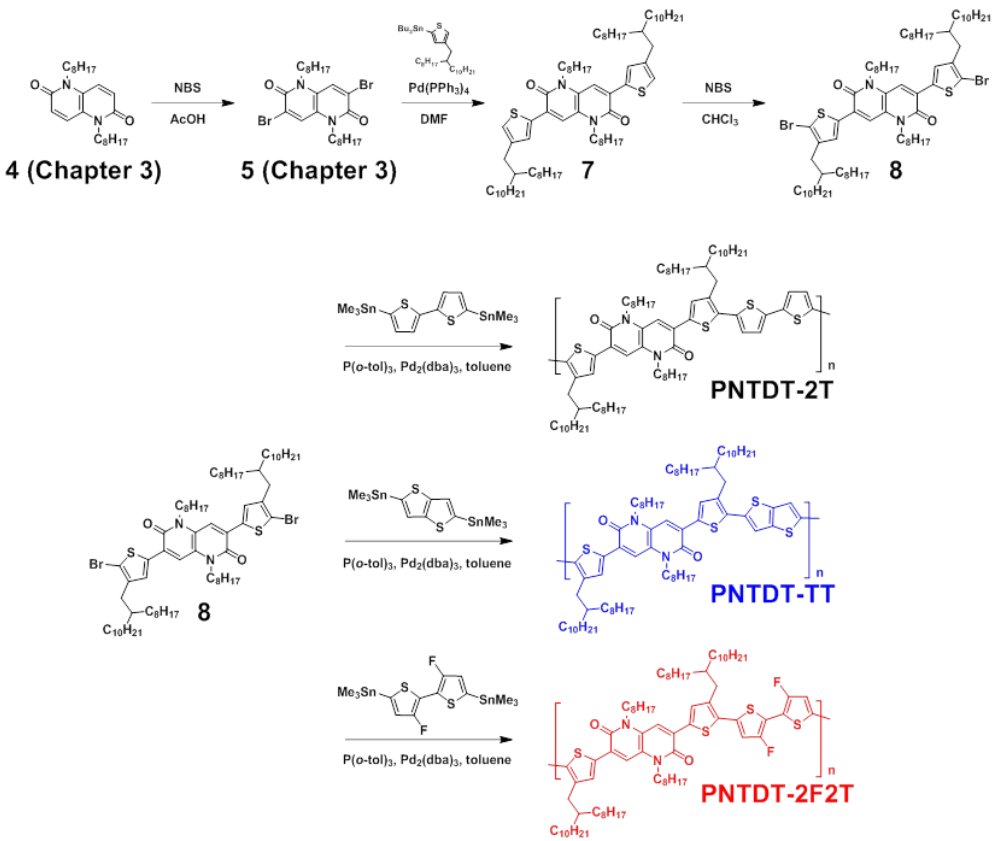

Scheme 4-1. Syntheses of PNTDT-2T, PNTDT-TT, and PNTDT-2F2T.

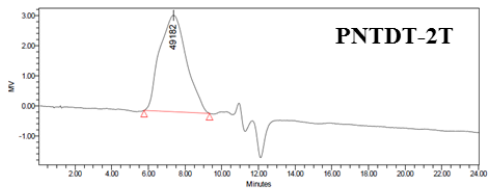

M_n	M_w	PDI
33853	54045	1.5964

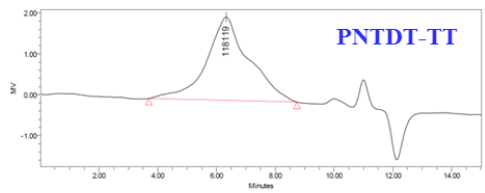

M_n	M_w	PDI
84637	351335	4.1510

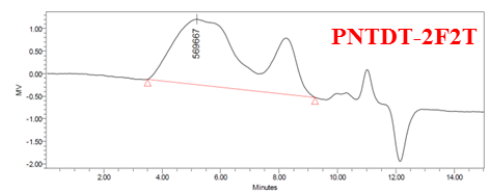

M_n	M_w	PDI
54384	159409	28.4902

Figure 4-2. GPC curves of (a) PNTDT-2T, (b) PNTDT-TT, and (c) PNTDT-2F2T.

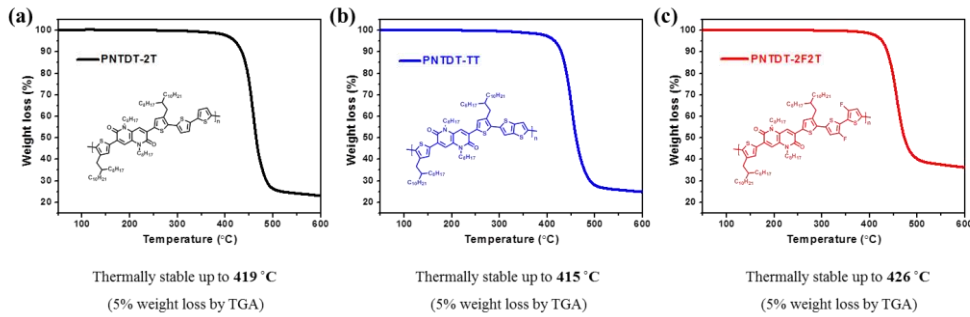

Figure 4-3. TGA curves of (a) PNTDT-2T, (b) PNTDT-TT, and (c) PNTDT-2F2T.

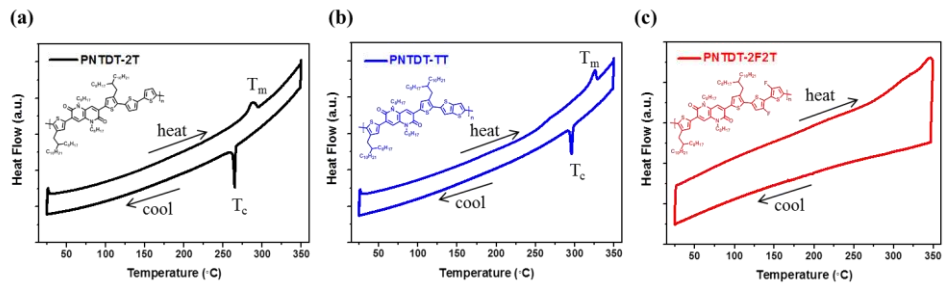

Figure 4-4. DSC curves of (a) PNTDT-2T, (b) PNTDT-TT, and (c) PNTDT-2F2T.

4.2.2. Theoretical calculations

Theoretical quantum chemical density functional theory (DFT) calculations were performed to analyze the molecular structures and optimized geometries of the three polymers using Gaussian 09 at the B3LYP level with 6-31G as the basis set. The alkyl groups of the three polymers were simplified to methyl groups to reduce the cost of calculation. The torsion angles in the three NTDT-based polymers are shown in **Figure 4-5**. As expected, the NTDT core has an almost planar structure (θ_1<1°) owing to intramolecular, non-bonding S···O interactions. In addition, the insertion of a fluorine atom in the 2T unit reduced the torsion angles (θ_3 = 0.12° for PNTDT-2F2T and θ_3 = 9.88° for PNTDT-2T) via intramolecular, non-bonding S···F interactions, as reported with other 2F2T-containing polymers.[30,31] This result explains the planar structure of PNTDT-2F2T, as shown in the side view (**Figure 4-5**b). In addition, PNTDT-2F2T exhibits a smaller torsion angle between NTDT and the D unit (θ_2 = 7.38°) than PNTDT-2T (θ_2 = 15.61°) or PNTDT-TT (θ_2 = 19.67°). Therefore, PNTDT-2F2T possesses the most rigid backbone structure. Since the crystallinities of conjugated polymers are significantly affected by their backbone curvatures, these three polymers are expected to show markedly different crystallinities.[32-35] As shown in **Figure 4-5**c, the HOMO electrons of the three polymers are delocalized over the polymer backbone, whilst the LUMO electrons are localized on the NTDT unit, indicating that NTDT is a

strong electron acceptor due to the lactam group in its structure. The calculated HOMO/LUMO energies of the polymers are -4.56/-2.79 eV (PNTDT-2T), -4.63/-2.80 eV (PNTDT-TT), and -4.66/-2.91 eV (PNTDT-2F2T), respectively.

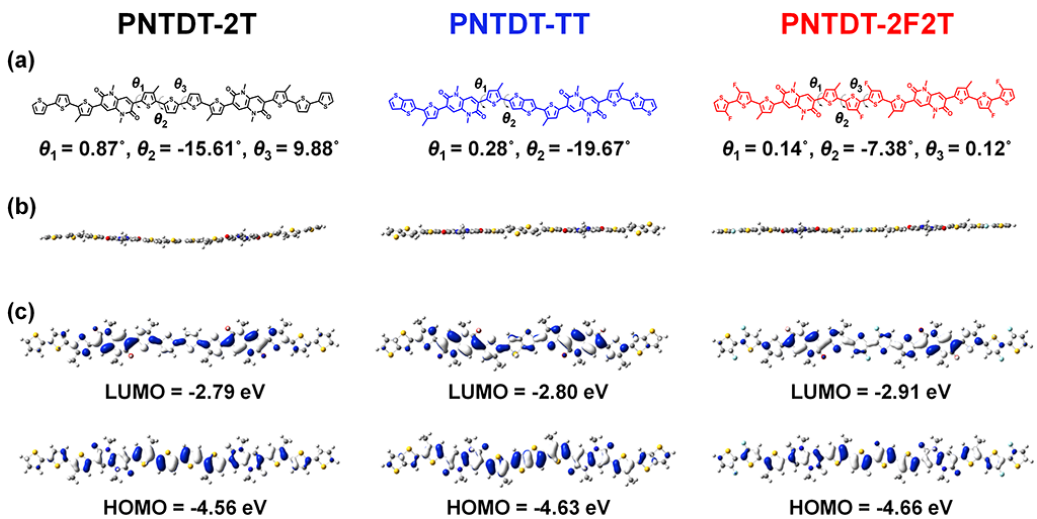

Figure 4-5. (a) Molecular structures, (b) side views of optimized geometries, and (c) HOMO and LUMO level distributions of the model compounds for PNTDT-2T, PNTDT-TT, and PNTDT-2F2T, as determined via DFT calculations performed using Gaussian 09.

4.2.3. Optical and electrochemical properties

The normalized UV-vis absorption spectra of the NTDT-based polymers in chloroform solution and of the thin films are displayed in **Figure 4-6**. The lowest energy transitions in the PNTDT-2T and PNTDT-TT thin films are significantly red-shifted (52 nm and 48 nm, respectively) relative to the solution state. In the case of PNTDT-2F2T, there is barely any shift, implying a certain degree of intermolecular packing even in solution, probably due to its rigid, planar backbone structure.[36,37] In addition, PNTDT-2F2T exhibits distinct, sharp 0-0 (λ = 729 nm) and 0-1 (λ = 662 nm) vibronic peaks, revealing a more ordered microstructure, which is attributable to the coplanar backbones predicted via DFT.[38] Interestingly, the absorption coefficient of PNTDT-2F2T increases significantly to 160,000 cm^{-1} at the maximum absorption peak, which is much higher than with PNTDT-2T (61,600 cm^{-1}) or PNTDT-TT (93,000 cm^{-1}) (**Figure 4-6**c). It is worth noting that the greater rigidity of the PNTDT-2F2T backbone can enhance its light harvesting capability, consequently rendering it more efficient at harvesting photons and generating photocurrents than PNTDT-2T or PNTDT-TT.[39]

The HOMO energy levels of the three polymers were estimated via cyclic voltammetry (CV) of the solid-state films (spin-coated on indium tin oxide (ITO) substrates), as shown in **Figure 4-7**. The respective HOMO energy levels of PNTDT-2T, PNTDT-TT, and PNTDT-2F2T are -5.07, -5.10, and -5.20 eV. As expected,

PNTDT-2F2T has a deeper HOMO energy level than the other polymers due to the effect of the electron-withdrawing fluorine atom, which renders it more able to produce high open-circuit voltages (V_{oc}) in the PSCs.[40] I also estimated the LUMO energy levels of the polymers by subtracting the absorption onsets (optical band gaps) from the corresponding HOMO energy levels, as depicted in **Figure 4-6**d. The experimentally determined polymer HOMO/LUMO energy levels coincided well with the computed results.

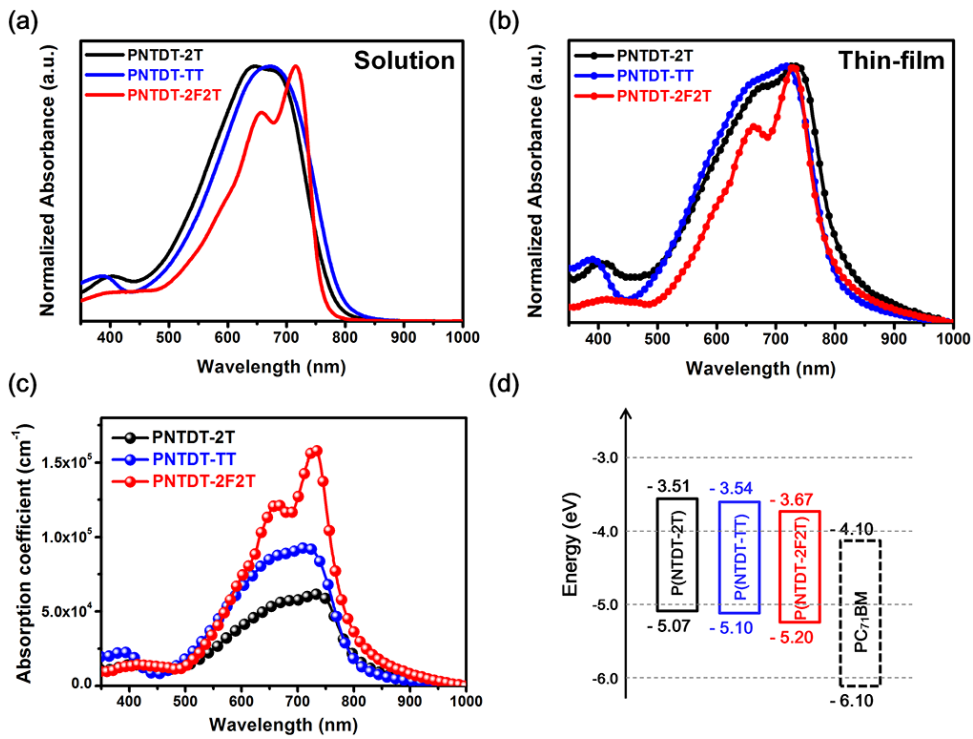

Figure 4-6. Normalized absorption spectra of the three polymers in (a) $CHCl_3$ solution and (b) thin films. (c) Absorption coefficients of the three polymers in thin films. (d) Energy level diagrams of the polymers and $PC_{71}BM$.

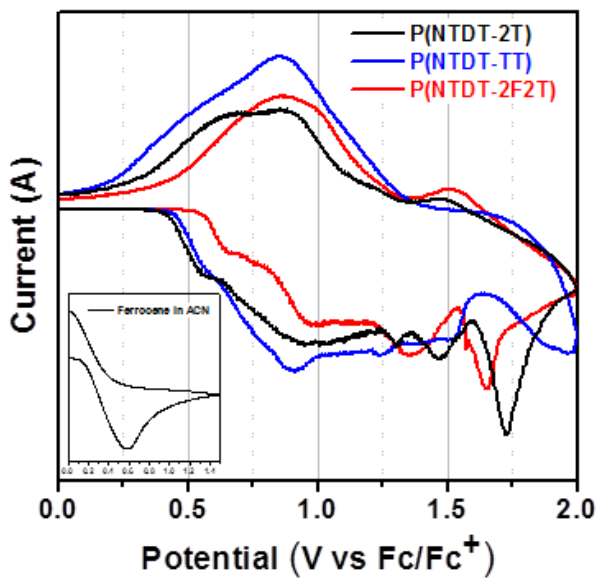

Figure 4-7. Cyclic voltammetry curves of the three polymers in thin film state (inset: CV of ferrocene shown for comparison).

4.2.4. Photovoltaic properties

Bulk-heterojunction PSCs were fabricated using $PC_{71}BM$ as the acceptor in a conventional ITO/PEDOT:PSS/Polymer:$PC_{71}BM$/Ca/Al device structure. The current density–voltage (*J*–*V*) curves and incident photon-to-current efficiencies (IPCEs) of the best cells are shown in **Figure 4-8**, and the relevant photovoltaic performance data is summarized in **Table 4-2**. The PCEs of the best devices based on PNTDT-2T, PNTDT-TT, and PNTDT-2F2T increase to 6.20%, 6.92%, and 9.63%, respectively. As expected, PNTDT-2F2T-based devices exhibit the highest V_{oc} values (0.73 V for PNTDT-2F2T and 0.66 V for both PNTDT-2T and PNTDT-TT) due to their low HOMO energy levels. In addition, the PNTDT-2F2T-based device exhibits a higher J_{sc} than PNTDT-2T or PNTDT-TT (18.80 mA/cm^2, 13.67 mA/cm^2, and 16.54 mA/cm^2 respectively), which can be attributed to its higher backbone planarity and light absorptivity.

The relationship between the active layer film thickness and the device properties was examined by varying the thickness via manipulation of the solution concentration. **Figure 4-9**, **Table 4-3**, and **Figure 4-8**c show the *J*–*V* curves and PCE values of PSC devices with various active layer thicknesses. The PNTDT-TT:$PC_{71}BM$ device with a thin active layer (90~100 nm) exhibits a superior J_{sc} (16.30 mA cm^{-2}) and average PCE (6.67%) when compared to the PNTDT-2T:$PC_{71}BM$ device (J_{sc} = 13.24 mA cm^{-2},

average PCE = 5.99%), probably because of the higher PNTDT-TT absorption coefficient discussed in the previous section. As the film thickness increases, the average PCE of the PNTDT-2T:$PC_{71}BM$ device decreases from 5.99% at 100 nm to 5.58%, 5.36%, and 4.79% at 130 nm, 155 nm, and 220 nm, respectively, while that of PNTDT-TT:$PC_{71}BM$ decreases more significantly to 4.64%, 3.75%, and 2.90% at 130 nm, 190 nm, and 250 nm, respectively. PNTDT-2T and PNTDT-TT exhibit 20.3% and 44.8% PCE reductions relative to their initial performances, at thicknesses of 220 nm and 190 nm, respectively. This is because of decreases in J_{sc} and FF. In the case of PNTDT-2F2T:$PC_{71}BM$ device, however, J_{sc} increases continuously while the FF is maintained when the film thickness increases up to 210 nm. Thus, the highest PNTDT-2F2T:$PC_{71}BM$ device PCE (9.63%) is obtained with an active layer thickness of over 200 nm without a hot solution or pre-heated substrate. The different trends exhibited by the three NTDT-based polymers may be closely related to not only their optical properties but also the degree of polymer crystallinity, which is discussed in the following section.

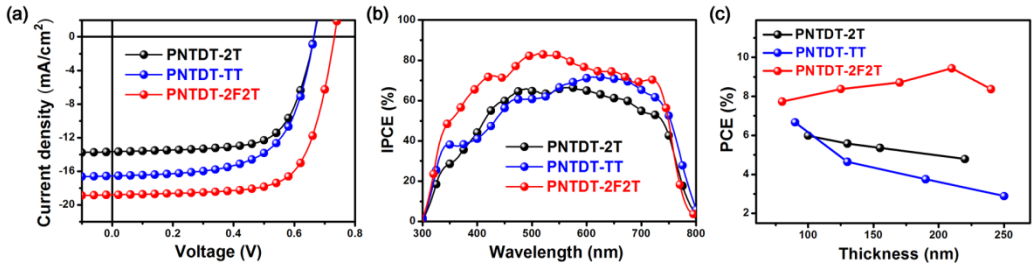

Figure 4-8. (a) Current density-voltage (*J*–*V*) curves and (b) IPCE spectra of the best polymer/$PC_{71}BM$ photovoltaic devices. (c) Thickness dependence of the PCEs of the polymer/$PC_{71}BM$ photovoltaic devices.

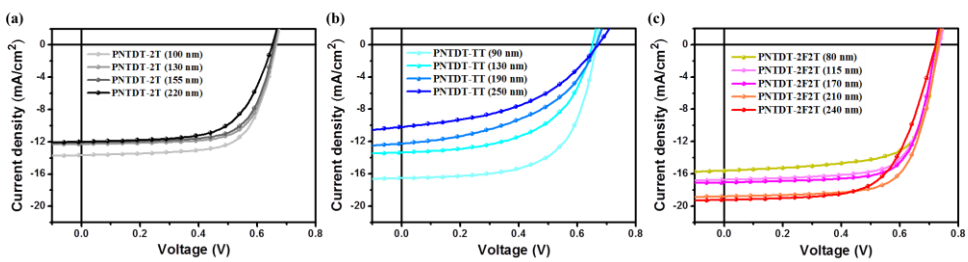

Figure 4-9. *J*–*V* curves of the (a) PNTDT-2T:$PC_{71}BM$, (b) PNTDT-TT:$PC_{71}BM$, and (c) PNTDT-2F2T:$PC_{71}BM$ PSCs with active layer thickness variation.

Table 4-1. Photovoltaic parameters of the optimized PNTDT-2T:$PC_{71}BM$, PNTDT-TT:$PC_{71}BM$, and PNTDT-2F2T: $PC_{71}BM$ devices.[a)]

Polymer[b)]	V_{oc} [c)] [V]	J_{sc} [c)] [mA cm^{-2}]	FF [c)]	PCE[c)] [%]	Thickness [nm]
PNTDT-2T	0.66	13.67	0.69	6.20 (5.99 ± 0.15)	100 ± 8
PNTDT-TT	0.66	16.54	0.63	6.92 (6.67 ± 0.18)	90 ± 10
PNTDT-2F2T	0.73	18.80	0.70	9.63 (9.44 ± 0.08)	210 ± 7

[a)]ITO/PEDOT:PSS/polymer:$PC_{71}BM$/Ca/Al; [b)]Polymer:$PC_{71}BM$ weight ratio is 1:1.5; [c)]Average values in parentheses were obtained from 8 devices.

Table 4-2. Photovoltaic parameters of polymer:$PC_{71}BM$ (1:1.5 w/w) BHJ devices[a)] as the active layer thickness increases.

Polymer	Thickness [nm]	V_{oc} [V]	J_{sc} [mA cm^{-2}]	FF	PCE (PCE_{max}) [%]
PNTDT-2T[b)]	100	0.67 ± 0.01	13.24 ± 0.26	0.68 ± 0.01	5.99 ± 0.15 (6.20)
	130	0.66 ± 0.01	12.24 ± 0.16	0.69 ± 0.01	5.58 ± 0.07 (5.68)
	155	0.66 ± 0.01	11.87 ± 0.26	0.69 ± 0.01	5.36 ± 0.08 (5.47)
	220	0.65 ± 0.01	11.35 ± 0.38	0.65 ± 0.01	4.79 ± 0.09 (4.94)
PNTDT-TT[b)]	90	0.66 ± 0.01	16.30 ± 0.35	0.62 ± 0.01	6.67 ± 0.18 (6.92)
	130	0.65 ± 0.01	13.18 ± 0.26	0.54 ± 0.01	4.64 ± 0.18 (4.81)
	190	0.66 ± 0.01	11.97 ± 0.22	0.47 ± 0.01	3.75 ± 0.06 (3.82)
	250	0.66 ± 0.01	9.73 ± 0.36	0.44 ± 0.01	2.90 ± 0.12 (3.07)
PNTDT-2F2T[b)]	80	0.73 ± 0.01	15.52 ± 0.15	0.69 ± 0.01	7.74 ± 0.13 (7.89)
	115	0.74 ± 0.01	16.35 ± 0.40	0.69 ± 0.01	8.38 ± 0.15 (8.54)
	170	0.73 ± 0.01	16.82 ± 0.19	0.71 ± 0.01	8.71 ± 0.05 (8.80)
	210	0.73 ± 0.01	18.38 ± 0.33	0.70 ± 0.01	9.44 ± 0.08 (9.63)
	240	0.72 ± 0.01	18.86 ± 0.46	0.62 ± 0.02	8.37 ± 0.40 (8.79)

[a)]ITO/PEDOT:PSS/polymer:$PC_{71}BM$/Ca/Al; [b)]Average values were obtained from over 5 devices.

4.2.5. Film morphologies and polymer crystallinities

I measured the grazing incidence wide-angle X-ray scattering (GIWAXS) patterns of the polymers to examine the relationships between their crystallinities and performances. **Figure 4-10** and **Figure 4-11** show GIWAXS images along with the out-of-plane (q_z direction) and in-plane (q_{xy} direction) profiles of the pristine polymers and the polymer:$PC_{71}BM$ blend films with and without diphenyl ether (DPE). Measured structure parameters are listed in **Table 4-4**. In the pristine films, PNTDT-2T and PNTDT-TT exhibit distinct (010) diffraction peaks with weak (*h*00) diffraction peaks in the out-of-plane direction, indicating that most of the polymers adopt a face-on orientation on the substrate. PNTDT-2F2T gave rise to strong (010) and (*h*00) diffraction peaks in the out-of-plane direction with a smaller π-π stacking distance (3.61 Å at q_z = 1.74 $Å^{-1}$) than those of PNTDT-2T (3.83 Å at q_z = 1.64 $Å^{-1}$) and PNTDT-TT (3.81 Å at q_z = 1.65 $Å^{-1}$), indicating that PNTDT-2F2T has a dense, close-packed crystalline domain. Upon blending with $PC_{71}BM$, molecular ordering of the polymers was extensively disrupted, as indicated by the broad, weak blend diffraction peaks. The (*h*00) diffraction peaks in the out-of-plane direction disappear for PNTDT-2T and PNTDT-TT, while PNTDT-2F2T has a weak π-π stacking peak in the out-of-plane direction after blending with $PC_{71}BM$. After the addition of DPE, an (*h*00) reflection appears along the out-of-plane directions of the PNTDT-2T/$PC_{71}BM$ and

PNDT-TT/$PC_{71}BM$ blends. I also observe further reductions in the π-π stacking distances of PNTDT-2T/$PC_{71}BM$ and PNTDT-TT/$PC_{71}BM$ blend films, suggesting that DPE may induce intense inter-chain organization.[41,42] The diffraction patterns of the PNTDT-2F2T/$PC_{71}BM$ blends reveal dramatic orientation changes, from edge-on to face-on orientation, after DPE addition, which is beneficial for vertical charge transport.[43,44] In addition, the crystalline coherence length (CCL) of the three polymers were calculated from the GIWAXS images of both the pristine and blend films using the Scherrer equation, to evaluate polymer crystallinity. In the pristine films, PNTDT-2F2T exhibits the highest CCL (29.8 Å) in the π-π stacking direction (PNTDT-2T: 28.3 Å; PNTDT-TT: 15.4 Å). This trend is also exhibited by the blends: PNTDT-TT (18.3 Å) < PNTDT-2T (24.6 Å) < PNTDT-2F2T (31.9 Å). These results indicate that PNTDT-2F2T forms a highly crystalline structure in the blended film with face-on-oriented crystallites, thus improving vertical hole transport and J_{sc} and FF, even in thick-active-layer PSC devices. However, PNTDT-TT exhibits the lowest crystallinity, which implies that the PCE of the PNTDT-TT-based PSC would decrease significantly as the active layer thickness increases, as discussed in Section 4.2.4. I further measured the vertical carrier mobilities of the three optimized polymer:$PC_{71}BM$ blend films to reveal the relationships between polymer crystallinity and charge transport (**Figure 4-12**). From the SCLC measurements, the vertical hole (μ_h) and electron mobilities (μ_e) of PNTDT-2F2T:$PC_{71}BM$ were calculated to be 8.6 x 10^{-3} cm^{-2} V^{-1} s^{-1} and 2.7 x 10^{-3} cm^{-2} V^{-1} s^{-1}, respectively. These exceed those of PNTDT-

2T:$PC_{71}BM$ (μ_h = 1.9 x 10^{-3} cm^{-2} V^{-1} s^{-1}; μ_e = 4.1 x 10^{-4} cm^{-2} V^{-1} s^{-1}) and PNTDT-TT:$PC_{71}BM$ (μ_h = 8.8 x 10^{-4} cm^{-2} V^{-1} s^{-1}; μ_e = 1.3 x 10^{-4} cm^{-2} V^{-1} s^{-1}). The highest carrier mobility of PNTDT-2F2T is consistent with its rigid structure and high crystallinity, as observed from the computational results and GIWAXS measurements.

Finally, I studied the morphologies of the three polymers. I used a transmission electron microscope (TEM) to examine the relationships between the photovoltaic properties and film morphologies of the polymer blend films. The TEM images (**Figure 4-13**) show that the PNTDT-2T:$PC_{71}BM$ and PNTDT-2F2T:$PC_{71}BM$ blend films exhibit more ordered, crystalline structures than the PNTDT-TT:$PC_{71}BM$ blend film because of highly ordered polymer packing. Moreover, the PNTDT-2F2T:$PC_{71}BM$ blend film contains finely dispersed, narrower (≈ 12 ± 5 nm) needle-shaped fibrils than the PNTDT-2T:$PC_{71}BM$ blend film, which has somewhat thicker fibrils (≈ 25 ± 4 nm). It is widely believed that the exciton diffusion length of a typical conjugated polymer is ~10 nm. Thus, I can conclude that the narrow nano-fibrils of PNTDT-2F2T are beneficial for exciton dissociation and charge transport, which lead to high SCLC mobility and J_{sc}.[45,46]

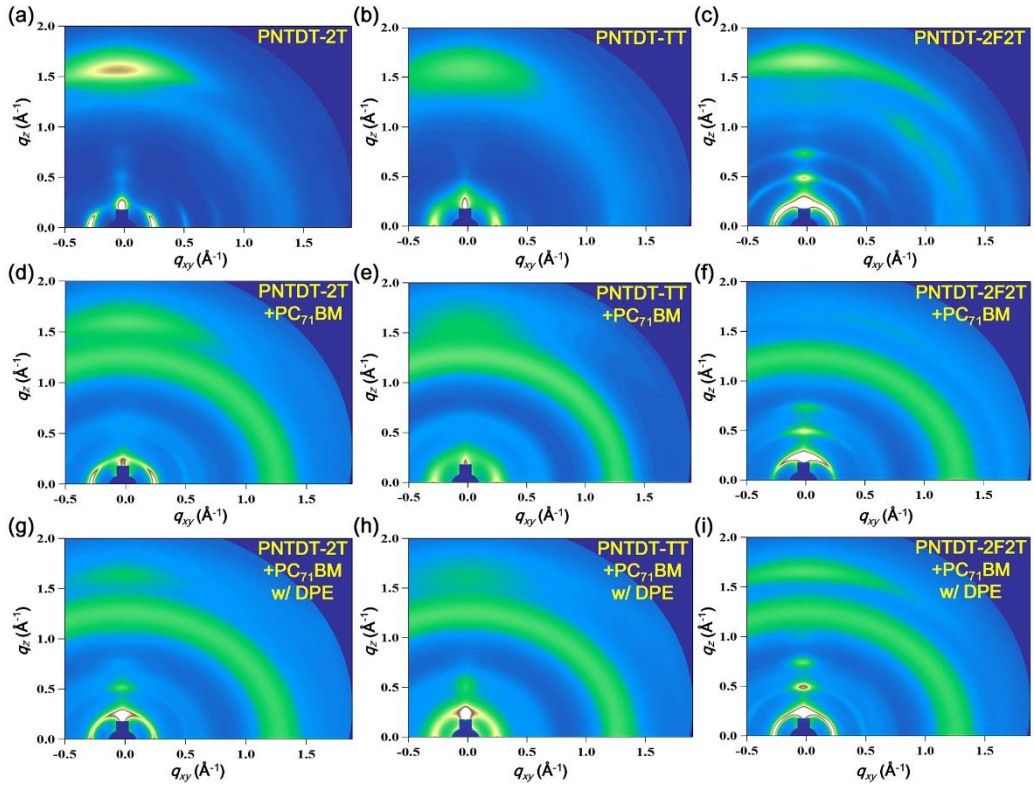

Figure 4-10. GIWAXS images of (top panel: a,b,c) pristine polymers, (middle panel: d,e,f) polymer:$PC_{71}BM$ blend films, and (bottom panel: g,h,i) polymer:$PC_{71}BM$ blend films with DPE.

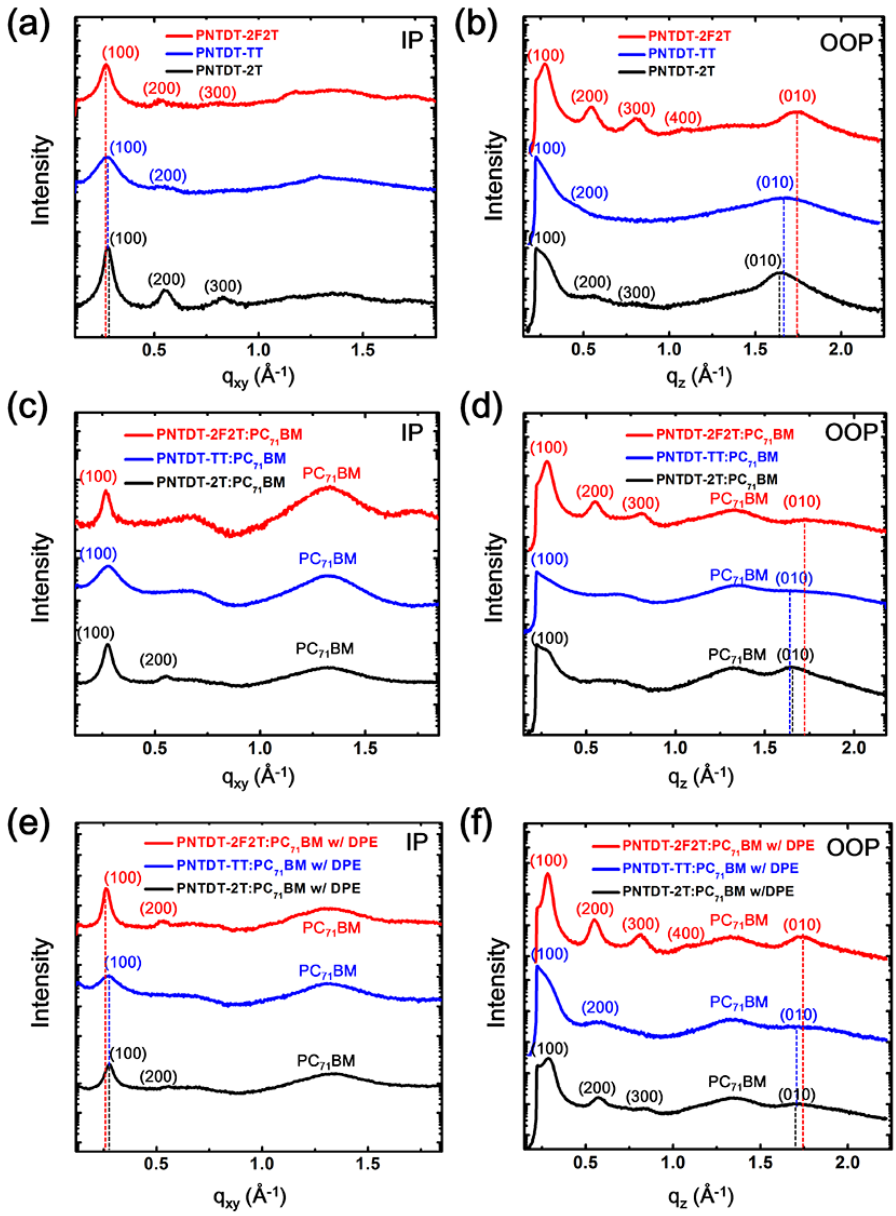

Figure 4-11. In-plane and out-of-plane linecuts of the GIWAXS patterns of (a–b) pristine polymer films, (c–d) polymer:$PC_{71}BM$ blend films, and (e–f) polymer:$PC_{71}BM$ blend films with DPE.

Table 4-3. GIWAXS parameters of the polymer thin films.

Film	Polymer	Lamella spacing		π-π stack		Coherence length	
		q_{xy} (Å^{-1})	*d-spacing* (Å)	q_z (Å^{-1})	*d-spacing* (Å)	FWHM (Å^{-1})	CCL (Å)
Pristine polymer	**PNTDT-2T**	0.2764	**22.7**	1.6421	**3.83**	0.2224	**28.3**
	PNTDT-TT	0.2744	**22.9**	1.6505	**3.81**	0.4083	**15.4**
	PNTDT-2F2T	0.2686	**23.4**	1.7417	**3.61**	0.2112	**29.8**
Polymer:$PC_{71}BM$ blend	**PNTDT-2T**	0.2764	**22.7**	1.6672	**3.76**	0.2754	**22.8**
	PNTDT-TT	0.2763	**22.7**	1.6506	**3.81**	0.3583	**17.5**
	PNTDT-2F2T	0.2691	**23.4**	1.7407	**3.61**	0.3140	**20.0**
Polymer:$PC_{71}BM$ w/DPE blend	**PNTDT-2T**	0.2783	**22.6**	1.7023	**3.69**	0.2556	**24.6**
	PNTDT-TT	0.2743	**22.9**	1.7124	**3.66**	0.3443	**18.3**
	PNTDT-2F2T	0.2678	**23.5**	1.7404	**3.61**	0.1967	**31.9**

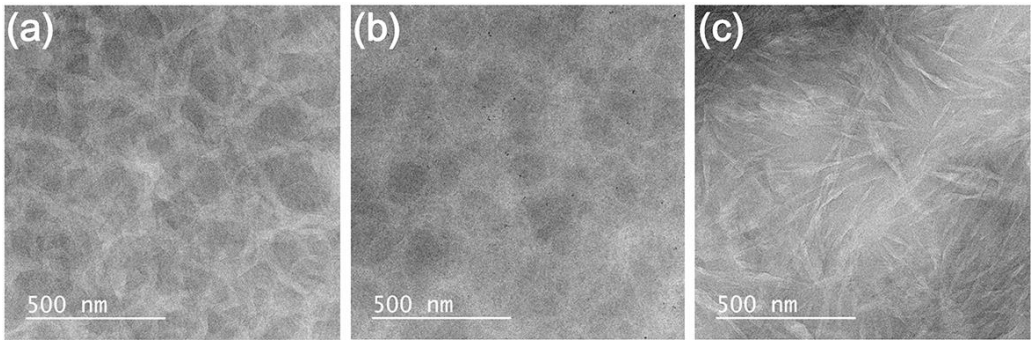

Figure 4-12. TEM images of the optimized (a) PNTDT-2T:$PC_{71}BM$, (b) PNTDT-TT:$PC_{71}BM$, and (c) PNTDT-2F2T:$PC_{71}BM$ blend films prepared from $CHCl_3$ with 2 vol% DPE.

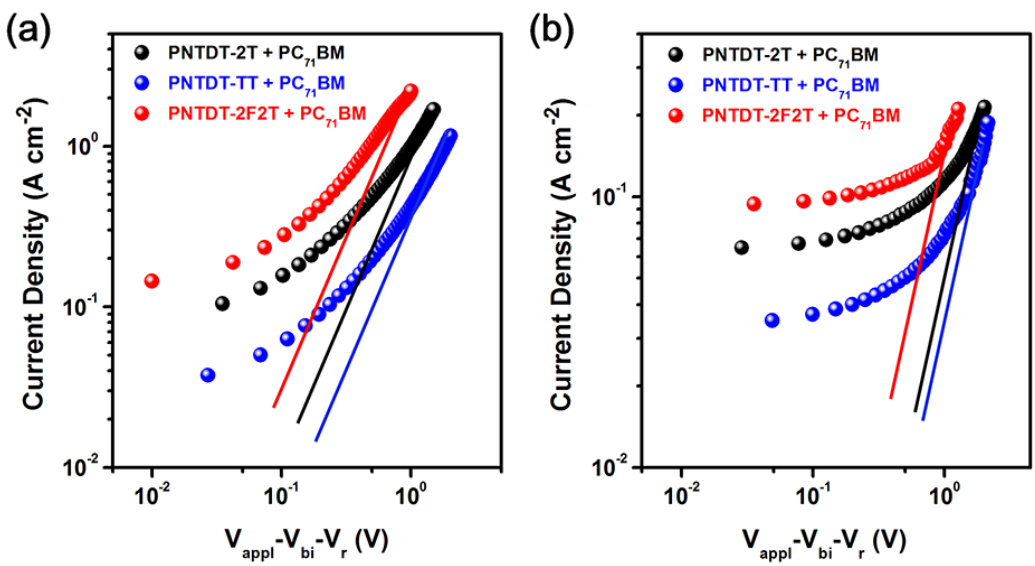

Figure 4-13. *J–V* curves of the (a) hole-only and (b) electron-only PNTDT-2T:$PC_{71}BM$, PNTDT-TT:$PC_{71}BM$, and PNTDT-2F2T:$PC_{71}BM$ devices.

4.3. Experimental

Materials and Characterization: All commercially available reagents were purchased from Sigma Aldrich Chemical Co., Tokyo Chemical Industry Co., or Alfa Aesar Co., and were used without further purification. 1,5-dioctyl-1,5-dihydro-1,5-naphthyridine-2,6-dione (1) and tributyl(4-(2-octyldodecyl)thiophene-2-yl)stannane were prepared following previously reported in the literature.[47] The donor units were purchased from Sigma Aldrich Chemical Co. (5,5'-bis(trimethylstannyl)-2,2'-bithiophene and 2,5-bis(trimethylstannyl)thieno[3,2-b]thiophene) and Sunatech Co. ((3,3'-difluoro-[2,2'-bithiophene]-5,5'-diyl)bis(trimethylstannane)), and were used after recrystallization for increasing purity. Chemical structures were fully identified via ^{1}H NMR (Bruker, Avance-300 and JEOL, JNM-LA400), ^{13}C NMR (Bruker, Avance-500), HR-ESI mass spectrometry (Waters, SYNAPT G2), and elemental analysis (CE Instrument, EA1110). The thermal properties of the compounds were obtained using thermogravimetric analysis (TGA) and differential scanning calorimetry (DSC) under N_2, with TA instruments Q50 and DSC-Q1000 tools, respectively. UV-Vis absorption spectra were recorded on a SHIMADZU UV-1650PC spectrometer. The cyclic voltammetry experiments were carried out using a Princeton Applied Research Potentiostat/Galvanostat Model 273A (Princeton Applied Research) onto which a three electrode cell assembly including an ITO-coated glass working electrode, a platinum

wire counter electrode, and a silver wire quasi-reference electrode was configured. The HOMO levels were estimated based on the onset oxidation potentials (E_{ox}), and E_{ox} was calibrated using ferrocene ($E_{Fc/Fc+}$) as a reference (Energy level = $-[E_{ox} - E_{Fc/Fc+} + 4.8]$). The film thickness was measured using a KLA Tencor Alpha-Step IQ surface profiler. The GIWAXS measurements were taken at the PLS-II 9A U-SAXS beamline (X-ray E = 11.06 keV, λ= 1.121 Å) of the Pohang Accelerator Laboratory in Korea. TEM images were obtained using a FEI Tecnai F20 operating at 200 kV. The TEM samples were prepared as follows. The polymer:$PC_{71}BM$ blend solutions were spin-coated onto PEDOT:PSS-coated glass. After drying, the films were floated off into distilled water, collected on a copper grid, and dried under a vacuum.

Device fabrication and Evaluation

OPV device fabrication and measurements

The patterned indium tin oxide (ITO) glass substrates were cleaned in an ultrasonic bath with deionized water, acetone, and isopropanol, and then exposed to a UV-ozone clean for 30 min. For the conventional devices, a PEDOT:PSS (Clavious P VP AI 4083) was spin-coated onto the ITO glass substrate at 5000 rpm for 30 s (30 nm) and dried on a hot plate at 150℃ for 10 min. The blend solutions of polymers and $PC_{71}BM$ (1:1.5 weight ratio) in $CHCl_3$/DPE additive (98:2 v/v) were fully dissolved at 40℃ overnight before use. The blend solutions were deposited through spin casting onto the PEDOT:PSS coated ITO glass in a N_2 glovebox. After drying the films for 1 hour in a

N_2 glovebox, a 5 nm layer of Ca and a 100 nm layer of Al were deposited by thermal evaporation under a vacuum of 10^{-6} Torr. The current density-voltage (*J*–*V*) characteristics of the solar cells were measured using a Keithley 4200 source measurement unit. The solar cell performances were characterized under AM 1.5G condition with an illumination intensity of 100 mW cm^{-2}, as generated using an Oriel Sol3A solar simulator (Oriel model 94023A). The measurements were carried out through a shadow mask with well-defined aperture area of 0.04 cm^2 under an ambient atmosphere. The incident photon-to-current efficiency (IPCE) was measured using an Oriel QE/IPCE Measurement Kit composed of a 300 W xenon lamp, a monochromator (74125), an order sorting filter wheel, a Merlin lock-in amplifier (70104), a calibrated silicon photodiode and an optical chopper.

Mobility measurements (SCLC)

The hole and electron mobilities were measured using the SCLC model, using a device configuration of ITO/PEDOT:PSS/polymer:$PC_{71}BM$/MoO_3/Ag and ITO/ZnO/polymer:$PC_{71}BM$/Ca/Al, for the hole-only and electron-only devices, respectively. Active layer conditions were identical to those used to fabricate the best performed photovoltaic devices. The SCLC mobilities were calculated using the following Mott-Gurney law:

$$J = \frac{9}{8}\varepsilon_r\varepsilon_0\mu_0\frac{V^2}{L^3}$$

where J is the current density, ε_r is the dielectric constant of the polymer (dielectric constant assumed to be 3), ε_0 is the permittivity of free space, μ_0 is the zero-field hole mobility, L is the polymer thickness, and the effective voltage, $V = V_{appl} - V_{bi} - V_r$, where V_{appl} is the applied voltage to the device, V_{bi} is the built-in voltage, and V_r is the voltage drop. The J–V curves of the devices were measured using a Keithley 4200 source measurement unit.

Synthesis of 3,7-dibromo-1,5-dioctyl-1,5-naphthyridine-2,6-dione (5): In a two-necked 100 mL round-bottom flask, compound (4) (5.00 g, 12.93 mmol) was dissolved in acetic acid (250 mL), and the solution was stirred at 0℃. To this solution was added *N*-bromosuccinimide (NBS) (6.22g, 34.92 mmol), and the solution was heated to 90℃ and stirred overnight. After the reaction had gone to completion, the solution was cooled to room temperature, poured into water, and the product was extracted by $CHCl_3$. The solvent was removing by rotary evaporation, and the crude product was purified by column chromatography (MC/MeOH, 99:1 v/v) to give an orange solid. Yield: 69.59% (4.90 g). ^{1}H NMR (300 MHz, $CDCl_3$, δ): 7.95 (s, 2H), 4.26 (t, J = 8.4 Hz, 4H), 1.72 (m, 4H), 1.49–1.21 (m, 24H), 0.89 (t, J = 6.9 Hz, 6H). ^{13}C NMR (500 MHz, $CDCl_3$, δ): 155.92, 129.82, 125.57, 122.36, 45.30, 31.95, 29.33, 29.31, 28.51, 26.94, 22.82, 14.29. Anal. calcd for $C_{24}H_{36}Br_2N_2O_2$: C 52.95, H 6.67, N 5.15; found: C 53.12, H 6.63, N 5.16. HRMS (ESI, m/z): $[M + H]^+$ calcd for $C_{24}H_{37}Br_2N_2O_2$ 543.1222; Found 543.1222.

Synthesis of 3,7-bis(4-(2-octyldodecyl)thiophen-2-yl)-1,5-dioctyl-1,5-naphthyridine-2,6-dione (7): In a two-necked 25 mL round-bottom flask, compound (5) (0.30 g, 0.55 mmol) and tributyl(4-(2-octyldodecyl)thiophene-2-yl)stannane (1.17 g, 1.65 mmol) were dissolved in degassed DMF (15 mL), and the solution was stirred under an Ar atmosphere. To this solution was added $Pd(PPh_3)_4$ (0.032 g, 0.03 mmol), and the solution was heated to 130℃ and stirred overnight. After the reaction had gone to completion, the solution was cooled to room temperature. Water was added to the reaction mixture and extracted using MC. The organic phase was washed with brine three times and dried over anhydrous $MgSO_4$, and evaporated by rotary evaporation. The crude product was purified by flash column chromatography (MC/MeOH, 99:1 v/v) to give a red solid. Yield: 73.44% (0.45 g). ^{1}H NMR (300 MHz, $CDCl_3$, δ): 7.89 (s, 2H), 7.61 (s, 2H), 7.09 (s, 2H), 4.41 (t, J = 7.8 Hz, 4H), 2.60 (d, J = 6.9 Hz, 4H), 1.83 (m, 4H), 1.64 (m, 2H), 1.49–1.21 (m, 84H), 0.87 (t, J = 7.5 Hz, 18H). ^{13}C NMR (500 MHz, $CDCl_3$, δ): 157.65, 142.52, 137.15, 128.51, 126.97, 125.60, 125.13, 119.88, 44.00, 39.17, 35.25, 33.51, 32.13, 32.00, 30.27, 29.91, 29.86, 29.56, 29.53, 29.47, 28.53, 27.24, 26.83, 22.89, 22.84, 14.32, 14.29. Anal. calcd for $C_{72}H_{122}N_2O_2S_2$: C 77.78, H 11.06, N 2.52, S 5.77; found: C 77.82, H 11.01, N 2.51, S 5.71. HRMS (ESI, m/z): $[M + H]^+$ calcd for $C_{72}H_{123}N_2O_2S_2$ 1111.9026; Found 1111.9019.

Synthesis of 3,7-bis(5-bromo-4-(2-octyldodecyl)thiophen-2-yl)-1,5-dioctyl-1,5-naphthyridine-2,6-dione (8): In a two-necked 50 mL round-bottom flask, compound (7)

(1.00 g, 0.90 mmol) was dissolved in $CHCl_3$ (100 mL), and the solution was stirred at 0℃. To this solution was added NBS (0.33 g, 1.84 mmol), and the solution was heated to 25℃ and stirred overnight. After the reaction had gone to completion, the solution was cooled to room temperature, and then water was added to the reaction mixture and extracted using $CHCl_3$. The organic phase was washed with brine three times and dried over anhydrous $MgSO_4$, and evaporated by rotary evaporation. The crude product was purified by column chromatography (EtOAc/n-Hexane, 1:99 v/v) to give a red solid. Yield: 63.05% (0.72 g). ^{1}H NMR (300 MHz, $CDCl_3$, δ): 7.83 (s, 2H), 7.37 (s, 2H), 4.40 (t, J = 7.2 Hz, 4H), 2.56 (d, J = 7.2 Hz, 4H), 1.82 (m, 4H), 1.71 (m, 2H), 1.49–1.21 (m, 84H), 0.86 (t, J = 9.6 Hz, 18H). ^{13}C NMR (500 MHz, $CDCl_3$, δ): 157.55, 141.40, 136.38, 126.88, 126.32, 125.22, 118.73, 116.28, 44.05, 38.85, 34.47, 33.55, 32.13, 32.00, 30.26, 29.90, 29.86, 29.56, 29.53, 29.48, 28.52, 27.21, 26.77, 22.89, 22.86, 14.32, 14.29. Anal. calcd for $C_{72}H_{120}Br_2N_2O_2S_2$: C 68.11, H 9.53, N 2.21, S 5.05; found: C 68.29, H 9.63, N 2.28, S 5.08. HRMS (ESI, m/z): $[M + H]^+$ calcd for $C_{72}H_{121}Br_2N_2O_2S_2$ 1269.7227; Found 1267.7239.

Polymerization for PNTDT-2T: In an oven-dried 50 mL Schlenk flask, compound (8) (200 mg, 0.158 mmol), (5,5'-bis(trimethylstannyl)-2,2'-bithiophene (77 mg, 0.158 mmol), (*o*-tol)$_3$P (4.2 mg, 0.014 mmol) and Pd_2dba_3 (3.2 mg, 0.003 mmol) were added. The flask was purged three times with successive vacuum and argon filling cycle, and then anhydrous toluene (5 mL) was added. After 5 mL of distilled toluene was added,

the solution was refluxed for 1 h under an Ar atmosphere. After cooling down to room temperature, the solution was precipitated into MeOH. The solid was further purified by Soxhlet extraction with MeOH, acetone, hexane, MC and then $CHCl_3$. Finally the $CHCl_3$ fraction was concentrated, and then precipitated in MeOH. The dark purple solid was obtained after filtering and vacuum drying. Yield: 93.53% (188 mg). GPC: (Mn = 34 kDa, PDI = 1.6). ^{1}H NMR (400 MHz, 1,1,2,2-tetrachloroethane-d_2, 110 ˚C, δ): 7.93 (s, 2H), 7.71 (s, 2H), 7.23 (s, 4H), 4.68–4.30 (br, 2H), 3.10–2.70 (br, 2H), 2.09–0.60 (br, 108H). Anal. calcd: C 75.30, H 9.95, N 2.20, S 10.05; found: C 75.43, H 9.93, N 2.20, S 10.04.

Polymerization for PNTDT-TT: PNTDT-TT was synthesized from 8 (180 mg, 0.142 mmol), 2,5-bis(trimethylstannyl)thieno[3,2-b]thiophene (66 mg, 0.127 mmol) by following a same procedure as PNTDT-2T. The resulting co-polymer PNTDT-TT was obtained as a dark blue solid. Yield: 81.36% (144 mg). GPC: (Mn = 85 kDa, PDI = 4.2). ^{1}H NMR (400 MHz, 1,1,2,2-tetrachloroethane-d_2, 110 ˚C, δ): 7.95 (s, 2H), 7.75 (s, 2H), 7.45 (s, 2H), 4.71–4.29 (br, 2H), 3.10–2.70 (br, 2H), 2.09–0.63 (br, 108H). Anal. calcd: C 74.94, H 10.00, N 2.24, S 10.26; found: C 74.97, H 10.11, N 2.27, S 10.24.

Polymerization for PNTDT-2F2T: PNTDT-2F2T was synthesized from 8 (120 mg, 0.095 mmol), (3,3'-difluoro-[2,2'-bithiophene]-5,5'-diyl)bis(trimethylstannane) (50 mg, 0.095 mmol) by following a same procedure as PNTDT-2T. The resulting co-polymer

PNTDT-2F2T was obtained as a dark blue solid. Yield: 83.06% (103 mg). GPC: (Mn = 54 kDa, PDI = 28.5). ^{1}H NMR (400 MHz, 1,1,2,2-tetrachloroethane-d_2, 110 ˚C, δ): 7.94 (s, 2H), 7.70 (s, 2H), 7.09 (s, 2H), 4.63–4.29 (br, 2H), 3.05–2.70 (br, 2H), 2.09–0.63 (br, 108H). Anal. calcd: C 73.23, H 9.53, N 2.14, S 9.77; found: C 73.20, H 9.56, N 2.18, S 9.76.

4.4. Conclusion

In summary, three NTDT-based D-A-type conjugated polymers, PNTDT-2T, PNTDT-TT, and PNTDT-2F2T, were designed and synthesized in order to examine relationships between polymer crystallinity and photovoltaic performance. The thermal, computational, electrochemical, and photophysical results show that PNTDT-2F2T had the lowest HOMO energy level (-5.20 eV), along with better light absorptivity ($\alpha \approx 1.6 \times 10^5$ cm^{-1}) and crystallinity (CCL = 31.9 Å) than PNTDT-2T (HOMO: -5.07 eV, $\alpha \approx 6.1 \times 10^4$ cm^{-1}, CCL = 24.6 Å) and PNTDT-TT (HOMO: -5.10 eV, $\alpha \approx 9.3 \times 10^4$ cm^{-1}, CCL = 18.3 Å). Consequently, PNTDT-2F2T exhibited a superior power conversion efficiency of up to 9.63% with a high short circuit current of 18.80 mA/cm^2, open circuit voltage of 0.73 V, and fill factor of 0.70, for a 210 nm thick-active-layer single-cell device.

4.5. Reference

[1] C. J. Brabec, *Sol. Energy Mater. Sol. Cells* **2004**, *83*, 273.

[2] S. Günes, H. Neugebauer, N. S. Sariciftci, *Chem. Rev.* **2007**, *107*, 1324.

[3] M. C. Scharber, N. S. Sariciftci, *Prog. Polym. Sci.* **2013**, *38*, 1929.

[4] Y. Huang, E. J. Kramer, A. J. Heeger, G. C. Bazan, *Chem. Rev.* **2014**, *114*, 7006.

[5] L. Lu, T. Zheng, Q. Wu, A. M. Schneider, D. Zhao, L. Yu, *Chem. Rev.* **2015**, *115*, 12666.

[6] K. A. Mazzio, C. K. Luscombe, *Chem. Soc. Rev.* **2015**, *44*, 78.

[7] Y. Kim, S. Cook, S. M. Tuladhar, S. A. Choulis, J. Nelson, J. R. Durrant, D. D. C. Bradley, M. Giles, I. McCulloch, C. S. Ha and M. Ree, *Nat. Mater.* **2006**, *5*, 197.

[8] S. Albrecht, J. R. Tumbleston, S. Janietz, I. Dumsch, S. Allard, U. Scherf, H. Ade, D. Neher, *J. Phys. Chem. Lett.* **2014**, *5*, 1131.

[9] M. Lenes, L. J. A. Koster, V. D. Mihailetchi, P. W. M. Blom, *Appl. Phys. Lett.* **2006**, *88*, 243502.

[10] T. Kirchartz, T. Agostinelli, M. Campoy-Quilles, W. Gong, J. Nelson, *J. Phys. Chem. Lett.* **2012**, *3*, 3470.

[11] D. Bartesaghi, I. d. C. Pérez, J. Kniepert, S. Roland, M. Turbiez, D. Neher, L. J. A. Koster, *Nat. Commun.* **2015**, *6*, 7083.

[12] N. Wang, Z. Chen, W. Wei, Z. Jiang, *J. Am. Chem. Soc.* **2013**, *135*, 17060.

[13] M. Wang, X. Hu, P. Liu, W. Li, X. Gong, F. Huang, Y. Cao, *J. Am. Chem. Soc.* **2011**, *133*, 9638.

[14] T. Yang, M. Wang, C. Duan, X. Hu, L. Huang, J. Peng, F. Huang, X. Gong, *Energy Environ. Sci.* **2012**, *5*, 8208.

[15] X. Hu, C. Yi, M. Wang, C.-H. Hsu, S. Liu, K. Zhang, C. Zhong, F. Huang, X. Gong, Y. Cao, *Adv. Energy Mater*. **2014**, *4*, 1400378.

[16] T. Xu, L. Yu, *Materials Today* **2014**, *17*, 11.

[17] A. V. Akkuratov, P. A. Troshin, *Polym. Sci. Ser. B* **2014**, *56*, 414.

[18] I. Osaka, T. Kakara, N. Takemura, T. Koganezawa, K. Takimiya, *J. Am. Chem. Soc.* **2013**, *135*, 8834.

[19] Y. Sun, J. Seifter, M. Wang, L. A. Perez, C. Luo, G. C. Bazan, F. Huang, Y. Cao, A. J. Heeger, *Adv. Energy Mater*. **2014**, *4*, 1301601.

[20] V. Vohra, K. Kawashima, T. Kakara, T. Koganezawa, I. Osaka, K. Takimiya, H. Murata, *Nat. Photonics* **2015**, *9*, 403

[21] K. Kawashima, T. Fukuhara, Y. Suda, Y. Suzuki, T. Koganezawa, H. Yoshida, H. Ohkita, I. Osaka, K. Tamikiya, *J. Am. Chem. Soc.* **2016**, *138*, 10265.

[22] Y. Liu, J. Zhao, Z. Li, C. Mu,, W. Ma, H. Hu, K. Jiang, H. Lin, H. Ade, H. Yan, *Nat. Commun.* **2014**, *5*, 5293.

[23] H. W. Ro, J. M. Downing, S. Engmann, A. A. Herzing, D. M. DeLongchamp, L. J. Richter, S. Mukherjee, H. Ade, M. Abdelsamie, L. K. Jagadamma, A. Amassian, Y. Liu, H. Yan, *Energy Environ. Sci.* **2016**, *9*, 2835.

[24] J. Zhao, Y. Li, A. Hunt, J. Zhang, H. Yao, Z. Li, J. Zhang, F. Huang, H. Ade, H. Yan, *Adv. Mater.* **2016**, *28*, 1868.

[25] I. Osaka, M. Shimawaki, H. Mori, I. Doi, E. Miyazaki, T. Koganezawa, K. Takimiya, *J. Am. Chem. Soc.* **2012**, *134*, 3498.

[26] W. Ma, G. Yang, K. Jiang, J. H. Carpenter, Y. Wu, X. Meng, T. McAfee, J. Zhao, C. Zhu, C. Wang, H. Ade, H, Yan, *Adv. Energy Mater*. **2015**, *5*, 1501400.

[27] R. Mondal, S. Ko, J. E. Norton, N. Miyaki, H. A. Becerril, E. Verploegen, M. F. Toney, J.-L. Brédas, M. D. McGehee, Z. Bao, *J. Mater. Chem.* **2009**, *19*, 7195.

[28] O. P. M. Gaudin, I. D. W. Samuel, S. Amriou, P. L. Burn, *Appl. Phys. Lett.* **2010**, *96*, 053305.

[29] W. S. Yoon, D. W. Kim, J.-M. Park, I. Cho, O. K. Kwon, D. R. Whang, J. H. Kim, J.-H. Park, S. Y. Park, *Macromolecules* **2016**, *49*, 8489.

[30] S. Zhang, Y. Qin, M. A. Uddin, B. Jang, W. Zhao, D. Liu, H. Y. Woo, J. Hou, *Macromolecules* **2016**, *49*, 2993.

[31] J. Wang, X. Bao, D. Ding, M. Qiu, Z. Du, J. Wang, J. Liu, M. Sun, R. Yang, *J. Mater. Chem. A* **2016**, *4*, 11729.

[32] R. Rieger, D. Beckmann, A. Mavrinskiy, M. Kastler, K. Müllen, *Chem. Mater.* **2010**, *22*, 5314.

[33] T. Lei, Y. Cao, X. Zhou, Y. Peng, J. Bian, J. Pei, *Chem. Mater.* **2012**, *24*, 1762.

[34] W. Lee, G.-H. Kim, S.-J. Ko, S. Yum, S. Hwang, S. Cho, Y.-H. Shin, J. Y. Kim, H. Y. Woo, *Macromolecules* **2014**, *47*, 1604.

[35] M.-H. Choi, H. Y. Kim, E. J. Lee, D. K. Moon, *Polymer* **2016**, *91*, 162.

[36] Y. Zhang, S. K. Hau, H.-L. Yip, Y. Sun, O. Acton, A. K. Y. Jen, *Chem. Mater.* **2010**, *22*, 2696.

[37] X. Guo, H. Xin, F. S. Kim, A. D. T. Liyanage, S. A. Jenekhe, M. D. Watson, *Macromolecules* **2011**, *44*, 269.

[38] C. Cui, Z. He, Y. Wu, X. Cheng, H. Wu, Y. Li, Y. Cao, W.-Y. Wong, *Energy Environ. Sci.* **2016**, *9*, 885.

[39] J. Grey, *Nat. Mater.* **2016**, *15*, 705.

[40] Y. Zhang, S.-C. Chien, K.-S. Chen, H.-L. Yip, Y. Sun, J. A. Davies, F.-C. Chen, A. K. Y. Jen, *Chem. Commun.* **2011**, *47*, 11026.

[41] T. L. Nguyen, H. Choi, S.-J. Ko, M. A. Uddin, B. Walker, S. Yum, J.-E. Jeong, M. H. Yun, T. Shin, S. Hwang, J. Y. Kim, H. Y. Woo, *Energy Environ. Sci.* **2014**, *7*, 3040.

[42] H. Choi, S.-J. Ko, T. Kim, P.-O. Morin, B. Walker, B. H. Lee, M. Leclerc, J. Y. Kim, A. J. Heeger, *Adv. Mater.* **2015**, *27*, 3318.

[43] M. S. Chen, J. R. Niskala, D. A. Unruh, C. K. Chu, O. P. Lee, J. M. J. Fréchet, *Chem. Mater.* **2013**, *25*, 4088.

[44] V. Vohra, K. Kawashima, T. Kakara, T. Koganezawa, I. Osaka, K. Takimiya, H. Murata, *Nat. Photonics* **2015**, *9*, 403.

[45] W. Li, K. H. Hendriks, A. Furlan, W. S. C. Roelofs, M. M. Wienk, *J. Am. Chem. Soc.* **2013**, *135*, 18942.

[46] J. Lee, D. H. Sin, B. Moon, J. Shin, H. G. Kim, M. Kim, K. Cho, *Energy Environ. Sci.* **2017**, *10*, 247.

[47] J. Zhou, S. Xie, E. F. Amond, M. L. Becker, *Macromolecules* **2013**, *46*, 3391.

Abstract in Korean

유기 반도체는 첨단 광전자 소자 재료로서의 유망한 잠재성으로 인해 지난 10년간 큰 주목을 받았다. 유기 반3도체 중에서 다이케토피롤로피롤 (diketopyrrolopyrrole, DPP), 아이소인디고 (isoindigo, II), 아이소디피피 (isoDPP) 그리고 싸이에노아이소인디고 (thienoisoindigo, TII)와 같은 비스락탐 (bis-lactam) 기반의 물질들은 (ㄱ) 락탐 유닛의 전자-당김 효과에 의한 높은 전자 친화력, (ㄴ) 그들의 평면 구조에 기인한 강한 파이-파이 상호작용, (ㄷ) 락탐 내 *N*-원자 위치에 알킬 및 아릴 가지 치환에 의한 용해도 조절 가능성 등의 독특한 특성들로 인해 유망한 전자-받개 빌딩 블록으로 심도 깊게 연구되어 왔다. 이를 바탕으로, 본 박사 학위 논문에서는 단분자 혹은 고분자 시스템 내에서 효과적인 전자-받개 빌딩 블록으로 사용될 수 있는 비스락탐 기반의 유기 반도체에 관한 연구를 진행하였다. 고성능의 유기 전계-효과 트랜지스터 (organic field-effect transistors, OFETs)와 유기태양전지 (organic photovoltaics, OPVs) 소자 구현을 목표로 세가지 다른 종류의 비스락탐 기반의 유기 반도체 물질을 합성하였으며 이들의 구조-특성 상관관계를 관찰 하였다.

첫째로, 고성능 n-형 유기 전계-효과 트랜지스터 구현을 위해 다이케토피롤로피롤 기반의 신형 단분자인 DPP-T-DCV를 설계 및 합성하였다. 다이케토피롤로피롤에 강한 전자-받개 기능단인 다이사이아노비닐 (dicyanovinyl) 그룹을 도입함으로써 효과적인 에너지 레벨 조절이 가능하였다. 또한 구조 분석을 통해 DPP-T-DCV 결정이 층상 구조를 가짐을 확인 할 수 있었고, 각 층상의 높이가 고체 상태의 분자 단층의 높이와 일치함을 확인하였다. 적절한 에너지 레벨 및 높은 결정성을 기반으로, DPP-T-DCV 단결정을 이용한 유기 전계-효과 트랜지스터 소자 적용 시 n-형 특성과 함께 0.96 $cm^2 V^{-1} s^{-1}$ 의 높은 전자이동도를 나타내었다. 또한, 진공 증착 소자에서도 0.64 $cm^2 V^{-1} s^{-1}$ 의 전자이동도를 보임을 통해 높은 실용성을 가지는 유기 반도체 물질임을 확인하였다. (Chapter 2)

두번째로, 새로운 전자-받개 비스락탐 기반의 빌딩 블록인 3,7-dithiophen-2-yl-1,5-dialkyl-1,5-naphthyridine-2,6-dione (NTDT)를 성공적으로 합성하였고, 고성능 유기태양전지 소자 구현을 목표로 NTDT를 전자-받개로 벤조다이싸이오펜 (benzodithiophene, BDT)를 전자-주개로 하는 공액 고분자인 P(NTDT-BDT)를 설계 및 합성하였다. 신규 빌딩 블록인 NTDT 및 신규 고분자 P(NTDT-BDT)의 열적, 전자적, 물리 화학적, 전기 화학적 및

구조적 특성 분석을 위해 가장 많은 연구가 되었던 비스락탐 빌딩 블록인 DPPT와 그 중합체 P(DPPT-BDT)를 같이 합성하여 비교 분석하였다. 결과적으로 NTDT와 P(NTDT-BDT)는 DPPT 유도체에 비해 현저하게 높은 흡광 계수, 깊은 HOMO 에너지 레벨 그리고 더 평탄한 구조를 가짐을 확인하였고 이를 통해 NTDT 유도체가 DPPT 유도체에 비해 유기태양전지 소자에 더 적합한 물질임을 확인하였다. P(NTDT-BDT) 기반의 벌크 이종접합 유기태양전지는 8.16%의 광전환효율 (Power Conversion Efficiency, PCE)과 18.51 mA cm^{-2}의 높은 단락 전류 (Short Circuit Current, J_{sc})값을 보였으며, 이는 현재까지 보고된 벤조다이싸이오펜 기반의 공액 고분자를 활용한 유기태양전지 소자 중 가장 높은 단락 전류값임을 확인하였다. 이러한 연구를 통해 신규성 비스락탐 유닛인 NTDT가 고성능 유기태양전지 구현에 전도 유망한 전자-받개 빌딩 블록임을 성공적으로 규명하였다. (Chapter 3)

앞선 연구를 통해 NTDT 기반의 고분자가 유기태양전지로서의 유망한 가능성을 가지는 물질임을 확인 했지만, P(NTDT-BDT) 기반 소자의 경우 다소 얇은 활성층 두께인 140 nm 에서만 최적화 됨을 보였다. 이는 상용적으로 필요한 두께인 200 nm 이상의 두꺼운 활성층 유기태양전지 소자

(thick-active-layer OPVs)를 구현하기에 P(NTDT-BDT)가 충분한 결정성을 가지지 못하기 때문이라고 판단하였으며 이에 따라 화학 구조 변형을 통해 고분자의 결정성을 증가시켜야 한다고 판단하였다. 따라서 NTDT 기반의 신규성 고분자인 PNTDT-2T, PNTDT-TT 그리고 PNTDT-2F2T를 설계 및 합성하였다. 이 중 PNTDT-2F2T의 경우, 고분자 중합 시 사용된 고평면성의 전자-받개인 NTDT와 전자-주개인 2F2T의 적절한 조합으로 인해 다른 고분자인 PNTDT-2T 및 PNTDT-TT에 비해 우수한 고분자 결정성 및 높은 흡광 계수를 나타내었다. 결과적으로 PNTDT-2F2T를 기반으로한 유기태양전지는 추가 열처리 공정 없이 200 nm 이상의 두꺼운 활성층 조건에서 9.63%의 우수한 광전환효율을 보였다. (Chapter 4)

주요어 : 유기 반도체, 유기 전계-효과 트랜지스터, 유기태양전지

학 번 : 2009-20624

List of Publications

1. Carmen Coya, Á ngel Luis Á lvarez, **Won Sik Yoon**, and Soo Young Park, "Influence of the 1,2,4-Linking Hyperbranched Poly(arylenevinylene) structure on the organic light emitting diodes performance comparing to conventional 1,3,5-liking", *J. Appl. Phys.* **2011**, *109*, 094507.

2. **Won Sik Yoon**, Sang Kyu Park, Illhun Cho, Jeong-A Oh, Jong H. Kim, and Soo Young Park, "High-Mobility n-Type Organic Transistors Based on a Crystallized Diketopyrrolopyrrole Derivative", *Adv. Funct. Mater.* **2013**, *23*, 3519.

3. Jeong-Wook Mun, Illhun Cho, Donggu Lee, **Won Sik Yoon**, Oh Kyu Kwon, Changhee Lee, and Soo Young Park, "Acetylene-bridged D-A-D Type Small Molecule Comprising Pyrene and Diketopyrrolopyrrole for High Efficiency Organic Solar Cells", *Org. Electron.* **2013**, *14*, 2341.

4. Jun-Mo Park, Sang Kyu Park, **Won Sik Yoon**, Jin Hong Kim, Dong Won Kim, Tae-Lim Choi, and Soo Young Park , "Designing Thermally Stable Conjugated Polymers with Balanced Ambipolar Field-Effect Mobilities by Incorporating Cyanovinylene Linker Unit", *Macromolecules* **2016**, *49*, 2985.

5. Jin Hong Kim, Sang Kyu Park, Jong H. Kim, Dong Ryeol Whang, **Won Sik Yoon**, and Soo Young Park, "Self-assembled organic single crystalline nanosheet for solution processed n-channel field-effect transistors", *Adv. Mater.* **2016**, *28*, 6011.

6. Illhun Cho, Sang Kyu Park, Boseok Kang, Jong Won Chung, Jin Hong Kim, **Won Sik Yoon**, Kilwon Cho, and Soo Young Park, "Dicyanovinyl-Substituted Indolo[3,2-b]indole Derivatives: Low Band-Gap π-Conjugated Molecules for Single-Component Ambipolar Organic Field-Effect Transistor", *J. Mater. Chem. C* **2016**, 4, 9460.

7. **Won Sik Yoon**, Dong Won Kim, Jun-Mo Park, Illhun Cho, Oh Kyu Kwon, Dong Ryeol Whang, Jin Hong Kim, Jung-Hwa Park, and Soo Young Park, "A Novel bis-Lactam Acceptor with Outstanding Molar Extinction Coefficient and Structural Planarity for Donor-Acceptor Type Conjugated Polymer", *Macromolecules* **2016**, *49*, 8489.

8. **Won Sik Yoon**, Dong Won Kim, Min-Woo Choi, Jun-Mo Park, and Soo Young Park, "Designing 1,5-Naphthyridine-2,6-dione-Based Conjugated Polymers for Higher Crystallinity and Enhanced Light Absorption to Achieve 9.63% Efficiency Polymer Solar Cells", *Adv. Energy Mater.* **2017**, *accepted*.

List of Presentations

International

1. (**Oral**) **Won Sik Yoon**, Illhun Cho, and Soo Young Park, "Synthesis and Emission Color Tuning of Hyghly Luminescent π-Conjugated Hyperbranched Polymer", KJF2010 (Korea Japan Joint Forum 2010), Fukuoka, Japan, 2010-08-22.

2. (**Poster**) **Won Sik Yoon**, and Soo Young Park, "Synthesis and Characterization of Benzothiadiazole-containing Hyperbranched Polymers for Photovoltaic Application", 2012 MRS spring meeting, Sanfrancisco, USA, 2012-04-11.

3. (**Poster**) Jeong-A Oh, **Won Sik Yoon**, Jung-Hwa Park, and Soo Young Park, "Low Band Gap and Solution-Processable Furan-Containing Diketopyrrolopyrrole-Based Small Molecules as Acceptor Materials in Organic Solar Cells", The 15th Asian Chemical Congress, Singapore National Institute of Chemistry, 2013-08-22.

4. (**Poster**) **Won Sik Yoon**, Sang Kyu Park, Illhun Cho, and Soo Young Park, "Energy Level Tailoring of Diketopyrrolopyrrole-based Small Molecules for Organic Field-

Effect Transistor and Solar Cell Applications", 2013 MRS Fall Meeting, Boston, USA, 2013-12-06.

5. (**Poster**) YoungJoo Park, **Won Sik Yoon**, Sangyoon Oh, and Soo Young Park, "Synthesis and Characterization of Isoindigo and Thienoisoindigo Derivatives for Organic Field Effect Transistor Application", KJF 2014, Japan, 2014-09-21.

6. (**Poster**) **Won Sik Yoon**, Dong won Kim, Min Woo Choi, and Soo Young Park, “Dithiophenyl Naphthyridinedione (NTDT)-Based Donor-Acceptor Polymers for High-performance Organic Solar Cells”, 13th International Symposium on Functional π-Electron Systems, Hong Kong, China, 2017-06-04.

Domestic

1. (**Poster**) **Won Sik Yoon**, and Soo Young Park, "Design and Synthesis of Soluble 1,2,4-Linking Hyperbranched Poly(styrylthiophene) for Photovoltaic Applications", 대한화학회 제 105 회 총회 및 학술발표회(춘계), Songdo, Korea, 2010-04-29.

2. (**Oral**) **Won Sik Yoon**, and Soo Young Park, "Synthesis and Emission Color Tuning of Highly Luminescent π-Conjugated Hyperbranched Polymer", 대한화학회 제 106 회 총회 및 학술발표회(추계), Daegu, Korea, 2010-10-14.

3. (**Poster**) Jeong-A Oh, **Won Sik Yoon**, Jung-Hwa Park, and Soo Young Park, "Low Band Gap and Solution-Processable Furan-Containing Diketopyrrolopyrrole-Based Small Molecules as Acceptor Materials in Organic Solar Cells", 2nd Korea-UK Student Exchange Program, SEOUL NATIONAL UNIVERSITY, 2013-03-25.

4. (**Poster**) Jin Hong Kim, Sang Kyu Park, **Won Sik Yoon**, Jong Hyun Kim, and Soo Young Park, "Synthesis and Characterization of High-Performance n-Type Organic Semiconductor: Novel Dicyanodistyrylbenzene Derivative Forming Large 2D Single Crystal ", ISCE 2013, SEOUL NATIONAL UNIVERSITY, 2013-05-06.

5. (**Poster**) Jeong-A Oh, **Won Sik Yoon**, Jung-Hwa Park, and Soo Young Park, "Novel Acceptor materials of Furan-Containing Diketopyrrolopyrrole Derivatives for Solution-Processed Organic Solar Cells", ISCE 2013, SEOUL NATIONAL UNIVERSITY, 2013-05-06.

List of Patents

1. 박수영, **윤원식**, 김동원, 박준모 “유기태양전지 광 활성층용 고분자 및 이를 포함하는 유기태양전지”, 출원번호 “10-2017-0033259”